The Chandra Deep Field South: Optical Spectroscopy I. [1]

G. P. Szokoly[1,2], J. Bergeron[3], G. Hasinger[1,2], I. Lehmann[1]. L. Kewley[4,5], V. Mainieri[6], M. Nonino[7], P. Rosati[6], R. Giacconi[8], R. Gilli[9], R. Gilmozzi[6], C. Norman[4], M. Romaniello[6] E. Schreier[8,10], P. Tozzi[7], J. X. Wang[4], W. Zheng[4] and A. Zirm[4]

szgyula@mpe.mpg.de

ABSTRACT

We present the results of our spectroscopic follow-up program of the X-ray sources detected in the 942 ks exposure of the *C*handra *D*eep *F*ield *S*outh (CDFS). 288 possible counterparts were observed at the VLT with the FORS1/FORS2 spectrographs for 251 of the 349 Chandra sources (including three additional faint X-ray sources). Spectra and R-band images are shown for all the observed sources and R−K colours are given for most of them. Spectroscopic redshifts were obtained for 168 X-ray sources, of which 137 have both reliable optical identification and redshift estimate (including 16 external identifications). The R$<$ 24 observed sample comprises 161 X-ray objects (181 optical counterparts) and 126 of them have unambiguous spectroscopic identification. There are two spikes in the redshift distribution, predominantly populated by type-2 AGN but also type-1 AGN and X-ray normal galaxies: that at $z = 0.734$ is fairly narrow (in redshift space) and comprises two clusters/groups of galaxies centered on extended X-ray

[1]Max-Planck-Institut für extraterrestrische Physik, Giessenbachstraße, Garching, D-85748 Germany

[2]Astrophysikalisches Institute Potsdam, An der Sternwarte 16, Potsdam, D-14482, Germany

[3]Institut d'Astrophysique de Paris, 98bis, bd Arago, 75014 Paris, France

[4]The Johns Hopkins University, Department of Physics and Astronomy, Baltimore, MD 21218, USA

[5]Harvard-Smithsonian Center for Astrophysics, 60 Garden Street, Cambridge, MA 02138, USA

[6]European Southern Observatory, Karl-Schwarzschild-Strasse 2, Garching, D-85748, Germany

[7]Osservatorio Astronomico, Via G. Tiepolo 11, 34131 Trieste, Italy

[8]Associated Universities, Inc. 1400 16th Stret, NW, Suite 730, Washington, DC 20036, USA

[9]Osservatorio Astrofisico di Arcetri, Largo E. Fermi 5, I-50125 Firenze, Italy

[10]Space Telescope Science Institute, 3700 San Martin Drive, Baltimore, MD 21218, USA

sources, the second one at $z = 0.674$ is broader and should trace a sheet-like structure. The type-1 and type-2 populations are clearly separated in X-ray/optical diagnostics involving parameters sensitive to absorption/reddening: X-ray hardness ratio (HR), optical/near-IR colour, soft X-ray flux and optical brightness. Nevertheless, these two populations cover similar ranges of hard X-ray luminosity and absolute K magnitude, thus trace similar levels of gravitational accretion. Consequently, we introduce a new classification based solely on X-ray properties, HR and X-ray luminosity, consistent with the unified AGN model. This X-ray classification uncovers a large fraction of optically obscured, X-ray luminous AGNs missed by the classical optical classification. We find a similar number of X-ray type-1 and type-2 QSOs ($L_{\rm X}$(0.5-10 keV)$> 10^{44}$ erg s^{-1}) at $z > 2$ (13 sources with unambiguous spectroscopic identification); most X-ray type-1 QSOs are bright, R$\lesssim$ 24, whereas most X-ray type-2 QSOs have R$\gtrsim$ 24 which may explain the difference with the CDFN results as few spectroscopic redshifts were obtained for R$>$ 24 CDFN X-ray counterparts. There are X-ray type-1 QSOs down to $z \sim 0.5$, but a strong decrease at $z < 2$ in the fraction of luminous X-ray type-2 QSOs may indicate a cosmic evolution of the X-ray luminosity function of the type-2 population. An X-ray spectral analysis is required to confirm this possible evolution. The red colour of most X-ray type-2 AGN could be due to dust associated with the X-ray absorbing material and/or a substantial contribution of the host galaxy light. The latter can also be important for some redder X-ray type-1 AGN. There is a large population of EROs (R$-$K$>$ 5) as X-ray counterparts and their fraction strongly increases with decreasing optical flux, up to 25% for the R$\geq$ 24 sample. They cover the whole range of X-ray hardness ratios, comprise objects of various classes (in particular a high fraction of $z \gtrsim 1$ X-ray absorbed AGNs, but also elliptical and starburst galaxies) and more than half of them should be fairly bright X-ray sources ($L_{\rm X}$(0.5-10 keV)$> 10^{42}$ erg s^{-1}). Photometric redshifts will be necessary to derive the properties and evolution of the X-ray selected EROs.

Subject headings: surveys — galaxies: active — cosmology: observations — quasars: general, evolution — X-rays: galaxies: clusters — techniques: spectroscopic

---

[1]Based on observations collected at the European Southern Observatory, Chile (ESO N$^{\rm o}$ 66.A-0270(A) and 67.A-0418(A)).

1. INTRODUCTION

Deep X-ray surveys indicate that the cosmic X-ray background (XRB) is largely due to accretion onto supermassive black holes, integrated over cosmic time. In the soft (0.5–2 keV) band more than 90% of the XRB flux has been resolved using 1.4 Msec observations with *ROSAT* (Hasinger et al. 1998) and 1-2 Msec Chandra observations (Brandt et al. 2001a; Rosati et al. 2002; Brandt et al. 2002) and 100 ksec observations with XMM-Newton (Hasinger et al. 2001). In the harder (2-10 keV) band a similar fraction of the background has been resolved with the above Chandra and XMM-Newton surveys, reaching source densities of about 4000 $\deg^{-2}$. Surveys in the very hard (5-10 keV) band have been pioneered using BeppoSAX, which resolved about 30% of the XRB (Fiore et al. 1999). XMM-Newton and Chandra have now also resolved the majority (60-70%) of the very hard X-ray background.

Optical follow-up programs with 8-10m telescopes have been completed for the *ROSAT* deep surveys and find predominantly Active Galactic Nuclei (AGN) as counterparts of the faint X-ray source population (Schmidt et al. 1998; Zamorani et al. 1999; Lehmann et al. 2001), mainly X-ray and optically unobscured AGN (type-1 Seyferts and QSOs) and a smaller fraction of obscured AGN (type-2 Seyferts). The X-ray observations have so far been about consistent with population synthesis models based on unified AGN schemes (Comastri et al. 1995; Gilli et al. 2001), which explain the hard spectrum of the X-ray background by a mixture of X-ray absorbed and unabsorbed AGN, folded with the corresponding luminosity function and its cosmological evolution. According to these models, most AGN spectra are heavily absorbed and about 80% of the light produced by accretion will be absorbed by gas and dust which may reside in nuclear starburst regions that feed the AGN (Fabian et al. 1998). However, these models are far from unique and contain a number of often overlooked assumptions, so their predictive power remains limited until complete samples of spectroscopically classified hard X-ray sources are available. In particular, they require a substantial contribution of high-luminosity absorbed X-ray sources (type-2 QSOs), which so far have only scarcely been detected. The cosmic history of obscuration and its potential dependence on intrinsic source luminosity remain completely unknown. Gilli et al. (2001) e.g. assumed a strong evolution of the absorbed/obscured fraction (ratio of type-2/type-1 AGN) from 4:1 in the local universe to much larger fractions (10:1) at high redshifts (see also Fabian et al. 1998). The gas-to-dust ratio in high-redshift, high-luminosity AGN could be completely different from the usually assumed Galactic value due to sputtering of the dust particles in the strong radiation field (Granato et al. 1997). There could thus be objects which are heavily absorbed at X-rays and unobscured at optical wavelengths.

After having understood the basic contributions to the X-ray background, the general

interest is now focussing on understanding the physical nature of these sources, the cosmological evolution of their properties, and their role in models of galaxy evolution. We know that basically every galaxy with a spheroidal component in the local universe has a supermassive black hole in its centre (Gebhardt et al. 2000). The luminosity function of X-ray selected AGN shows strong cosmological density evolution at redshifts up to 2, which goes hand in hand with the cosmic star formation history (Miyaji et al. 2000). At the redshift peak of optically selected QSOs, around z=2.5, the AGN space density is several hundred times higher than locally, which is in line with the assumption that most galaxies have been active in the past and that the feeding of their black holes is reflected in the X-ray background. While the comoving space density of optically and radio-selected QSOs has been shown to decline significantly beyond a redshift of 2.5 (Schmidt et al. 1997; Fan et al. 2001; Shaver et al. 1996), the statistical quality of X-ray selected high-redshift AGN samples still needs to be improved (Miyaji et al. 2000). The new Chandra and XMM-Newton surveys are now providing strong additional constraints.

Optical identifications of the deepest Chandra and XMM-Newton fields are still in progress, however, a mixture of obscured and unobscured AGN with an increasing fraction of obscuration at lower flux levels seems to be the dominant population in these samples (Fiore et al. 2000; Barger et al. 2001a; Tozzi et al. 2001; Rosati et al. 2002; Stern et al. 2002). First examples of the long-sought class of high-redshift, radio-quiet, high-luminosity, heavily obscured active galactic nuclei (type-2 QSO) have also been detected in deep Chandra fields (Norman et al. 2002; Stern et al. 2002) and in the XMM-Newton deep survey in the Lockman Hole field (Hasinger 2002).

In this paper we report on our optical identification work in the Chandra Deep Field South, which, thanks to the efficiency of the VLT, has progressed to the faintest magnitudes among the deepest X-ray surveys.

2. THE CHANDRA DEEP FIELD SOUTH (CDFS)

The Chandra X-ray Observatory has performed deep X-ray surveys in a number of fields with ever increasing exposure times (Mushotzky et al. 2000; Hornschemeier et al. 2000; Giacconi et al. 2001; Tozzi et al. 2001; Brandt et al. 2001a) and has completed a 1 Msec exposure in the Chandra Deep Field South, CDFS (Giacconi et al. 2002; Rosati et al. 2002) and a 2 Msec exposure in the Hubble Deep Field North, HDF-N (Brandt et al. 2002). The Megasecond dataset of the CDFS is the result of the coaddition of 11 individual Chandra ACIS-I exposures with aimpoints only a few arcsec from each other. The nominal aim point of the CDFS is $\alpha = 3:32:28.0$, $\delta = -27:48:30$ (J2000). This field was selected in a

patch of the southern sky characterized by a low galactic neutral hydrogen column density, $N_{\rm H} = 8 \times 10^{19} {\rm cm}^{-2}$, and a lack of bright stars (Rosati et al. 2002).

3. OPTICAL IDENTIFICATIONS IN THE CDFS

Our primary optical imaging was obtained using the FORS1 camera on the ANTU (UT-1 at VLT) telescope. The R band mosaics cover ∼360 arcmin^2 to depths between 26 and 26.7 (Vega magnitudes). This data does not cover the full CDFS area and must be supplemented with other observations (see Figure 14). The ESO Imaging Survey (EIS) has covered this field to moderate depths (5 σ limiting AB magnitudes of 26.0, 25.7, 26.4, 25.4, 25.5 and 24.7 in U′, U, B, V, R and I, respectively) in several bands (Arnouts et al. 2001; Vandame et al. 2001). The EIS data has been obtained using the Wide Field Imager (WFI) on the ESO-MPG 2.2 meter telescope at La Silla. The positioning of the X-ray sources is better than 0.5″(Giacconi et al. 2002) and we readily identify likely optical counterparts in 85% of the cases.

Figure 1 shows the classical correlation between the R-band magnitude and the soft X-ray flux of the CDFS sources. The objects are marked according to their classification (see below). By comparison with the deepest ROSAT survey in the Lockman Hole (Lehmann et al. 2001), the Chandra data extend the previous ROSAT range by a factor of about 40 in X-ray flux and to substantially fainter optical magnitudes. While the bulk of the type-1 AGN population still follows the general correlation along a constant f_X/f_{opt} line, the type-2 AGNs cluster at higher X-ray-to-optical flux ratios. There is also a population of normal galaxies emerging at low fluxes (thus discovered in the Chandra and XMM era).

To be consistent with the already published deep ROSAT catalogs (Lehmann et al. 2001), we used a modified version of the X-ray to optical flux ratios:

$$log_{10}(f_x/f_o) \equiv log_{10}(f_{0.5-2{\rm keV}}/f_R) \equiv log_{10}(f_{0.5-2{\rm keV}}) + 0.4R + 5.71, \quad (1)$$

where the flux is measured in erg cm^{-2} s^{-1} units in the 0.5-2 keV band and R is in Vega magnitudes. The slight change in the normalization (Maccacaro et al. 1988) is motivated by the significantly narrower X-ray energy band used (the original definition was based on the *Einstein* medium sensitivity survey band, 0.3-3.5 keV), which introduces a factor of 1.77 decrease in the flux for objects with a spectral energy index of −1 (classical type-1 AGN) and the use of the R-band instead of V (here we assumed a V−R color of 0.22, typical value for galaxies).

To use this new X-ray to optical flux ratio definition for source classification, we also had to convert the canonical ranges (Stocke et al. 1991) to our new system. The new ranges

for different classes of objects are shown in Table 2. To calculate the new ranges of the X-ray to optical flux ratios, we assumed typical X-ray spectra for each class and calculated the shift in the X-ray flux due to the narrower energy band: a power law with a photon index of Γ=1-2.7 for AGN, a power law with a photon index of Γ=1-2 for BL Lac objects, a Raymond-Smith model with kT =2-7 keV, abundances of 0.1-0.6 and redshifts of z =0-1. For stars and supernova remnants we used Raymond-Smith models with energies of kT=0.5-2 keV, for X-ray binaries powerlaw models with photon index Γ=1-2. For galaxies, we adopted a somewhat ad hoc shift of 0.1-0.3 in the logarithm of the flux due to the different energy bands. This choice was motivated by examining different models for galaxies (warm and hot plasma mixture, powerlaw like emission from X-ray binaries, typical supernova remnant spectra, etc.).

For the shift in the optical flux (using R-band instead of the canonical V-band) we assumed typical values for each class.

The resulting ranges of the X-ray-to-optical flux ratios are shown in Table 2. As can be seen from the table, the new X-ray-to-optical flux ratio is not significantly different from the canonical one. The typical ranges are a bit wider, but this just a consequence of *converting* the ranges instead of directly determining it from large surveys. With our new normalization, we can use the original ranges (Stocke et al. 1991) to make an educated guess on the galactic/extragalactic nature of objects.

4. TARGET SELECTION

Target selection was primarily based on our deep VLT/FORS imaging data (Giacconi et al. 2002), reaching a depth of R $\sim$ 26.5. In regions not covered by this VLT/FORS deep imaging, we used somewhat shallower VLT/FORS imaging in the R-band obtained as part of the survey.

Possible optical counterparts of X-ray sources were selected based on the estimated astrometry error of the X-ray object (for a relatively bright point source at zero off-axis angle the astrometry rms error is $\sim 0\farcs5$). We used the automatically generated optical catalog, however, *every* object was visually inspected for deblending problems and artefacts.

The surface density of our X-ray objects is very well suited to MOS spectroscopy with FORS/VLT. We could fill a large part of the masks with program objects and it was quite rare that we had to choose between multiple optical counterpart candidates within the geometrical constraints of the instrument. As a consequence, our target selection is nearly unbiased. The only selection effect that should be considered was related to objects with multiple

counterpart candidates. In these cases we usually selected the object in the appropriate magnitude range for the particular mask, but in general we tried to revisit these objects – unless the first one turned out to be clearly the counterpart.

We also took advantage of the extremely high accuracy of the robotic masks: in some cases, we reconfigured *some* of the slits between read-outs, without changing the telescope pointing to observe many (brighter) optical counterparts. This way, the integration time on bright objects could be shortened and we could use the remaining time on a different object, while maintaining longer integration times for the faint ones.

During our last two runs (in November and December 2001) we were also using the prefabricated masks (MXU mode – only available for FORS2), as opposed to movable robotic slitlets (MOS mode). For our survey, the only important difference between the two modes is more freedom in the placement of slits in MXU mode. This improved our observing efficiency in the later phase of the survey, where we concentrated on fainter objects (with a higher surface density).

4.1. *The Reliability of the Target Selection*

The reliability of X-ray follow-up surveys using optical (or near infrared) spectroscopy hinges on matching the X-ray source to the *right* optical object. This is primarily done through astrometry. Just how reliable are these identifications? Using deep galaxy number counts (Metcalfe et al. 2001), we expect roughly 0.02 galaxies in every square arcsec area that are brighter than R $\sim$ 26. Considering our best 3σ astrometry error ($1\farcs5$), we expect $\sim$ 0.15 *field* galaxies to fall within our error circle – even in the best, zero off axis angle case. In other words we expect one *false* candidate for every seventh X-ray object at R $<$ 26. Considering the roughly 250 X-ray sources we observed, we expect that for at least 35 of them, there *will be* a completely unrelated faint galaxy, even in an error circle of $1\farcs5$. Fortunately, the X-ray counterpart candidates typically have much brighter magnitudes (see Figure 2). At these brighter magnitudes the probability of field galaxy contamination is much lower, so we should only worry about contamination for very faint (R=25-27) objects.

As our astrometric accuracy heavily depends on the signal-to-noise ratio of the object (i.e. objects with low photon counts are centered with lower accuracy) and the off-axis angle of the object (there is a significant degradation of the PSF of increasing off-axis angles), the total area covered by the sum of the error circles is quite large, around 3900 arcsec^2. In Figure 2, we show the magnitude distribution of our selected primary optical counterparts and the expected magnitude distribution of random field galaxies over this area, based on

galaxy number counts (Metcalfe et al. 2001; Jones et al. 1991). Contamination by random field galaxies becomes a serious problem beyond R $\sim$ 24 and they start to dominate beyond R $\sim$ 26, the practical limit of our imaging survey.

Therefore, extra caution is required in making sure that the *right* optical object is identified as the counterpart. This is not always trivial as the optical spectra do not always show clear signatures of active nuclei (AGNs). In some cases we had to observe every object in the error circle. Fortunately this turns out to be feasible. At R $\sim$ 24 and fainter, deblending is not a serious challenge (using both automated and visual tests). At brighter magnitudes, where deblending would be near impossible (e.g. detecting a R $\sim$ 25 X-ray object in the halo of a R $\sim$ 19 galaxy), the probability of field galaxy contamination is negligible. Stellar contamination is negligible at our high galactic latitude.

It is also important to point out that these estimates of field galaxy contamination are for the probability of finding an unrelated object in our X-ray error circle. We can also ask a technical question: what is the probability of finding a field object on a slit? Taking a $20'' \times 2''$ area (the typical slit length in FORS-1 is around $20''$), we expect to find a R < 23 galaxy in 5% of the slits and we expect statistically a field galaxy with magnitude R < 25 in every second slit. This means that one has to be extremely careful in the data reduction and do a very careful book keeping in the process.

5. OBSERVATIONS AND DATA REDUCTION

Data were obtained during 11 nights in 2000 and 2001. A summary of the observations is presented in Table 4. All observations were using the '150I' grism (150I+17 in FORS-1 and 150I+27 in FORS-2). These grisms provide a pixel scale (dispersed) of 280Å/mm, or roughly 5.5Å/pixel. The nominal resolution of the configuration is $R = \lambda/\Delta\lambda$=230, which corresponds to roughly 20Å at 5600Å. The pixel scale of these instruments is $0.2''$/pixel, so there is no significant degradation of the resolution due to the finite slit width.

In the initial phase of our survey, we exclusively used low resolution multiobject spectroscopy with varying integration time. This strategy maximizes the number of observed objects and provides a (nearly) full spectral coverage for every exposure. This is clearly a trade off, as we then get a significantly lower S/N spectrum for the individual objects, compared to higher resolution long-slit spectroscopy based on photometric redshifts, but the latter technique was deemed to be prohibitevely expensive in observing time in the initial phase of our project.

As our goal was to observe as many objects as possible, we used non standard order

separation filters (either no filter, or the GG-375 filter, which cuts out light bluer than ∼3750Å). It was thus possible to cover a very wide spectral range in a single exposure (in the standard configuration the order separation filter that cuts the light blueward of 5900Å, thus the whole spectral range can only be covered in two exposures).

5.1. *Data Reduction*

Data were reduced by our own semi-automatic pipeline built on top of IRAF. In general we followed standard procedures, but had to deviate slightly in several cases to accomodate particularities of the FORS instrument and do a very rigorous book-keeping. In the following sections, we enumerate these changes.

5.2. *Bias, Overscan and Trim Correction*

The FORS CCD's have in principle 4 read-out modes: high and low gain and one and four amplifier modes. To avoid serious complications, we only used the high gain/one amplifier read-out mode for our spectroscopic observations. This decision resulted in a slightly larger overhead, but this was deemed negligible considering our long integration times, compared to the challenges posed by reducing a 4 amplifier read-out mode spectroscopic observations, where we would have to calibrate the gain of each amplifier very accurately (so we do not introduce artifical features in the spectra).

A sufficient number of full frame bias exposures were taken during each run (typically around 20 per run). These were individually overscan corrected and trimmed. The resulting (bias) frames were averaged with suspect pixels (too high or too low values) filtered out to generate the master bias frame. In each case we verified that the bias frame does not change significantly from night to night within a run.

A slight complication was posed by our spectrophotometric standard observations. These frames were also using one amplifier/high gain, but (to save some time) only 500 rows were read out (centered on the standard star). Since ESO does not provide an under/overscan region for windowed frames, we took a sufficient number (typically 10) of bias frames in this configuration. Naturally (lacking under/overscan region) these frames were *not* overscan corrected, nor trimmed. Instead, they were averaged to create a master bias frame, which *did* include the artificially introduced bias level. We checked the individual frames and confirmed that the variation of this artifical bias level is negligible for these very high S/N frames.

After creating the full and windowed bias frames, all object and calibration (flat and arc) frames were overscan corrected and trimmed (except the windowed frames) and zero subtracted.

At this point we applied a shift in the dispersion direction, based on the slit position, to bring (very crudely; within 10 pixels or 50Å) the observations on a similar wavelength scale. We also inserted gaps in the spatial direction between the neighbouring slits to reduce the risk of contamination between slits. These two steps are purely practical, but make bookkeeping significantly easier.

5.3. *Flatfielding*

In this processing step, we had to tackle three main issues:

The first one is an inherent complication in the FORS instruments. Due to the mechanical construction of the robotic slit masks and the location of the flat-field lamps, flat-field exposures show higher flux levels in a few rows at the upper or lower edge of the slit. To correct for this effect, there are two sets of flat-field lamps in the instrument. We took a sufficient number of flat-field exposures using both sets of lamps. We generated merged flats independently for each lamp set and generated the final flat-field frame by taking the smaller pixel value in the two frames. As the reflections from the two lamp sets do not overlap, this feature can be fully removed.

The second issue is a consequence of our unusual observing strategy. In some cases (due to geometric constraints imposed by the robotic slit masks) we could not target very faint objects with a particular slit, but we had several bright candidates available. In these cases, to maximize efficiency, we reconfigured these slits between readouts so that all bright candidates were observed, while faint objects targeted with other slits were observed with a longer integration time. Due to the extremely high mechanical stability of the FORS instruments, this strategy is very safe. As the sensitivity variation between pixels is potentially color dependent, we decided to generate flat-field frames for each mask. This may not be the optimal strategy since for the slits that are in the same position in two masks, we could use more exposures, thus to create a more accurate flat-field. This alternative strategy would be too complex and the resulting data quality improvement is very marginal, consequently we decided *against* it.

The last major issue is due to the extremely wide spectral coverage used. As our intention was to correct *only* for the pixel-to-pixel sensitivity variations, we had to generate a normalization image (a combination of the flat-field lamp spectrum and the overall quantum

efficiency of the system as a function of wavelength and spatial position). For high resolution (and smaller wavelength coverage) observations, this is often achieved by collapsing in the spatial direction and fitting a function in the dispersion direction. Unfortunately, this technique proved to be impractical for us. The main problem was that we were unable to find an ansatz function that could reproduce the very sharp cutoffs at both ends (due to either the order separation filter or the natural cut-off of the CCD detector) without introducing artifical structure on intermediate scale. An additional complication was that the internal flat-field lamps did not illuminate the slits homogenously – there is a slight gradient in the spatial direction. Therefore, after a slight smoothing of the flat-field exposures, we created the normalization image by a linear or (for very long slits) a second order polynomial fit in the spatial direction. Each flat-field exposure was divided by this normalization frame, thus creating a 'true' flat-field frame, which only contains pixel-to-pixel sensitivity variations. In regions, where the signal was too low, the flat-field was artificially set to one (to avoid the introduction of too high photon noise).

After these steps, the individual, normalized flat-field frames were merged, eliminating the effect of light reflection on the slit edges. Both science and wavelength calibration frames for a given mask were divided by the resulting master flat-field frame.

5.4. *Sky Subtraction*

The sky background was estimated in each column by a linear fit (for longer slits) or just calculating the average (shorter slits) in each column of each slit, rejecting too high pixels (i.e. the targeted object) and subtracting the result. It is important to note that we did *not* correct for the very slight curvature of the dispersed spectra on the CCD in this step. With the FORS instruments, this strategy works quite well (as opposed to LRIS on the Keck telescope). Significant sky residuals are only present around the very bright, narrow sky lines – where sky subtration is doomed anyway due to pixel saturation.

This procedure works only for our typical faint objects. Extremely bright objects can illuminate the whole slit, thus making correct sky subtraction impossible. Fortunately, in those (very few) cases identification was still possible due to the extremely high object signal.

5.5. *Fringe Removal*

In some cases (especially in MXU masks), we could take advantage of our dithering strategy to reduce further the effect of fringing and the sky residuals. As neither the fringe

pattern nor the sky residuals are significantly affected by the small (spatial) offsets of the telescope, we could, in some cases (with sufficient number of exposures in a given mask) exclude (most of) the object signal and create a fringe/sky residual template for each slit. Subtracting this from the frames resulted in an improved signal-to-noise ratio for the object spectra. Depending on the seeing conditions and the dithering offsets used, not all object signal was perfectly removed, thus the extracted spectra significantly underestimated the real spectra. As our primary goal was object identification, not spectrophotometry, this was an acceptable trade-off.

5.6. *Coadding the Frames*

After sky subtraction, all the slits were visually inspected to verify that the object is indeed in the 'good' region of the slit. This step was necessary since the applied small spatial offsets between the science exposures can result in objects falling too close to the slit edge (MOS blade corners are round, thus the slit is not usable there) or falling completely outside the slit.

After this visual screening, the *spatial* offset between different exposures of the same object was caculated based on the *world coordinate system* (WCS) information stored in the frame headers. The individual exposures were coadded (including the rejection of suspicious pixels or cosmic ray hits) after applying these spatial shifts. We only shifted the frames in the spatial direction and only by integer number of pixels. As the objects were sufficiently well sampled (the pixel scale was significantly smaller than the seeing), this step resulted in nearly negligible bluring of the spectra, while preserving the statistical properties of the exposures.

5.7. *Extraction*

Even though for *sky subtraction* we could safely ignore the slight curvature of dispersed spectra on the CCD, for the extraction of the object signal this is no longer possible. Therefore, we estimated the object position on the detector by collapsing at least 30 columns (more for really faint objects) in the dispersion direction and measuring the object center in the resulting profile. The object position was fitted typically with a second order polynomial as a function of column (wavelength).

Then an aperture *width* was visually determined. Except in special cases (e.g. blended objects), our aim was to include most of the object signal without adding too much sky (to

maximize the signal-to-noise ratio). A one dimensional spectrum was obtained using the 'optimal extraction' method of IRAF. This procedure calculates a weighted average in each column, based on both the estimated object profile and photon statistics.

5.8. *Wavelength Calibration*

Wavelength calibration was based on (daytime) arc calibration frames, using four arc lamps (a He, a HgCd and two Ar lamps) which provide a sufficient number of lines over the whole spectral range used (3889–9924Å).

The exact same aperture that was used for the science object was used for the arc frames. The resulting lines were first identified automatically. These identifications were then visually verified, and quite often significantly improved. In most cases, around 20 lines were located in the 3889–9924Å range, and fitted by a forth order polinomial, with a typical rms accuracy of 1Å or better. This accuracy is close to that expected from the nominal resolution of the instrument in our configuration. The object spectra were then wavelength calibrated and subsequently rebinned to obtain spectra with a linear wavelength scale.

We also examined the stability of the instrument by repeating the daytime calibrations on different days. No noticeable change was detected. In addition, we verified the wavelength calibration by checking the position of narrow skylines in science exposures – no discrepancy was found within our error estimates.

The wavelength calibration may not be accurate in the range outside the two extreme arc lines identified. As the FORS instruments use a grism, we had to resort to high order polynomial fits, which become unreliable when extrapolating the wavelength solution. In most cases, this is not an important issue, but there were a few unfortunate cases where major object features fell into unreliable regions (typically if the spectra were cut short on the blue side due to the position of the slit).

6. FLUX CALIBRATION

In this step, we *nearly* followed standard practices. The only significant necessary change arrised due to our choice of a non standard instrument configuration, namely not using the *right* order separation filters. Consequently, we nearly doubled our efficiency (taking only one exposure per object), but we then had to correct for second order diffracted light.

It is important to point out that we have to correct for this effect both for the science

and the spectrophotometric standard observations.

6.1. *Second Order Diffraction*

The first step was to determine the nature of the second order contamination. As this contamination affects the red part of the spectrum, where there are typically many lines present already from first order diffraction (in both arc and sky exposures), we used a special set of calibration frames: a 1.3 arcsec wide long slit, the standard arc lamps (He, HgCd, Ar) and a set of (dispersed) exposures through all available broad-band filters (U, B, V, R and I) as well as without any filter. Using the exposure without filter, we established the *first order* wavelength solution of this configuration. We verified that the use of the Bessel filters does *not* introduce any noticable shift in this solution. We were then able to identify the second order lines in the exposures taken through the broad-band filters. These identifications are shown in Table 3.

The comparison between the apparent fluxes in first and second order diffracted lines indicates that second order diffraction *can* be very strong, as much as 30% of the first order strength (especially in the blue part of the spectrum). This effect is made seriously worse by the quantum efficiency of the CCD. The overall quantum efficiency of the system peaks around 6000Å and declines relatively rapidly (see also Section 6.2). Because of this, a relatively weak second order contamination may become the dominant signal beyond 9000Å – due to to the much higher sensitivity of the pixels to these photons. For blue objetcs (for example spectral photometric standards), this problem is even worse: second order contamination can already start at 7000Å(due to the high UV flux of the object) and can contribute over 30% to the observed flux.

To correct for the second order diffraction, we first had to model it. Based on the identified arc lines, we adopted a second order wavelength solution in a linear form:

$$\lambda = 2.106\Lambda - 723\text{Å}, \tag{2}$$

where Λ is the real wavelength of the feature and λ is its apparent wavelength position observed in second order.

It should be noted that, as opposed to *grating* spectrographs where the coefficient is practically two and the shift is very small, a few times 10Å (Gutierrez-Moreno et al. 1994), FORS, which uses *grisms*, is significantly different, which makes the detection of second order diffraction harder, unless one takes the appropriate calibration data sets.

We assumed that the measured signal, $d(\lambda)$ is

$$d(\lambda) = f(\lambda)s(\lambda) + c(\Lambda)f(\Lambda), \tag{3}$$

where $s(\lambda)$ is the overall quantum efficiency of the system, Λ is the real, physical wavelength of features detected at λ in second order, $c(\Lambda)$ is the strength of the second order folded into the sensitivity function at Λ and $f(\lambda)$ is the real spectrum of the object.

Since we can not derive *two* functions ($s(\lambda)$ and $c(\Lambda)$) from a single measurement, either we determine the sensitivity, $s(\lambda)$, independently (e.g. observing a standard star through different order separation filters) or we use two independent measurements from observing two different standard stars. As the first option implies the introduction of an additional optical element (the filter), which can affect the strength of the second order diffracted signal (in fact comparing the flux ratios of the 3650.1Å arc line in Table 3 is a strong indication for this to be the case), we selected the latter aproach. We observed two standards with very different spectral shapes, LTT-3218 (Hamuy et al. 1992, 1994, a relatively red DA6 white dwarf) and HD49798 (Turnshek et al. 1990, a blue sdO6 subdwarf).

Given two different standards ($f_1(\lambda)$ and $f_2(\lambda)$), but identical instrument setups ($c(\Lambda)$ and $s(\lambda)$), we can write

$$c(\Lambda) = \frac{d_1(\lambda) - f_1(\lambda)s(\lambda)}{f_1(\Lambda)} = \frac{d_2(\lambda) - f_2(\lambda)s(\lambda)}{f_2(\Lambda)}, \tag{4}$$

which we can solve for $c(\Lambda)$:

$$c(\Lambda) = \frac{d_1(\lambda)}{f_1(\Lambda)} \left(1 - \frac{\alpha(\Lambda) - \beta(\lambda)}{\alpha(\Lambda) - \alpha(\lambda)}\right), \tag{5}$$

where $\alpha(\lambda) = f_2(\lambda)/f_1(\lambda)$ (known a'priori) and $\beta(\lambda) = d_2(\lambda)/d_1(\lambda)$ (known from observations).

The derived $c(\Lambda)$ indicates that the contamination is completely negligible up to 6300Å. Up to 7500Å it is somewhat stronger, but typically still negligible as this wavelength corresponds to up to 3800Å in first order, where the CCD is very inefficient. Between 7500 and 9000Å, the effect is strong (12% to 3% of the first order instrumental flux shows up in second order). Depending on the object type (whether it is a blue or red object) and the wavelength of interest (as this result should be folded with the system quantum efficiency, which is increasing with wavelength for second order diffracted photons and decreasing for first order diffracted photons in this range) this may or may not be a strong effect – this decision should be made for each observing program. Beyond that this effect could not be estimated as one of our standards is measured only to 8700Å. As in this range the CCD QE

is dropping very sharply, while the first order QE is very high, second order contamination *must* become the dominant source of signal at some wavelength.

The effect of the second order diffraction is demonstrated in Figure 3, using a blue spectrophotometric standard star, Feige110 (Hamuy et al. 1992, 1994; Oke 1990).

6.2. *Overall Quantum Efficiency of the System*

The overall throughput of the system was determined using a set of spectro photometric standard stars: LTT-377, LTT-3218, LTT-7379, LTT-7987, LTT-9239 (Hamuy et al. 1992, 1994), HD49798 (Turnshek et al. 1990) and Feige110 (Hamuy et al. 1992, 1994; Oke 1990). These objects were observed repeatedly over a wide range of airmasses during each run, using a simulated very wide ($\sim 5''$) long slit, using the robotic mask facility of the FORS instruments (combining 3 slits).

The observations were reduced nearly the same way as science observations. Second order diffraction was removed as outlined in Section 6.1. The measured spectra (in instrumental units) were compared to the published physical spectra – excluding regions with sharp features in the objects and sharp telluric absorption features in the atmosphere. A smooth sensitivity curve was fitted to the data points. As we were using about the whole wavelength range of the CCD, this fit was done in four parts: 3000-4000Å (or 3500-4000Å if the OG375 order separation filter was used during the run), where the throughput raises very sharply and only a 10% accuracy was achieved, between 4000-5000Å, where the throughput is still rising fast (about 4% accuracy), between 5000-8000Å (2% accuracy) and finally between 8000-9500Å, where the accuracy drops again to around 10%. These four data sets were used to construct the sensitivity curve for each observing run and each configuration.

As the Paranal Observatory does not have sufficient data collected to measure an accurate spectroscopic extinction curve, we used the curve published by the Cerro Tololo Inter-American Observatory (CTIO), after verifying, using our standard observations, that the curve is very close to that estimated for Paranal.

This calibration was applied to all measured program spectra. We also corrected for atmospheric extinction using the CTIO extinction curve. The accuracy of the resulting flux calibrated (but not absolute calibrated – see below) spectra is mainly constrained by the signal-to-noise ratio of the object signal in the 4000-8500Å range (the inaccuracy due to the sensitivity function is negligible in this range). Outside this range the flux calibration can introduce significant structures as the throughput of the whole system drops very rapidly, thus even very small inaccuracies in the wavelength calibration of the object spectra result

in significant over or underestimation of the physical spectra. It is also important to point out that no attempt was made to correct for telluric absorption: For the vast majority of our program objects, telluric absorption completely eliminates the signal (between 7600-7630Å, 7170-7350Å and 6868-6890Å), thus a correction is not practical. For the few brighter objects, this correction would have been possible, but was deemed unnecessary for identification of the sources.

6.3. *Absolute Calibration – Estimating the Slitloss*

The purpose of our observations was to identify as many X-ray sources as possible with the telescope time available. Therefore, no effort was made to collect data necessary for *absolute* calibration of the spectra measured. Even though we did *not* use an elaborate program designed for spectrophotometry, we can still estimate the accuracy of our derived fluxes.

The most important effect to be considered is slit-loss. To maximize the S/N of the data, we tried to match the slit width to the expected seeing of the observations. Therefore, a significant fraction of the light from the object was excluded, but this was more than balanced by the large reduction in the sky background, and thus the increase in the S/N of the source.

We can easily estimate the effect of slit-losses from the high accuracy broad-band photometry. Using the flux calibrated spectra, we can directly calculate the AB-magnitude of the object in any filter:

$$m_{AB} = -2.5 \log \frac{\int d(\log \nu) f_\nu S_\nu}{\int d(\log \nu) S_\nu} - 48.60, \tag{6}$$

where f_ν is the energy flux per unit frequency, S_ν is the overall throughput of the system (telescope and instrument) in arbitrary units.

The first step is to select the filter curve to use, S_ν. In practice, no system can replicate the canonical Cousins-Johnson filter curves *exactly*. Even a perfect filter response curve would be distorted by the non flatness of the CCD detector. In many cases a slight deviation from this filter response curve is acceptable, assuming that the spectrum of the object is smooth and the slope is not very different from the slope of Vega. Unfortunately, these assumptions do not hold for most of our objects as a significant fraction of the flux is in very sharp features. Therefore, we have to use the effective filter curve of *our* system used to derive the broad-band magnitudes. Fortunately, the Bessel filter set used by ESO is a sufficiently good approximation of the Cousins-Johnson filters and the quantum efficiency

curve of the FORS detectors being relatively flat, this correction would only amount to a fraction of a percent and can be safely ignored. Therefore, we used the published ESO filter response curves folded over the quantum efficiency of the detectors as system throughput, S_ν. To convert to Vega magnitudes, we calculated the AB magnitude of Vega from its spectra (Fukugita et al. 1996). The resulting slitlosses are presented in Table 4 for point sources for each mask. We also checked if the slitloss depends on wavelength (by comparing different broad-band magnitudes) but found no significant effect.

6.4. *Reddening Correction*

To calculate the effect of reddening due to our Galaxy on the spectra, we used the $100\mu m$ maps (Schlegel et al. 1998). In the direction of the CDFS, $l = 223.5°$, $b = -54.4°$, the color excess is $E(\mathrm{B-V}) \approx 0.008$. Assuming the canonical value, $R_\mathrm{V} = 3.1$ for the ratio of extinction in the V-band to the color excess (Cardelli et al. 1989), the extintion is $A(\mathrm{U}) \approx 0.04$ and $A(\mathrm{I}) \approx 0.01$. As this extinction is heavily dependent on the choice of R_V, this correction was *not* applied to the data, introducing an artificial tilt in all spectra on the order of a few percent.

The AGN line strengths were not corrected for absorption lines from the *host* galaxy (Ho et al. 1993) as the S/N of our faint spectroscopic sample is too low. Consequently, the very few optical identifications based on line ratios are possibly affected by this effect.

Correcting for reddening by the AGN host galaxy would require to estimate the extinction using the X-ray spectral information. This correction is deferred to a later paper concentrating on X-ray spectral analysis of the CDFS sources based on the Chandra and XMM-Newton data.

7. REDSHIFT DETERMINATION AND THE SPECTROSCOPIC SAMPLE

7.1. *Redshift and Luminosity Determination*

The first step toward the classification of the spectroscopically observed sources was their *redshift* determination. In the vast majority of the cases this was done through the identification of prominent features, typically the 4000Å break and the Ca II H and K absorption, Balmer lines or emission lines (e.g. Ly-α, C IV, C III], Mg II, [O II], etc.). In case of prominent emission lines, the wavelength ratio of the line centers was used to identify these features. In cases of single emission line objects with no additional feature, this line

was usually identified as either [O II] or Ly-α, depending on the continuum spectral shape. Naturally, these are not secure classifications, the quoted redshifts should only be used as an educated guess to optimize follow-up observations.

The redshift identifications are summarized in Table 5. The 'No' column refers to our internal id of the *X-ray* source – this is the *unique detection ID (XID)* in the published catalog (Giacconi et al. 2002). In cases of multiple counterparts, a letter is appended to this number to distinguish between the optical candidates. Extended X-ray objects are marked with a star. When an object was observed repeatedly, multiple entries are given in the table. Altogether 249 X-ray sources were observed, of which one point source belongs to the small additional sample given in Table 1, and 15 are extended X-ray sources. In 17 cases, the slit was centered on the X-ray position for the search of strong, narrow emission lines although no counterpart was detected in the R-band.

The *mask* column is our internal name used to identify the set of observations used for individual objects. Multiple mask names indicate that during the observations some slits were reconfigured, but the slit used for the object was identical during the set of observations. The relevant observing conditions and configuration can be found in Table 4 (exposure time, slit width, seeing, etc.).

The two position columns (right ascension and declination) give the coordinates of the *optical* object, *not* those of the X-ray source. Astrometry is based on the USNO (Monet et al. 1998) reference frame, just like the X-ray positions in Giacconi et al. (2002) and the astrometric accuracy is better than $0.2''$.

Whenever available, we also provide broadband optical information, an R-band magnitude and R−K color (both in Vega magnitudes). If no R-band magnitude is given, it implies that our FORS imaging data is not deep enough to measure the magnitude of the object (all program objects are covered by the FORS R-band survey). The lack of R−K color can be due to our limited near-infrared coverage (*NA* entries).

Assuming (throughout this paper) an $\Omega_m = 0.3$, $\Omega_\Lambda = 0.7$ universe and $H_0 = 70$ km s^{-1} Mpc^{-1} (Spergel et al. 2003) the total X-ray intrinsic luminosity of the object, $L_{\rm X}$, in erg s^{-1}, is (Carroll et al. 1992)

$$L_{\rm X}(f_{\rm X}, z) = 4\pi f_X \left(\frac{c(1+z)}{H_0\sqrt{|\Omega_k|}} \mathrm{sinn}\left(\sqrt{|\Omega_k|} \int_0^z \left((1+\zeta)^2(1+\Omega_m\zeta) - \zeta(2+\zeta)\Omega_\Lambda \right)^{-1/2} d\zeta \right) \right)^2 \quad (7)$$

where $f_{X,tot}$ is the *observed* X-ray flux in the 0.5-10 keV band. The sinn(x) function is sin(x) for $\Omega_k < 0$, sinh(x) for $\Omega_k < 0$ and simply x for $\Omega_k = 0$, where $\Omega_k \equiv 1 - \Omega_m - \Omega_\Lambda$. In case of

$\Omega_k = 0$, the two $\sqrt{|\Omega_k|}$ terms disappear. This flux being the *observed* X-ray flux, it should be interpreted as a lower limit for the *intrinsic* X-ray flux of the object due to potentially strong obscuration of the source.

If we assume that $\Omega_k = 0$ (i.e. $\Omega_m + \Omega_\Lambda \equiv 1$), we can rewrite this equation as

$$L_{\rm X}(f_{\rm X}, z) = 4\pi f_X \left(\frac{c(1+z)}{H_0} \left(\int_0^z \left((1+\zeta)^3 \Omega_m + \Omega_\Lambda \right)^{-1/2} d\zeta \right) \right)^2 \tag{8}$$

Introducing $x = (1+\zeta)(\Omega_m/\Omega_\Lambda)^{1/3}$, this simplifies to

$$L_{\rm X}(f_{\rm X}, z) = \frac{4\pi f_X c^2 (1+z)^2}{H_0^2 \Omega_m^{2/3} \Omega_\Lambda^{1/3}} \left(\int_{(\Omega_m/\Omega_\Lambda)^{1/3}}^{(1+z)(\Omega_m/\Omega_\Lambda)^{1/3}} \frac{dx}{\sqrt{x^3+1}} \right)^2 \tag{9}$$

The above integral can be evaluated in terms of incomplete elliptical integrals of the first kind. We also give below an analytical fit for flat cosmologies (Pen 1999) with $\Omega_m = 0.3$:

$$d_L = \frac{c(1+z)}{H_0} \left(3.308 - 3.651 \left(0.207 + 0.446(1+z) + 0.757(1+z)^2 - 0.204(1+z)^3 + (1+z)^4 \right)^{-1/8} \right) \tag{10}$$

In Figure 4 we show the correction to the calculated X-ray luminosity for slightly different cosmologies. We also show the difference between luminosities calculated using current cosmological parameters and the (now obsolete) $\Omega_m = 1$, $\Omega_\Lambda = 0$, $H_0 = 50$ km s^{-1} Mpc^{-1} cosmology,

$$L_{\rm X} = 4\pi f_{X,tot} \left(\frac{2c}{H_0} \left(1 + z - \sqrt{1+z} \right) \right)^2 \approx 1.72 \times 10^{58} {\rm cm}^2 f_{X,tot} \left(1 + z - \sqrt{1+z} \right)^2, \tag{11}$$

The HR column contains the already published (Giacconi et al. 2002) hardness ratios for each object, $HR = (H - S)/(H + S)$, where H and S are the net count rates in the hard (2-10 keV) and soft (0.5-2 keV) band, respectively. It is important to point out that the hardness ratio is defined in *instrument* counts (for Chandra ACIS-I), thus for different X-ray telescopes or instruments, it should be converted using their specific energy conversion factors.

The z column gives our best redshift estimate. The selected low spectral resolution leads to an uncertainty in the redshift determination of ± 0.005. For broad emission line objects the uncertainty is significantly higher. The quoted redshift value *always* refers to the particular observation of the object, thus, there can be slight discrepancies between observations of the same object or missing redshift values for some masks.

7.2. *The Optical and X-ray Classification*

The classical/optical and X-ray classifications of the objects are discussed in details in Section 10 and given in Table 5.

Based on purely the optical spectra, we define the following *optical* object classes:

- *BLAGN*: Objects with emission lines broader than 2000 km s^{-1}. This classification implies an optical type-1 AGN or QSO, as discussed in Section 10.
- *HEX*: Object with unresolved emission lines *and* exhibiting high ionization lines or emission line ratios indicating AGN activity. These objects are dominanly optical type-2 AGNs or QSOs, but in a few cases the optical type-1/2 distinction is not possible based on the data.
- *LEX*: Objects with unresolved emission lines consistent with an H II region-type spectra. These objects would be classified as normal galaxies based on the optical data alone as the presence of the AGN can not be established.
- *ABS*: a typical galaxy spectrum showing only absorption lines.
- *star*: a stellar spectrum.

Our main classification is solely based on the observed X-ray properties ($L_{\rm X}$ and HR) of the sources and is summarized below. The type-1 AGN/QSO are soft X-ray sources, while the type-2 AGN/QSO are hard, absorbed X-ray sources (for the relationship between hardness ratio and absorption see e.g. Mainieri et al. 2002). The AGN and QSO classes cover different ranges of X-ray luminosities.

- *QSO-1*: $L_{\rm X}$(0.5-10 keV)$\geq 10^{44}$ erg s^{-1} and $HR \leq -0.2$.
- *AGN-1*: $10^{42} \leq L_{\rm X}$(0.5-10 keV)$< 10^{44}$ erg s^{-1} and $HR \leq -0.2$.
- *QSO-2*: $L_{\rm X}$(0.5-10 keV)$\geq 10^{44}$ erg s^{-1} and $HR > -0.2$.
- *AGN-2*: $10^{41} \leq L_{\rm X}$(0.5-10 keV)$< 10^{44}$ erg s^{-1} (lower limit smaller than for the AGN-1 population to account for substantial absorption) and $HR > -0.2$.
- *gal*: $L_{\rm X}$(0.5-10 keV)$< 10^{42}$ erg s^{-1} and $HR < -0.2$.
- *star*: this class is defined from the optical spectra and/or proper motions.

Throughout the paper we call X-ray type-1/2 AGNs and QSOs together X-ray type-1/2 *objects*.

7.3. *The Spectroscopic Sample*

The *quality* flag, Q, indicates the reliablity of the redshift determination. $Q = 2.0$ indicates a reliable redshift determination, a value of 0.0 indicates no success. $Q = 1.0$ indicates that we clearly detect *some* feature (typically a single narrow emission line) in the spectrum that cannot be identified securely. In a few cases, $Q = 0.5$ is used when there is a hint of some spectral feature. This quality flag *only* refers to the reliability of the spectroscopic classification. The identification of the X-ray sources is unambiguous for single counterparts in the X-ray error circles, and for cases with reliable redshift identification we then use a $Q = 2.0+$ quality flag. X-ray sources with multiple counterparts are discussed below. The $Q = 2.0+$ objects define our spectroscopically identified X-ray sample.

Finally, the *comments* column contains additional information relevant to the particular observation. The most common ones are a limited wavelength coverage (the full wavelength range is not available due to the positioning of the slit) and the detection of high ionization lines. We also include information necessary to apply the stricy Seyfert definition (Khachikian & Weedman 1974) to optically classify our objects.

Among the X-ray sources with multiple optical counterparts, the identification is considered as highly reliable in the following 13 cases: X-ray type-1 QSO/AGN (XID 30, 101), X-ray type-2 QSO/AGN (XID 56, 201, 263), and interacting galaxy pairs (XID 98, 138, 580). Four of the remaining X-ray sources (XID 553, 567, 582, 620) are the brightest objects in the X-ray error circles, only detected in the soft band and at moderate redshift with H II region-type spectra, thus most likely the X-ray counterparts. The last source (XID 189) is detected in the hard band only, has R−K > 5 and is the brigthest, best centered counterpart (the additional counterparts are very faint, R > 25). These objects are included in the spectroscopically identified X-ray sample.

As the CDFS has been observed by various teams and covered by wide surveys (2dF and Tycho), we could include in our sample additional spectroscopic redshifts. Four sources (XID 39, 95, 103, 116) were in fact already published in the CDFS 130 ksec paper (Giacconi et al. 2001). Eight objects (XID 33, 38, 149, 171, 204, 526, 563, 600) are covered by the K20 survey (Daddi et al. 2003, Cimatti, private communications) and three (XID 90, 92 and 647) by the COMBO-17 survey (Wolf, private communication). Three sources have optically bright, low z counterparts in the 2dFGRS (Colless et al. 2001). One ot them, XID 84 (TGS243Z005), has a soft X-ray spectrum and appears to be a normal X-ray galaxy. The other two sources, XID 247 (TGS243Z011) and XID 514 (TGS243Z010), have hard spectra, luminosities $L_{\rm X}$(0.5-10 keV) $\sim 10^{40}$ erg s^{-1} and are off-centred within the parent galaxy: these properties are similar to those of the brigther, ultraluminous compact X-ray sources (ULXs) detected in nearby spiral galaxies (Makishima et al. 2000). Finally, one source

(XID 549), optically very bright, is identified with an object (TYC 6453-888-1) from the Tycho Reference Catalog (Hog et al. 1998), that has a clear proper motion (7.6±2.1 and 15.7±1.7 mas/yr in right ascension and declination, respectively) and is thus a star in the Milkyway.

The spectroscopically identified X-ray sample comprises 137 sources of which 15 are fainter than R = 24.0. Among the brighter objects, there are seven extended X-ray sources at $0.6 < z < 1$ (XID 132, 138, 249, 560, 566, 594, 645: Giacconi et al. 2002). In addition, there are 24 X-ray sources with secure identifications but only tentative redshifts ($Q = 0.5$ and 1.0 cases).

8. FINDING CHARTS AND SPECTRA

Figure 5 gives the finding charts and *all* the spectra obtained for each of our program objects.

Finding charts are $20'' \times 20''$ in size, centered on the X-ray position with its 2σ position error circle. Individual contrast levels are chosen in each case to give as much information as possible. If multiple optical counterparts are present in (or around) the error circle, they are marked and labeled. The underlying optical images are our R-band FORS images.

Next to the finding charts, we show the associated spectra. For cases of repeated observations, all the data are shown. In the plots, we mark the features used for the redshift determination.

In cases of marginal line detections, we also examined the sky-subtracted coadded two-dimensional frames to confirm/infirm the presence of the feature. These images are not included in this paper, but are available through our web-site, http://www.mpe.mpg.de/CDFS.

9. FIELD SAMPLE

During our survey, we also collected a large number of field object spectra. These were objects either accidentally covered by some of our slits, or observed in slits that could not be placed on X-ray counterpart candidates due to geometrical constraints, or stars used to align the MXU masks. Consequently, this sample is not representative of the field population.

The results of these observations are summarized in Table 7. We give the object position, mask name, R-band magnitude (when available), redshift, redshift quality flag, very crude classification and optional comments relevant to the observation. The full dataset (spectra

and finding charts) is available on our web site (http://www.mpe.mpg.de/CDFS).

10. X-RAY VERSUS OPTICAL CLASSIFICATION

Seyfert galaxies (Seyfert 1943) were originally defined (Khachikian & Weedman 1974) as a recognizable galaxy (on *Sky Survey* prints) that have broad (> 500 km s^{-1}) emission lines arising in a bright, semi-stellar nucleus. Seyfert galaxies were subdivided into class 1 and class 2, depending on the width of the Balmer lines, compared to that of forbidden lines. For line widths $200 < FWHM < 500$ km s^{-1}, additional criteria were applied, based on emission line ratios (e.g. Osterbrock 1989) to establish the Seyfert nature of a galaxy. With the emergence of the unified AGN model (Antonucci & Miller 1985), it is now widely accepted that these two Seyfert classes are not distinct, but form a continuous distribution between the two extremes and a large number of intermediate classes were introduced since the original definition. Applying these classical definitions poses very serious problems for the study of faint X-ray sources.

At high redshifts, the Balmer lines are no longer in the optical range: the two strongest Balmer lines, Hα and Hβ, are redwards of 8500Å for $z > 0.3$ and 0.75, respectively. This problem was overcome by extending the original definition to *permitted* lines in the UV range from Mg II$\lambda\lambda$2796,2803 to Lyα (see e.g. Schmidt et al. 1998), thus allowing an optical classification of objects up to $z \sim 6.5$. Another difficulty stems from the fact that most of the objects associated with faint X-ray sources are at intermediate redshifts and, thus, are comparable in size to the seeing achievable with ground-based optical telescopes. As a consequence, we can only study the *integrated* emission from these objects, as opposed to *nuclear* emission from local Seyfert galaxies. Consequently, the nuclear emission can be 'hidden' in the stellar light coming from the host galaxy. The study of local Seyfert galaxies confirms that about 60% of the local Seyfert type-2 galaxies would *not* be classified as Seyfert-2, if only the *total* emission were available (Moran, Filippenko & Chornock 2002).

Moreover, an obvious challenge in applying the classical Seyfert definition for faint objects is merely to recognize that they are AGNs. The main optical classes introduced in this paper for extragalactic sources are: 1) BLAGN – $FWHM$(permitted lines)$>$ 2000 km s^{-1}, 2) HEX – unresolved emission features but presence of high excitation lines not found in H II regions (e.g. [Ne V]λ3425, He IIλ1640), suggesting AGNs of the optical type-2 class, 3) LEX – H II region-type spectrum, 4) ABS – typical galaxy absorption line spectrum. For the 130 extragalactic X-ray sources with secure redshift identification, there are 32 BLAGN, 24 HEX, 54 LEX and 21 ABS sources, thus 57% LEX+ABS objects. But among the latter (optically dull), it should be noted that there is a large number of luminous X-ray sources.

To overcome the limitations of the classical/optical definition of AGN, we follow the unified AGN model introduced by Antonucci & Miller (1985) and classify an object as an AGN *if it has (nuclear) emission stronger than expected from stellar processes in normal galaxies*. This emission is likely to be produced by strong accretion onto supermassive objects, most probably black holes. A clear signature of the presence of this accretion is a high X-ray luminosity.

An X-ray classification requires first to introduce a conservative lower limit on the (unabsorbed) absolute X-ray luminosity of AGNs. Local, well studied starburst galaxies have X-ray luminosities in the 0.5-10 keV band typically below 10^{42} erg s^{-1} (Rosati et al. 2002; Alexander et al. 2002). Thermal haloes of galaxies and intragroup/cluster gas can have higher X-ray luminosities but, in Chandra data, they are spatially resolved and detected only in the soft band thus, at intermediate redshifts, they become fainter than 10^{42} erg s^{-1} in the 0.5-10 keV band. Accordingly, objects with $L_{\rm X}$(0.5-10 keV) $\geq 10^{42}$ erg s^{-1}, should be classified AGNs. There are 20[20] HEX, 31[53] LEX and 9[12] ABS (excluding XID 645 which only shows extended X-ray emission) high $L_{\rm X}$ sources with secure[secure+tentative] redshift identification respectively. Thus the optical classification completely fails to identify as AGN 42% (LEX+ABS fraction) of the luminous X-ray sources (96), or altogether 54% if we include the tentative redshift identifications (120). In these objects, optical extinction of the nuclear component by dust can be very high, and/or the host galaxy can outshine the central AGN (Lehmann et al. 2000, 2001).

The X-ray luminosity is also used to separate the sources of the AGN class, $10^{42} \leq L_{\rm X}$(0.5-10 keV) $< 10^{44}$ erg s^{-1}, from those of the QSO class, $L_{\rm X}$(0.5-10 keV) $\geq 10^{44}$ erg s^{-1}.

Secondly, following the unified AGN model, we can also define two AGN classes by using the hardness ratio, a parameter sensitive to X-ray absorption which can be measured even for faint objects. In Figure 12, we give the expected hardness ratios for AGNs with power law X-ray spectra, selecting a photon index Γ=2 and different absorption levels. Unabsorbed sources have $HR \approx -0.5$, independent of z. This is indeed the case for all the BLAGNs; their hardness ratios are in the range $-1.0 \leq HR \leq -0.2$, except for one BAL QSO. The scatter is easily explained by introducing different slopes for the X-ray spectra, together with statistical errors associated with low number counts in the X-ray bands. The harder spectra ($HR > -0.2$) are fully consistent with *absorbed* power law spectra. Significant intrinsic absorption, $10^{21.5} < N_{\rm H} \lesssim 10^{23.5}$ cm^{-2}, has indeed already been found for the type-2 AGN population (Mainieri et al. 2002; Barger et al. 2002). Figure 12 shows that, assuming $\Gamma = 2$, intrinsic absorption ($HR > -0.2$) can be detected up to $z = 0.25$, 2.1 and 3.9 for $N_{\rm H} = 10^{22}, 10^{23}$ and 3×10^{23} cm^{-2}, respectively. Thus the hardness ratio can be used to separate the unabsorbed sources, X-ray type-1: $HR \leq -0.2$, from the absorbed ones, X-ray

type-2: $HR > -0.2$. Indeed, in the Chandra and XMM-Newton deep surveys, most of the harder X-ray sources are optical type-2 AGN with an increasing fraction of absorption at decreasing X-ray flux (Barger et al. 2001a,b; Hasinger et al. 2001; Rosati et al. 2002; Mainieri et al. 2002). Among this class of objects, there are a few bright type-2 QSOs but the majority of the sources are type-2 AGNs at $z \lesssim 1$ (see e.g. Hasinger 2002). It should be noted that an X-ray classification based on the hardness ratio might be misleading for some high-redshift objects: an increasing absorption makes the sources harder, while a higher redshift makes them softer. Consequently, some high-redshift absorbed/type-2 sources may be mistakenly identified as type-1, but not the other way around.

A consistent X-ray classification should use the intrinsic luminosity. As mentioned above, hard sources ($HR > -0.2$) at $z \sim 0.25$ have absorbing column densities $N_{\rm H} \geq 10^{22}$ cm^{-2} and thus their de-absorbed flux in the observed 0.5-10 keV band is at least 5 times larger than the observed flux. Consequently, *hard* objects ($HR > -0.2$) with lower luminosities ($(10^{41} < L_{\rm X}(0.5\text{-}10 \text{ keV}) < 10^{42}$ erg s^{-1}) can be classified as X-ray type-2 AGN. Four additional objects (XID 55, 525, 538, 598) are thus classified as low $L_{\rm X}$ X-ray type-2 AGNs.

In Figure 13, we show the hardness ratio versus the observed X-ray luminosity for all the sources with secure redshift, for both the optical classification (left panel) and the X-ray one (right panel). No source with a very high X-ray luminosity is present in this diagram: this is, at least in part, a selection effect of pencil beam surveys. We now compare the optical and the X-ray classifications.

- Of the 32 BLAGNs in our sample, all are X-ray type-1 objects, except the BAL QSO (XID 62, $HR = -0.07$) which is an X-ray type-2 QSO.

- Among the HEX population (24 objects), there are 16 X-ray type-2 AGNs/QSOs (including one low $L_{\rm X}$ source: XID 55) for which X-ray absorption is indeed associated with optical obscuration. There are eight X-ray type-1 AGNs/QSOs or galaxies, of which four at $z \geq 1.6$ (XID 31, 117, 563, 901) with permitted emission lines no broader than $\sim$ 1500 km s^{-1}. These four sources may be partly absorbed ($N_{\rm H} = 10^{22}$-10^{23} cm^{-2}), thus misclassified as X-ray type-1: the presence of probable X-ray absorption should be confirmed by X-ray spectral analysis, whenever possible. In the spectrum of XID 34a, we do not detect permitted lines. The remaining three HEX objects are X-ray galaxies (XID 98a, 175b, 580a), two being members of interacting pairs, and all have $HR = -1.0$. They could be either low $L_{\rm X}$ type-1 AGN or, in the case of the interacting pairs, shocks might be at the origin of the [Ne V] emission.
  There is a high fraction, 42%, of $z > 2$ sources among the HEX class as compared to 25% in the BLAGN class.

- The LEX population comprises 54 sources with secure redhift identification, of which 9 and 24 X-ray type-1 and type-2 (including two low $L_{\rm X}$ sources: XID 525, 538) AGNs/QSOs, respectively. The optical classification thus fails to identify as AGN 61% of this population. Among the remaining sources, there are 21 X-ray galaxies including one ULX (XID 247) at $z = 0.038$ with a hard spectrum, $HR = 0.31$ (see Section 7). In the LEX class, there are only two high luminosity sources of the X-ray QSO class and no objects at high redshift ($z > 1.5$). A few X-ray type-2 AGNs might be of the HEX class but, due to the low S/N (< 5 per resolution element) of their optical spectra, high excitation lines could be below the detection threshold.
  For most X-ray type-2 AGNs, both the broad (BLR) and narrow (NLR) emission line regions could be obscured by dust absorption. Alternatively, the obscuring region may fully cover the central UV source and the BLR, preventing photo-ionization of external regions thus the existence of a NLR. The AGN nature of all the X-ray type-1 sources ($0.53 \leq z \leq 1.03$) is difficult to ascertain from the optical data alone as the Hα line is outside the observing range for redshift higher than 0.4. For six of them, the expected Mg II emission line is within the observed range (i.e. $0.4 < z < 2.2$) and away from strong sky lines, but the S/N is not high enough to detect a weak broad line; in one source (XID 138), a broad Mg II emission line may be present, although at a low significance level. For comparison, Mg II is often seen in absorption or with a P Cygni profile in star-forming galaxies (Kinney et al. 1993).

- There are 21 sources in the ABS class of which one and 9 X-ray type-1 and type-2 (including one low $L_{\rm X}$ source: XID 598) AGNs. Thus 48% of the AGN population in the ABS class is missed by the optical classification. All the sources of the X-ray AGN class are at $z < 1.2$. The 11 X-ray galaxies are all at $z < 0.8$ and have soft spectra ($HR < -0.7$) except one object (XID 514), a ULX at $z = 0.103$ with $HR = -0.14$ (see Section 7).

The comparision of the two classification schemes are summarised in Table 8.

The proposed X-ray classification is more successful than the classical/optical one in revealing the presence of black hole activity, whatever the amount of dust obscuration from the central and/or external parts of the nuclear region. Thus, we use this classification throughout the paper unless otherwise stated. For comparison, we also give the optical classification in Table 5. The latter may be more appropriate in studies that aim to extrapolate the classical Seyfert definition to faint AGNs.

It should be noted that using the X-ray classification is mandatory to properly identify the X-ray normal galaxies among the LEX+ABS optical class. This population provides

another means to derive the star formation history of the universe, in addition to the methods using radio or optical data.

11. CLUSTERS AND EXTENDED SOURCES

Of the 19 extended sources detected in the CDFS (Giacconi et al. 2002), 15 were observed in our survey. In 5 cases (XID 37, 147, 522, 527 and 581) no spectroscopic identification was possible and in one case (XID 132) only a low quality identification was obtained. In two cases (XID 116 and 514) the diffuse X-ray emission could be ascribed to thermal halos of nearby galaxies. In general, most of the remaining extended sources span the regime of galaxy groups (with luminosities of a few$\times 10^{42}$ erg s^{-1}) down to X-ray luminosities typical of thermal halos around single early-type galaxies. In some cases, either the hardness ratio or the optical identification suggest the coexistence of a thermal halo with an AGN component (e.g. XID 138). In Figures 6-11 we show K-band images of the identifield clusters/groups with overlaid Chandra contours (2.5,3,4,5,7,10 σ above the local background) in the [0.5-2] keV band. We also mark objects with concordant redshifts (as listed in Table 5).

Specifically, XID 566,594,645 are ordinary groups showing however a range of surface brightness profiles (see Figs. 9,10,11). XID 566 and 594 belong to the large scale structure at $z \simeq 0.73$ (see below). XID 249, for which we have two concordant redshifts with $< z >= 0.964$, is clearly extended with a harder component (Fig. 7). XID 138 was identified as a close pair of AGN at $z = 0.97$, surrounded by a soft halo. In two cases, XID 511 and 560, we identified only one galaxy per source, making it difficult to ascertain the existence of a group.

12. REDSHIFT DISTRIBUTION

The spectroscopically identified CDFS sample comprises 135 X-ray sources, including five stars. Reliable redshifts can be obtained typically for objects with R < 25.5, however, some incompleteness already sets in around R ~ 23. For the R$<$24 sample (199 objects), 120 (including five stars) of the 159 observed X-ray sources have been spectroscopically identified, thus a success rate of 75% and a completenes of 60%. The sources with inconclusive redshift identification cover a wide range of hardness ratios. In Figure 14, we show the spatial distribution of the sources with spectroscopic observations as well as those not observed. The latter lie predominantly in some of the outermost parts of the CDFS.

The histogram of the redshift distribution of the X-ray sources is shown in Figure 15.

A preliminary version of this diagram was given by Hasinger (2002). There is an excess of objects in two redshift bins, revealing large-scale structures of X-ray sources(Gilli et al. 2003), similar to that found in the CDFN (Barger et al. 2002). These redshift spikes are populated by X-ray type-1 and type-2 AGNs as well as a few X-ray galaxies. There are 18 X-ray sources within 2000 km s^{-1} of $z = 0.674$, of which one (XID 201b) is fainter than R of 24; these objects are distributed loosely across a large fraction of the field and should thus trace a sheet-like structure. The spike centered on $z = 0.734$ is narrower and includes 16 X-ray sources within 1000 km s^{-1} of the mean redshift, all brighter than R of 24. In both structures, about 70% of the sources are X-ray type-2 AGNs (+ X-ray galaxies). The brightest X-ray cluster (XID 594) belongs to the $z = 0.73$ spike. A few field galaxies, possibly associated with this X-ray cluster and other extended X-ray sources (of which XID 645 at $z = 0.679$), are given at the end of Table 5. The $z = 0.67$ and 0.73 structures are also traced by galaxies from the ESO K20 survey which covers $\sim$1/10 of the Chandra field (Cimatti et al. 2002a,b): they are populated by 24 and 47 galaxies respectively (Gilli et al. 2003). The K20 structure at $z = 0.73$ is dominated by a standard cluster with a central cD galaxy (identified with the extended X-ray source XID 566), whereas the K20 galaxies at $z = 0.67$ are uniformaly distributed across the field. There is also evidence of higher redshift, narrow spikes in the distribution of the X-ray sources at $z = 1.04$, 1.62 and 2.57; that at $z = 1.04$ is also present in the K20 sample (Gilli et al. 2003).

At $z > 2$, there are similar numbers of X-ray type-1 (5) and type-2 (7) QSOs. The relative paucity of high z X-ray type-2 AGN (1/6) could arise from an observational bias as type-2 sources are optically fainter than the type-1 population. At $z < 1$, the higher number of X-ray type-2 over type-1 sources is mainly due to the large concentration of X-ray type-2 sources within the $z = 0.67$ and 0.73 structures.

The redshift distribution of the bright sample with 60% redshift identification completeness can be compared to those predicted by models. The X-ray background population synthesis models (Gilli et al. 2001), based on the AGN/QSO X-ray luminosity function and its evolution, predict a maximum in the AGN/QSO redshift distribution at $z \sim 1.5$. Contrary to these expectations, accretion onto black holes is still very important at $z < 1$: indeed 88 (68%) of the 130 CDFS extragalactic X-ray sources are at $z < 1$ and the redshift distribution peaks around $z \sim 0.7$, even if the normal starforming galaxies are removed from the sample. Similar results were found for the CDFN (Barger et al. 2002). This clearly demonstrates that the population synthesis models will have to be modified to incorporate different luminosity functions and evolutionary scenarios for intermediate-redshift, lower-luminosity AGNs.

Moreover, the CDFS redshift distribution does not confirm the prediction by Haiman

& Loeb (1999), that a large number (∼100) of QSOs at redshifts larger than 5 should be expected in any ultra deep Chandra survey. The highest redshift in the CDFS thus far is 3.70, while there are two confirmed and one uncertain high redshift sources in the CDFN at $z = 4.14, 5.19$ and $z = 4.42$, respectively (Barger et al. 2002, 2003a; Brandt et al. 2001b), as well as one QSO at $z = 4.45$ in the Lockman Hole (Schneider et al. 1998). As our target selection is based primarily on our R-band imaging, we are suffering from a bias against z>5 objects (the Ly_α emission is redshifted out of the FORS R-band at z∼5). Therefore, we may have a *few* QSOs at redshifts larger than 5 in the sample, but we can be certain that the number of these is on the order of a few. Most of the X-ray survey area is covered by near-infrared, where objects well beyond redshift of 15 are detectable. Among the objects covered in the near-IR, we only find 10 that are detected *only* in the near-IR. Furthermore, 4 of these were still observed spectroscopically, where we can detect Ly_α emission up to a redshift of 6.5. So in the unlikely case that *all* these objects and five additional objects not detected in optical imaging and without near-IR coverage are all very high redshift QSOs, we are still an order of magnitude below the predicted number of such objects. This suggests a turn-off of the X-ray selected QSO space density beyond $z \sim 4$ (Hasinger 2002; Barger et al. 2003a).

13. OPTICAL AND X-RAY DIAGNOSTICS

13.1. *X-ray and Optical Fluxes*

The soft and hard X-ray fluxes versus redshift diagrams are shown in Figure 16. The X-ray type-1 and type-2 populations have similar hard X-ray fluxes, whereas these two populations cover different ranges of soft X-ray fluxes, as can also be seen in Figure 1. However, the brighter, rarer objects, f_{X}(0.5-2 keV) and f_{X}(2-10 keV) larger than (1 and 5)$\times10^{-14}$ erg cm^{-2} s^{-1} respectively, are dominated by optically broad-emission line QSOs (at $z < 2$) as already demonstrated by larger samples of luminous X-ray sources detected by ROSAT, Chandra and XMM-Newton (Lehmann et al. 2001; Barger et al. 2002; Mainieri et al. 2002).

The observed R and K magnitudes of the extragalactic sources versus redshift are shown in Figures 17 and 18 respectively. At $z \gtrsim 2$, there are seven X-ray type-2 QSOs (XID 27, 54, 57, 62, 112, 202, 263) plus one lower X-ray luminosity type-2 AGN (XID 642); except the BAL QSO, all have narrow Lyα and C IV emission, $HR > -0.2$, and faint optical magnitudes R $\gtrsim$ 24.0. There are also six X-ray type-1 QSOs at $z \gtrsim 2$ (XID 11, 15, 21, 24, 68, 117), all but one being otically bright (R < 24) BLAGN, and five fainter, lower X-ray luminosity type-1 AGN (XID 87, 89, 230, 563, 901). The fraction of high-redshift, X-ray

type-2 QSO+AGN sources is thus 42%. Moreover, two of the X-ray type-1 QSO/AGN (XID 117, 901), with narrow Lyα and C IV emission but $HR < -0.2$, could be absorbed X-ray sources since the hardness ratio is not a good tracer of intrinsic absorption for high redshift sources. These results differ from those obtained for the CDFN 2 Msec sample (Barger et al. 2003b) which comprises 26 objects at $z \gtrsim 2.0$ (excluding the sources with tentative redshifts or complex/multiple structure or possible contamination: their Types s and m, respectively) of which 20 are BLAGN, thus an optical type-2 QSO+AGN fraction of 23%. This may arise from an observational selection as 10 (53%) of the 19 CDFS sources at $z \gtrsim 2$, with secure redshift identification, have R > 24 as compared to only 2 (8%) out of 26 CDFN sources.

The segregation between the X-ray type-1 and type-2 QSOs/AGNs seen in the R versus z diagram (Figure 17) is far less pronounced in the K versus z diagram (Figure 18). This is most likely due to the presence of dust in X-ray type-2 QSOs/AGNs associated with the X-ray absorbing material which severely obscures the nuclear component, as well as an increased contribution of the galaxy host light in the K-band relative to that of the AGN. The X-ray and optical versus redshift diagrams (Figure 16, 17 and 18) strongly suggest that the X-ray type-1 and type-2 populations cover roughly the same range of intrinsic luminosities (see also Rosati et al. 2002; Mainieri et al. 2002).

13.2. *X-ray and Optical Colours*

A segregation of the X-ray type-1 and type-2 populations is also present in the R−K versus z diagram (see Figure 19), as first outlined by Lehmann et al. (2001) and confirmed by Mainieri et al. (2002). The deeper Chandra observations reveal many more X-ray type-2 sources which have optical/near IR colours dominated by the host galaxy and most of them cluster around the SED tracks of elliptical and Sbc galaxies at $0.5 < z < 1.0$ (see also Rosati et al. 2002). The X-ray type-1 population usually follows the evolutionary track of an unreddened QSO, except nine AGNs/QSOs at $z \gtrsim 1$, all with R−K $\gtrsim 4$. This may be due to either an important contribution of the galaxy host light in the near IR or obscuration by dust. Among these nine X-ray type-1 sources, the X-ray luminous, red BLAGN at $z = 1.616$ (XID 67) was observed with HST/WFPC2 and is clearly resolved with an elliptical morphology (Koekemoer et al. 2002). A substantial contribution of the host galaxy could also account for the red colour of two BLAGN at $z \simeq 1.62$ (XID 46, 101). Obscuration by dust associated with the X-ray aborbing material is more probable for the remaining six X-ray type-1 sources, of which four belong to the HEX optical class and are at $1.6 \lesssim z \lesssim 2.6$ (XID 31, 117, 563, 901) and two belong to the LEX optical class and are at $z \simeq 1.0$ (XID 18, 242).

For a large fraction of the X-ray sources, there is a relationship between the hardness ratio, HR, and the R−K colour as shown in Figure 20. The bluer objects are X-ray type-1 QSOs, whereas the redder ones are mostly X-ray type-2 AGNs at $z \sim 0.5$ to 1.0. However, the redder objects (R−K > 4) cover a wide range of HR values, as already noted by Franceschini et al. (2002), and they comprise many X-ray type-1 AGNs, including the nine objects discussed above, while most of the remaining X-ray type-1 are $z < 1$ objects of the optical LEX class. To constrain the nature of the redder, X-ray type-1 AGNs requires to conduct an X-ray spectral analysis (Chandra and XMM-Newton data) of these sources (Streblyanskaya, Mainieri et al. in preparation), primarily those with secure redshifts, and to derive the morphological properties of their host galaxies using the HST observations from the GOODS-ACS Treasury program.

13.3. *X-ray Selected Extremely Red Objects*

The fraction of extremely red objects (EROs: R−K > 5.0) among X-ray sources appears to increase with decreasing optical flux as found for a subset of the CDFN X-ray sources (Alexander et al. 2001) and for Lockman Hole (LH) sources detected by XMM-Newton (Mainieri et al. 2002). We use the CDFS sample given in Table 5 to confirm this trend. There are 151 X-ray sources with bright, R<24, counterparts observed in the R and K bands. Five sources were not detected in the K band (K > 20.3), but the upper limits on their R−K colours are smaller than 5. The fraction of EROs in this bright optical sample is 10% (15 objects). The fainter optical sample is limited to $24 \leq R < 26$ to have meaningful R−K upper limits and it comprises 72 X-ray sources. Most of these faint objects do not have spectroscopic redshifts. Thus, in cases of several possible counterparts, the brigthest of the best centred counterparts was selected. To the 14 EROs with measured R−K colours, should be added the four objects detected in the K band only (R > 26.3), thus with R−K $\gtrsim$ 6.0. For the X-ray counterparts not detected in the K band, all those with $24 \leq R < 25$ have R−K upper limits smaller than 5, but among the 10 objects with $25 \leq R < 26$ only four have R−K $\lesssim$5.0. The remaining six objects have R−K upper limits in the range 5.3 to 5.6, but we will consider them as non-EROs in order to get a conservative value of the number of EROs among the fainter optical sample. The ERO fraction in the R≥24 sample is thus 25%, or 2.5 times higher than for the R<24 sample.

Six of the optically bright CDFS EROs have redshift estimates (5 secure), all with $z \sim 1$ (± 0.3). One is an X-ray AGN-1 (LEX optical class), and five are X-ray AGN-2 (LEX or ABS class) thus with strong optical obscuration associated with X-ray absorption. The other nine objects do not show any optical emission/absorption feature and all, but one, have

$HR < -0.2$. If they were at $z \sim 1$, they would have luminosities $L_{\rm X}$(0.5-10 keV)$> 10^{42}$ erg s^{-1}. The fraction of hard X-ray sources among the optically bright ERO population is thus 40%. Higher redshift sources are present in the optically faint ERO sample. Among the six objects with redshift estimates (4 secure), five are at $1.6 \lesssim z \lesssim 3.7$ of which three are X-ray luminous QSOs. The fraction of hard X-ray, optically faint EROs is 50%, but if there were a majority of high z sources, the bulk of this faint ERO population would be heavily absorbed X-ray sources. A similar result was found for the LH sources (Mainieri et al. 2002). This sample comprises 66 objects with measured R−K colour (only 20 are fainter than R=24), of which 18 are EROs. Five EROs (28%) are not detected in the hard band as compared to 27% and 22% for the CDFS optically bright and faint ERO samples, respectively. The X-ray spectral analysis of the LH sources shows that all, but one, of the $HR > -1.0$ sources have high intrinsic absorption: ten have absorbing column densities $N_{\rm H} > 10^{22}$ cm^{-2} and two, without redshift identification, have lower limits (observer frame) of $N_{\rm H,min} > 10^{21.5}$ cm^{-2}.

Among the X-ray selected EROs, the dominant population appears to be fairly luminous, absorbed X-ray sources, thus of the X-ray type-2 AGN class, at intermediate and high redshifts. This is consistent with the small fraction (1.5-10%) of near-IR selected EROs detected in X-ray (Cimatti et al. 2003). EROs belonging to other classes, elliptical galaxies or dusty starbursts (Stevens et al. 2003), are also most probably present. Indeed, among the optically faint EROs, there are a few sources with optically red and soft X-ray spectra (e.g. XID 579b).

Objects of different classes are also found for EROs in the HDFN and the Lockman hole (Franceschini et al. 2002; Stevens et al. 2003): sources at $z \sim 1$ with SEDs typical of elliptical galaxies, dusty starbursts and $z > 1.5$ absorbed AGN.

13.4. *Luminosities*

A trend of increasing hard X-ray luminosity (2-10 keV band) with absolute K magnitude can be seen in Figure 21. This trend is not present when the X-ray luminosity in the broad 0.5-10 keV band is considered instead (see also Franceschini et al. 2002). We also show in this figure the effect expected from the correlation found between the bulge luminosity and the black hole mass (Marconi & Hunt 2003). We used very uncertain assumptions to derive this curve. We assumed that around 40% of the K-band emission originates in the bulge and we assumed that the X-ray luminosity is 0.1% of the Eddington limit luminosity. The observed X-ray luminosity in the hard band is close to the intrinsic one (small K correction for most of the sources) and the reddening correction for the K absolute magnitude is much smaller in the near-IR than in the optical, although it could still be important for the

extremely red objects. We thus expect a tighter correlation between the mid-IR luminosity, to be obtained by the Spitzer-GOODS Legacy program, and the hard X-ray luminosity. The trend present in Figure 21 reinforces the suggestion made above that the X-ray type-1 and type-2 populations cover the same range of luminosities, thus trace similar levels of gravitational accretion. They differ by either the environment close to the AGN and/or the viewing angle to the nucleus, the contribution of the light from an early-type host galaxy, or the dust content and dust-to-gas ratio within the host galaxy, or an associated starburst.

The observed hard X-ray luminosity as a function of redshift is shown in Figure 22. There are X-ray luminous X-ray type-1 QSOs down to $z = 0.5$, thus no strong evolution, confirming the findings in the CDFN (Barger et al. 2002). However, this only applies to the X-ray type-1 population, as there is only one (8%) X-ray type-2 QSO (XID 51) out of 13 QSOs at $0.5 < z < 2$. Two of the X-ray type-1 QSOs show narrow emission lines only (XID 18, 31) and could be absorbed X-ray sources, as indeed confirmed by X-ray spectral analysis of XID 31 ($z = 1.603$) which is an absorbed source with $N_{\rm H} = 1.4 \times 10^{22}$ cm^{-2} (V. Mainieri, private communication). Even including these narrow-line QSOs in the type-2 sample would still lead to only 23% X-ray type-2 QSOs at lower redshift compared to 54% at $z > 2$ (see Section 13.1). This difference (detected at 90% confidence level) would no longer be as significant if sources down to $L_{\rm X}$(2-10 keV) $> 10^{43.5}$ erg s^{-1} were considered instead. Indeed, the ratio of X-ray type-2/type-1 sources at $0.5 < z < 2$ increases with decreasing hard X-ray luminosity, the type-2 population being dominant for $L_{\rm X}$(2-10 keV) $< 10^{43.0}$ erg s^{-1}. This trend is confirmed by the analysis of the 2-10 keV luminosity function derived from ASCA, HEAO1 and Chandra surveys (Ueda et al. 2003) which shows that, at $z < 1$, the percentage of X-ray type-2 AGN ($N_{\rm H} > 10^{22}$ cm^{-2}) decreases with increasing intrinsic luminosity from 49% at $L_{\rm X}$(2-10 keV) $= 10^{43}$ erg s^{-1} to 26% at $L_{\rm X}$(2-10 keV) $= 10^{45}$ erg s^{-1}.

The X-ray spectral analysis (absorbing column densities and intrinsic X-ray luminosities) of the QSOs+AGNs of the CDFS and CDFN spectroscopic samples will enable the determination of the cosmic evolution of the X-ray type-1 and the X-ray type-2/absorbed sources, thus of a possible differential cosmic evolution between these two populations. It should be noted that Barger et al. (2002) mention the existence of only two type-2 QSOs at $0.5 < z < 2$ (both at $z \approx 1$) while, in their Table 1, there are 12 broad-line QSO+AGN sources in the same redshift range, which is consistent with our results. However, in the CDFN, the fraction of type-2 QSOs is small at both intermediate and high (see Section 13.1) redshifts.

14. SUMMARY AND OUTLOOK

We presented a catalog of 137 secure and 24 tentative spectroscopic identifications of the 349 X-ray objects (including 3 new, faint sources) in the CDFS field, based on our survey using the VLT. Our spectroscopic survey is 40% complete considering the whole X-ray catalog, and 70% complete if we consider the subset in the central $8'$ radius with optical counterparts at R<24. This can compared to the somewhat higher spectroscopic completeness achieved in the Chandra Deep Field North identification programme (Barger et al. 2002), where the corresponding fractions are 49% and 78%, respectively. Very recently, optical identifications have also been presented for the 2 Msec observation of the HDFN (Barger et al. 2003b), which reach a completeness as high as 87% at R<24. At fainter optical magnitudes (R>24), however, the fraction of reliable spectroscopic identifications is larger for the CDFS compared to the HDFN. This is becoming important in particular, when comparing the fraction of X-ray type-2 QSOs at these faint magnitudes (see below).

We proposed a new, objective and simple scheme, based on X-ray luminosity and hardness ratio, to classify objects into X-ray type-1 (unabsorbed) and X-ray type-2 (absorbed) AGN. Hard ($HR > -0.2$) sources are classified as X-ray type-2 AGN or QSO, depending on their X-ray luminosity. Soft sources ($HR \leq -0.2$) are classified as X-ray galaxies, X-ray type-1 AGN or QSO, depending on their X-ray luminosity. At high optical and X-ray luminosities, this classification scheme is largely coincident with the classical AGN classification purely based on optical spectroscopic diagnostics. However, as soon as the integrated light of the host galaxy becomes larger than the optical emission of the AGN nucleus, the optical classification breaks down. Consequently, we are classifying many more objects as AGN, than would be selected in optical samples. An additional advantage of our proposed classification scheme is that it only relies on X-ray fluxes and redshift (to calculate L_X). So far we only used optical spectroscopy to derive the redshift, but our scheme can use photometric redshift techniques, thus going significantly beyond the capabilities of optical spectroscopy. Indeed, using photo-z techniques, more than 95% of the CDFS sources can be identified in our scheme (Mainieri, private communication).

We have spectroscopically identified a sample of 8 secure and 2 tentative high-luminosity X-ray sources with significant absorption, our X-ray type-2 QSO class. Nine ($^{+4.1}_{-3.0}$: 1σ errors) of these sources are in the redshift range $2 < z < 4$ and their optical spectra are dominated by strong, narrow high excitation UV permitted lines, very similar to the prototypical object CDFS-202 (Norman et al. 2002). In contrast, the spectroscopic sample existing in the HDFN so far (Barger et al. 2002) only contains 2 ($^{+2.6}_{-1.3}$) similar objects (HDFN #184 and #287). This difference may be due to the fact that our spectroscopy is pushing about one magnitude deeper than the HDFN spectroscopy in a part of the field. However, we can not exclude

true cosmic field-to-field variations in the number of X-ray type-2 QSOs. The fraction of X-ray type-2 to the total AGN population shows a significant variation with observed X-ray luminosity, consistent with, but even somewhat stronger than the trend found from ASCA surveys in the 2-10 keV band (Ueda et al. 2003): the X-ray type-2 fraction decreases from $75 \pm 8\%$ (8 type-1 vs. 24 type-2 AGN) in the luminosity range 10^{42-43} erg s^{-1}, over $44 \pm 8\%$ (20 vs. 16 AGN) at luminosities 10^{43-44} erg s^{-1}, to $33 \pm 10\%$ (16 vs. 8) at 10^{44-45} erg s^{-1} (see also Figure 13). This behaviour can probably explain some of the evolutionary trends apparent in Figures 16 and 22.

We found spectroscopic evidence for two large-scale structures in the field, predominantly populated by X-ray type-2 AGN but also X-ray type-1 AGN and normal galaxies: one at $z = 0.734$ has a fairly narrow redshift distribution and comprises two clusters/groups of galaxies centered on extended X-ray sources. The redshift distribution of the second one at $z = 0.674$ is broader (velocity space) and traces a sheet-like structure. A detailed comparison with the redshift spikes in a NIR-selected (K20) sample of galaxies in the same field has been performed by (Gilli et al. 2003). Similar, but much less pronounced redshift spikes have also been observed in the HDFN at redshifts around $z = 0.843$ and $z = 1.018$ by (Barger et al. 2002). AGN therefore trace large-scale structures as do normal galaxies. Further studies on larger samples are required to investigate, whether AGN are more strongly clustered than normal galaxies (Gilli et al. 2003) and, whether X-ray type-2 AGN are indeed clustering stronger than X-ray type-1 AGN, as indicated by the CDFS results.

However, the objects in these spikes do not dominate the sample. The observed AGN redshift distribution peaks at $z \sim 0.7$, even if the objects in the spikes and also the normal, starforming galaxies are removed. Compared to the pre-Chandra and XMM-Newton predictions of population synthesis models of the X-ray background (Gilli et al. 2003), there is an excess of $z < 1$ AGN, even taking into account the spectroscopic incompleteness of the sample. These models will therefore have to be modified to incorporate different luminosity functions and evolutionary scenarios for intermediate-redshift, lower-luminosity AGNs.

It will be interesting to study the correlation of active galaxies to field galaxies in the sheets and investigate the role that galaxy mergers play in the triggering of the AGN activity. Finally, there may be a relation between the surprisingly low redshift of the bulk of the Chandra sources, the existence of the sheets at the same redshift and the strongly evolving population of dusty starburst galaxies inferred from the ISO mid-infrared surveys (Franceschini et al. 2002).

The Chandra Deep Field South has been selected as one of the deep fields in the Spitzer legacy programme Great Observatories Origins Deep Survey (GOODS). GOODS will produce the deepest observations with the Spitzer IRAC instrument at 3.6-8μm and with the

MIPS instrument at 24μm over a significant fraction of the CDFS (see Fosbury et al. 2001). The same area has already been covered by an extensive set of pointings with the new Advanced Camera for Surveys (ACS) of the Hubble Space Telescope in BVIz to near HDF depth. Following up the deep EIS survey in the CDFS, ESO has undertaken a large program to image the GOODS area with the VLT to obtain deep JHKs images in some 32 ISAAC fields. A small spot inside the CDFS has also been selected as the location of the HST ACS ultradeep field (UDF), aiming at roughly two magnitudes fainter than the Hubble Deep Fields, over a substantially larger area. An even larger field than the CDFS has been surveyed with the HST ACS program GEMS and has also been covered by multiband optical photometry as part of the COMBO-17 survey (Wolf et al. 2003). The next step in the optical identification and classification work is to use the extremely deep HST ACS and VLT ISAAC (or EIS SOFI) data provided by GOODS and the narrow band photometry provided by COMBO-17 to obtain multicolour photometric redshifts for the objects not covered by and/or too faint for our spectroscopic identification programme (Zheng et al., in preparation).

Additional X-ray information in an area wider than the CDFS is existing from a deep XMM-Newton pointing of $\sim$400 ksec exposure time (PI: Bergeron). The already existing Chandra Megasecond coverage will be widened and deepened with four additional 250 ksec ACIS-I pointings (PI: Brandt). The multiwavelength coverage of the field is complemented by deep 20 cm radio data from the VLA and ATCA. The CDFS will therefore ultimately be one of the patches in the sky providing a combination of the widest and deepest coverage at all wavelengths and thus a legacy for the future.

This publication makes use of data products from the Two Micron All Sky Survey, which is a joint project of the University of Massachusetts and the Infrared Processing and Analysis Center/California Institute of Technology, funded by the National Aeronautics and Space Administration and the National Science Foundation. Three of our redshifts have been obtained from the 2dFGRS public dataset.

REFERENCES

Alexander, D..M., Brandt, W..N., Hornschemeier, A..E., et al. 2001, AJ, 122, 2156

Alexander, D..M., Aussel, H., Bauer, F..E., et al. 2002, ApJ, 568, L85

Antonucci, R. R. J., & Miller, J. S., ApJ, 297, 621

Arnouts, S., Vandame, B., Benoist, C., et al. 2001, A&A, 379, 740

Barger, A. J., Cowie, L. L., Mushotzky, R. F., & Richards, E. A. 2001a, AJ, 121, 662

Barger, A. J., Cowie, L. L., Bautz M. W., et al. 2001b, AJ, 122, 2177

Barger, A. J., Cowie, L. L., Brandt, W. N., et al. 2002, AJ, 124, 1839

Barger, A. J., Cowie, L. L., Capak, P., et al. 2003, ApJ, 584, L61

Barger, A. J., Cowie, L. L., Capak, P., et al. 2003, AJ, 126, 632

Brandt, W. N., Hornschemeier, A. E., Alexander, D. M., et al. 2001, AJ, 122, 1

Brandt, W. N., Alexander, D. M., Hornschemeier A. E., et al. 2001a, AJ, 122, 2810

Brandt, W. N., Alexander, D. M., Bauer, F. E., & Hornschemeier, A. E. 2002, astro-ph/0202311

Cardelli, J. A., Clayton, G. C., & Mathis, J. S. 1989, ApJ, 345, 245

Carroll, S. M., Press, W. H., & Turner, E. L. 1992, ARA&A, 30, 499

Cimatti, A., Daddi E., Cassata, P., et al. 2003, A&A, in press, astro-ph/0310742

Cimatti, A., Mignoli, M., Daddi, E., et al. 2002, A&A, 392, 865

Cimatti, A., Pozzetti, L., Mignoli, M., et al. 2002, A&A, 391, L1

Coleman, G. D., Wu, C. C., & Weedman, D. W. 1980, ApJS, 43, 393

Colless, M., Dalton, G., Maddox, S., Sutherland, W., Norberg, P. et al. , 2001, MNRAS, 328, 1039

Comastri, A., Setti, G., Zamorani, G., & Hasinger, G. 1995, A&A, 296, 1

Croom, S. M., Warren, S. J., & Glazebrook, K. 2001, MNRAS, 328, 150

Daddi, E., Cimatti, A., Renzini, A., et al. 2003, ApJ, in press, astro-ph/0308456

Fabian A. C., Barcons X., Almaini O., & Iwasawa K. 1998, MNRAS, 297, L11

Fadda, D., Flores, H., Hasinger, G., et al. 2002, A&A, 383, 838

Fan, X., et al. 2001, AJ, 121, 54

Fiore, F., La Franca, F., Giommi, P., et al. 1999, MNRAS, 306, 55

Fiore, F., LaFranca, F., Vignali, C., et al. 2000, New Astronomy, 5, 143

Fosbury, R. A., Bergeron, J., Cesarsky, C., Cristiani, S., Hook, R., Renzini, A., & Rosati, P. 2001, The Messenger, 105, 40

Franceschini, A., Fadda, D., Cesarsky, C., et al. 2002, ApJ, 568, 470

Fukugita, M., Ichikawa T., Gunn, J. E., Doi, M., Shimasaku, K., & Schneider, D. P. 1996, AJ, 111, 1748

Gebhardt, K., Bender, R., Bower, G., et al. 2000, ApJ, 539, 13

Giacconi, R., Rosati, P., Tozzi, P., et al. 2001, ApJ, 551, 624

Giacconi, R., Zirm, A., Wang, J. X., Rosati, P., et al. 2002, ApJS, 139, 369

Gilli, R., Salvati, M., & Hasinger, G. 2001, A&A, 366, 407

Gilli, R., Cimatti, A., Daddi E., et al. 2003, ApJ, 592, 721

Granato, G. L., Danese, L., & Francheschini, A. 1997, ApJ, 486, 147

Gutierrez-Moreno, A., Heathcote, S., Moreno, H., & Hamuy, M. 1994, PASP, 106, 1184

Haiman, Z., & Loeb A. 1999, ApJ, 519, 479

Hamuy, M., Walker, A. R., Suntzeff, N. B., Gigoux, P., Heathcote, S. R., & Phillips, M. M. 1992, PASP, 104, 533

Hamuy, M., Suntzeff, N. B., Heathcote, S. R., Walker, A. R., Gigoux, P., & Phillips, M. M. 1994, PASP, 106, 566

Hasinger, G., Burg, R., Giacconi, R., et al. 1998, A&A, 329, 482

Hasinger, G., Altieri, B., Arnaud, M., et al. 2001, A&A, 365, 45

Hasinger, G. 2002, astro-ph/0202430

Ho, L. C, Filippenko, A. V., & Sargent, W. L. W. 1993, ApJ, 417, 63

Khachikian, E. Y., & Weedman, D. W. 1974, ApJ, 192, 581

Kinney, A. L., Bohlin, R. C., Calzetti, D., Panagia, N., & Wyse, R. F., G. 1993, ApJS, 86, 5

Hog, E., Kuzmin, A., Bastian, U., Fabricius, C., Kuimov, K., Lindegren, L., Makarov, V. V., & Roeser, S. 1998, A&A, 335, L65

Hornschemeier, A. E., Brandt, W. N., Garmire, G. P., et al. 2000, ApJ, 541, 49

Hughes, D. H., Serjeant, S., Dunlop, J., et al. 1998, Nature, 394, 241

Jones, L. R., Fong, R., Shanks, T., Ellis, R. S., & Peterson, B. A. 1991, MNRAS, 249, 481

Koekemoer, A. M., Grogin, N. A., Schreier, E. J., et al. 2002, ApJ, 567, 657

Landolt, A. U. 1992, AJ, 104, 340

Lehmann, I., Hasinger, G., Schmidt, M., et al. 2000, A&A, 354, 35

Lehmann, I., Hasinger, G., Schmidt, M., et al. 2001, A&A, 371, 833

Lehmann, I., Hasinger, G., Murray, S. S, & Schmidt M. 2002, astro-ph/0109172

Maccacaro, T., Gioia, I. M., Wolter, A., Zamorani, G., & Stocke, J. T. 1988, ApJ, 326, 680

Mainieri, V., Bergeron, J., Hasinger, G., et al. 2002, A&A, 393, 425

Makishima, K., Kubota, A., Mizuno, T., et al. 2000, ApJ, 535, 632

Marconi, A., & Hunt, L. K. 2003, ApJ, 589, L21

Metcalfe, N., Shanks, T., Campos, A., McCracken, H. J., & Fong, R. 2001, MNRAS, 323, 795

Miyaji, T., Hasinger, G., & Schmidt, M. 2000, A&A, 353, 25

Monet, D., Bird, A., Canzian, B., Dahn, C., et al. 1998, The USNO-A2.0 Catalogue, (U.S. Naval Observatory, Washington DC).

Moran, E. C., Filippenko, A. V., & Chornock, R. 2002, ApJ, 579, L71

Mushotzky, R. F., Cowie L. L., Barger, A. J., & Arnaud, K. A. 2000, Nature, 404, 459

Norman, C., Hasinger, G., Giacconi, R., et al. 2002, ApJ, 571, 218

Oke, J. B. 1990, AJ, 99, 1621

Osterbrock, D. E. 1989, Astrophysics of Gaseous Nebulae and Active Galactic Nuclei, University Science Books

Pen, U.-L. 1999, ApJS, 120, 49

Rosati, P., Tozzi, P., Giacconi, R., et al. 2002, ApJ, 566, 667

Schlegel, D., Finkbeiner, D., & Davis, M. 1998, ApJ, 500, 525.

Schmidt, M., Schneider, D. P., & Gunn J. E. 1997, AJ, 114, 36

Schmidt, M., Hasinger, G., Gunn, J. E., et al. 1998, A&A, 329, 495

Schneider, D. P., Schmidt, M., Hasinger, G., et al. 1998, AJ, 115, 1230

Seyfert, C. K. 1943, ApJ, 97, 28

Shaver, P. A., et al. 1996, Nature, 384, 439

Spergel, D. N., Verde, L., Peiris, H. V., Komatsu, E., et al. 2003, ApJS, 148, 175

Steidel, C. C., Adelberger, K. L., Giavalisco, M., Dickinson, M., & Pettini, M. 1999, ApJ, 519, 1

Stern, D., Moran, E. C., Coil, A. L., et al. 2002, ApJ, 568, 71

Stevens, J. A., Page, M. J., Ivison, R. J., et al. 2003, MNRAS, 343, L47

Stocke, J. T., Morris, S. L., Giola, I. M., et al. 1991, ApJS, 76, 813

Tozzi, P., Rosati, P., Nonino, M., et al. 2001, ApJ, 562, 42

Turnshek, D. A., Bohlin, R. C., Williamson, R. L., II, et al. 1990, AJ, 99, 1243

Ueda, Y., Akiyama, M., Ohta, K., & Miyaji, T. 2003, Astron. Nachr, 324, 36

Vandame, B., Olsen, L. F., Jorgensen, H. E. et al. 2001, astro-ph/0102300

Vignati, P., Molendi, S., Matt, G., et al. 1999, A&A, 349, L57

White, R. R. III, Sarazin, C. L., & Kulkarni, S. R. 2002, ApJ, 571, 23

Wolf, C., Meisenheimer, K., Rix, H.-W., et al. 2003, A&A, 401, 73

Zamorani, G., Mignoli, M., Hasinger, G., et al. 1999, A&A, 346,731

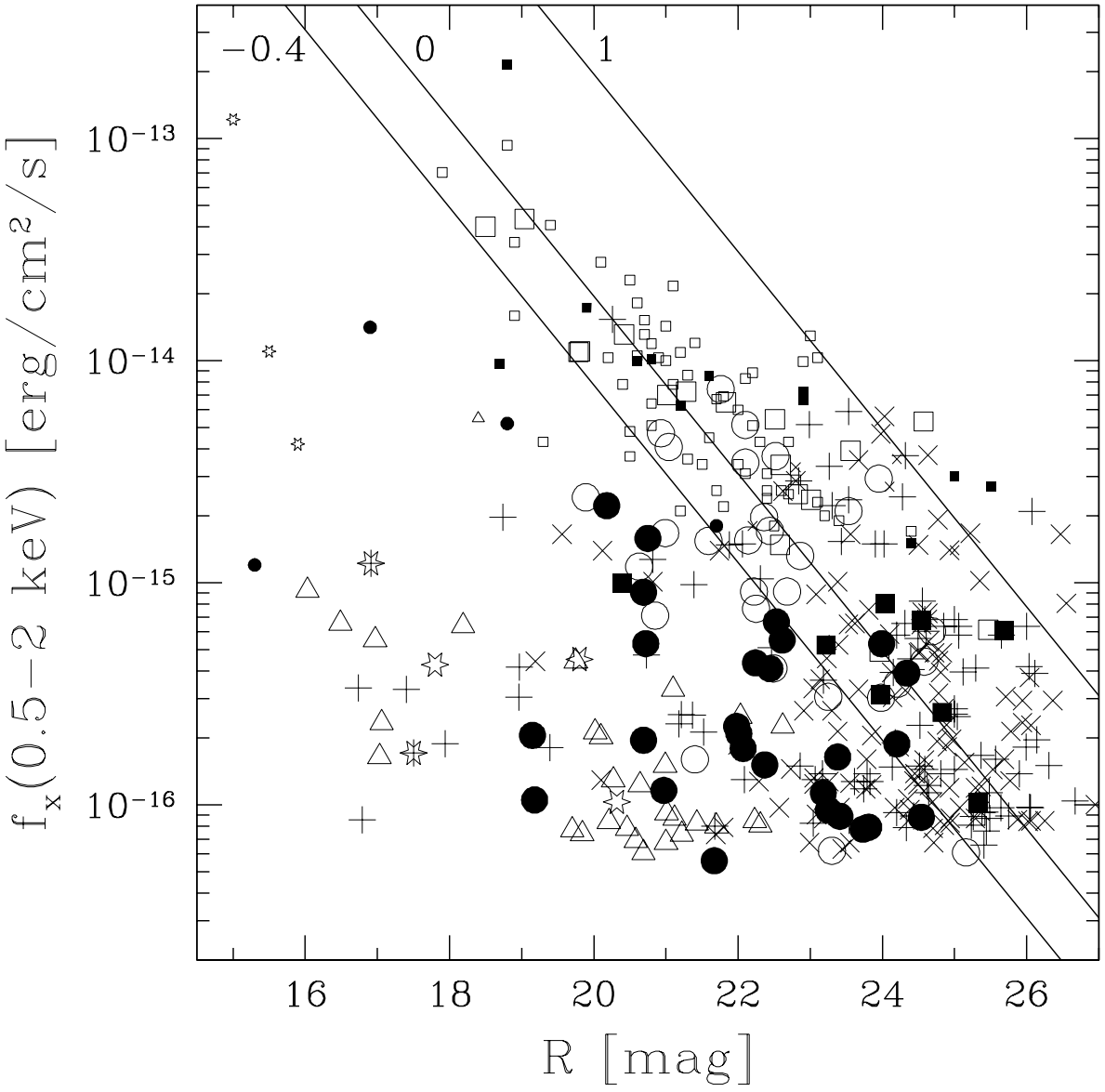

Fig. 1.— X-ray flux in the 0.5-2 keV band versus R-band magnitude for the CDFS-sources (larger symbols) and the ultradeep ROSAT survey in the Lockman Hole (smaller symbols). Objects are marked according to their X-ray classification for the CDFS sources and the original classification for the Lockman Hole sources: squares correspond to QSOs, circles to AGN and triangles to galaxies. Type-1 and type-2 AGNs/QSOs have empty and solid symbols, respectively. Stars are marked with star symbols. 'X' symbols refer to spectroscopically not securely identified CDFS counterpart candidates which we observed in our program, '+' symbols mark objects we did not observe. The solid lines correspond to an X-ray to optical flux ratio index (as discussed in Section 3) of 1, 0 and −0.4.

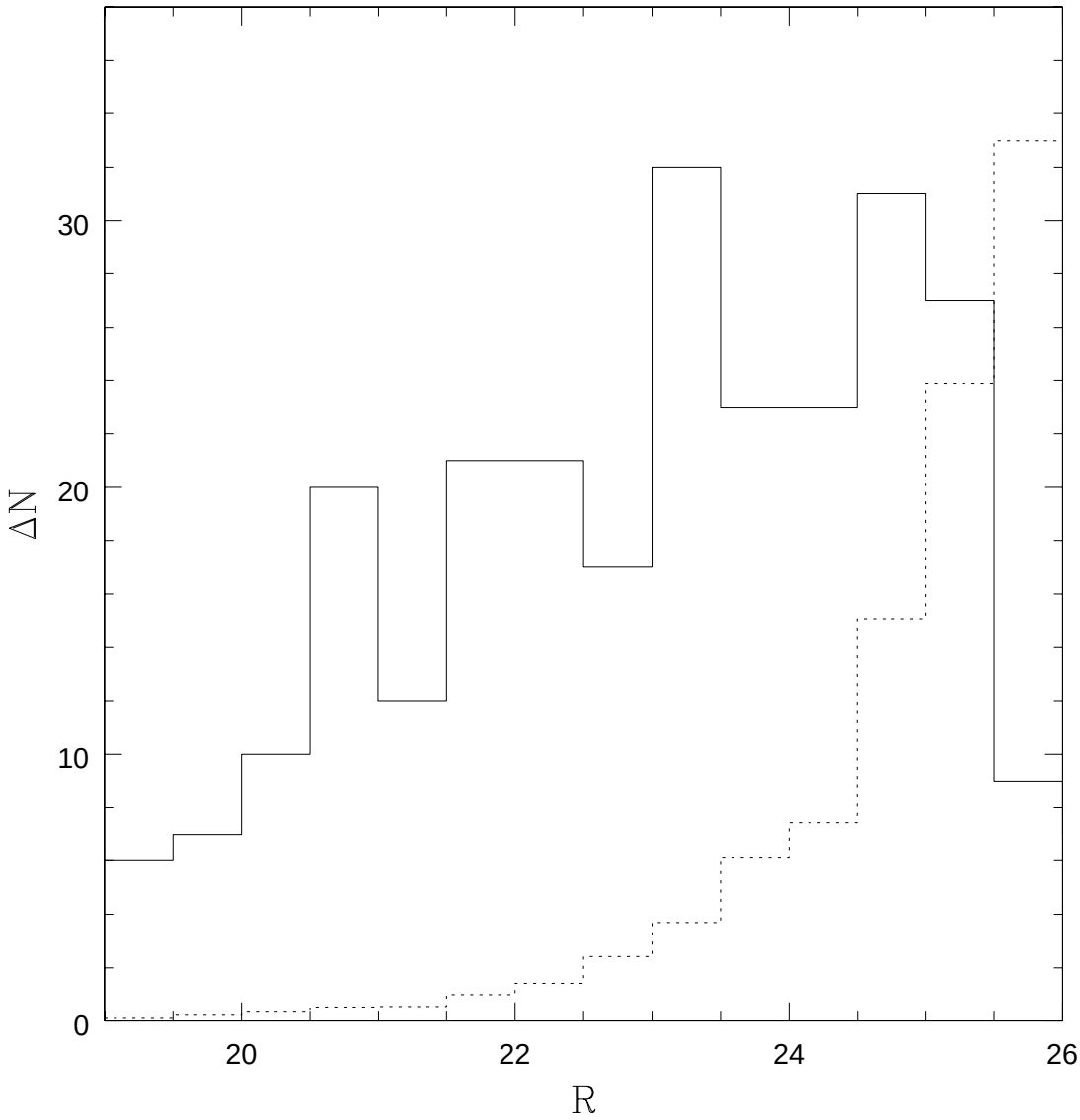

Fig. 2.— The R-band magnitude distribution of the selected (primary) optical counterparts of the X-ray sources in our survey (solid line). For comparision, we also show (dotted line) the expected distribution of random field galaxies normalized to the total area of the error circles of our X-ray sources, based on galaxy number count measurements (Metcalfe et al. 2001; Jones et al. 1991).

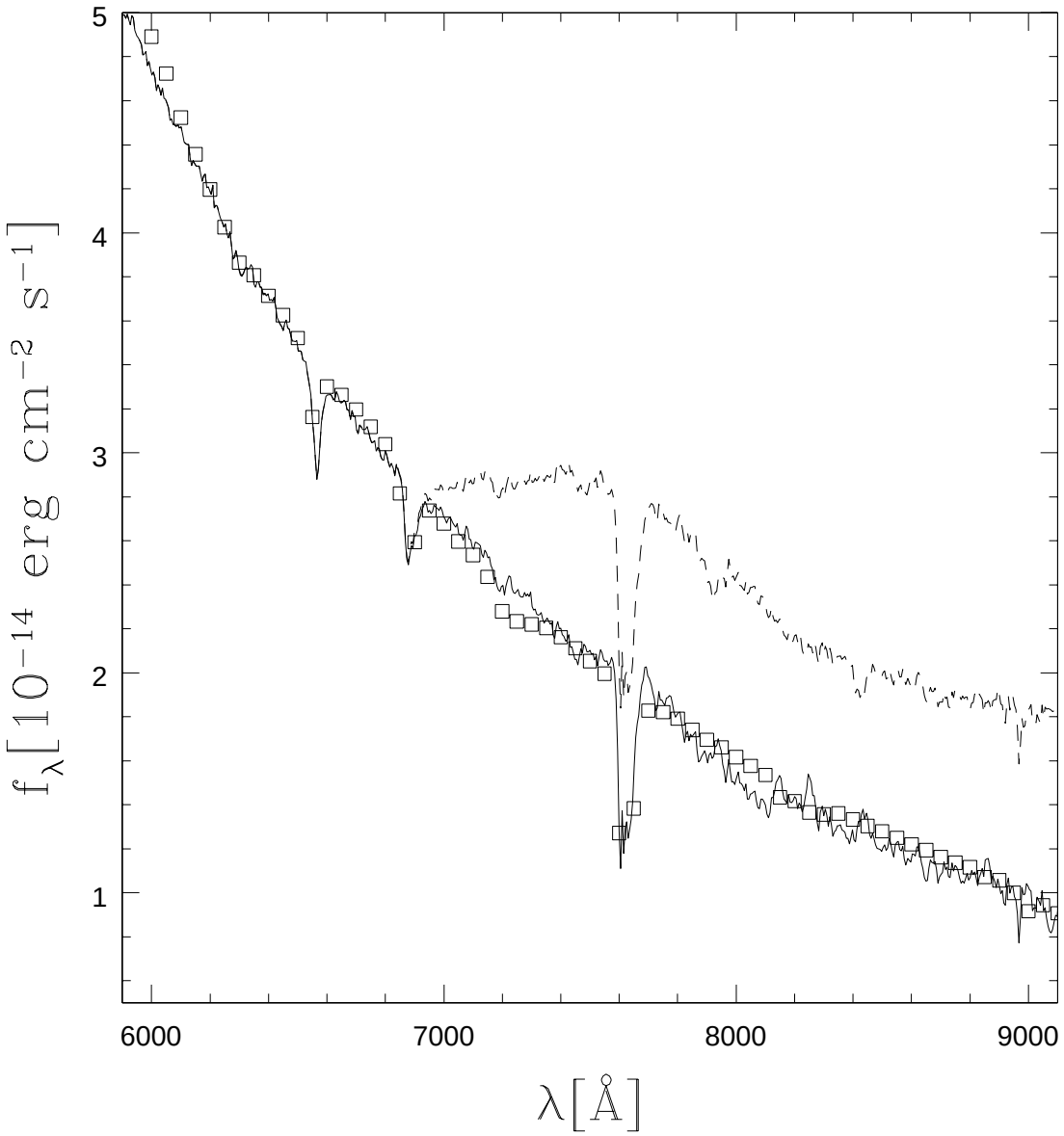

Fig. 3.— Flux calibrated spectra of a spectrophotometric standard star, Feige110 (Hamuy et al. 1992, 1994; Oke 1990). The dashed line is the measured flux without removing the second order contamination, solid line is the spectra *after* the correction. Empty squares are the real flux values from literature.

.

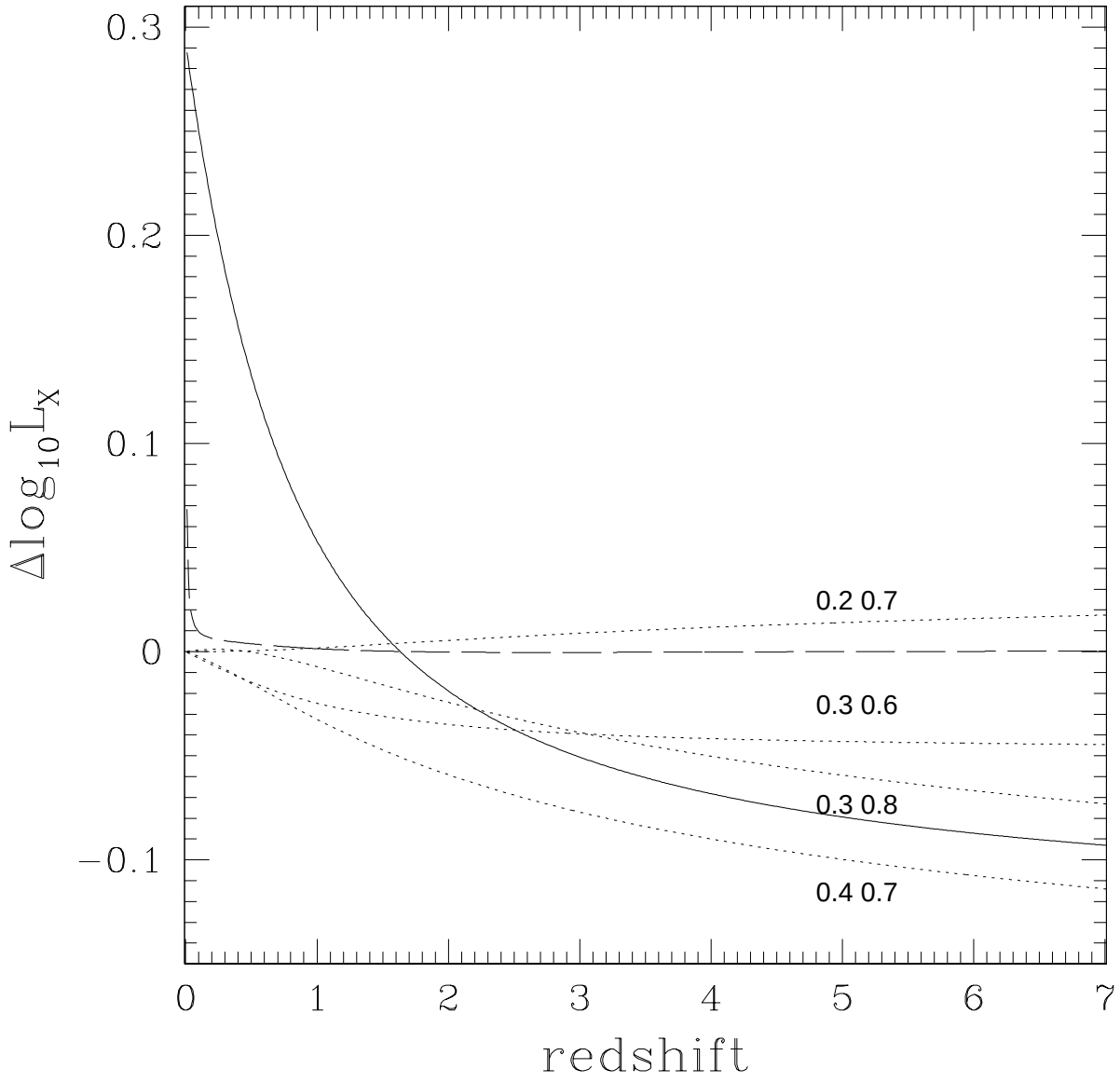

Fig. 4.— Comparing calculated L_X values in different cosmologies. Plotted are the changes as a function of redshift, compared to the current $\Omega_m = 0.3$, $\Omega_\Lambda = 0.7$, $H_0 = 70 km\ s^{-1}\ Mpc^{-1}$ cosmology. Dotted lines are slight variations on the two basic parameters, without changing the Hubble constant. The solid line is the now obsolete $\Omega_m = 1$, $\Omega_\Lambda = 0$, $H_0 = 50 km\ s^{-1}\ Mpc^{-1}$ cosmology. The result of an approximate formula (Pen 1999) for $\Omega_m = 0.3$, $\Omega_\Lambda = 0.7$, $H_0 = 70 km\ s^{-1}\ Mpc^{-1}$ is also shown (dashed line).

.

Fig. 5.— For these figures, see http://www.mpe.mpg.de/CDFS. Finding charts and VLT spectra of CDFS sources. Images are based on our FORS R-band imaging. The circles indicate the positional error (Giacconi et al. 2002). The images are $20'' \times 20''$ in size. If multiple optical counterparts were considered, they are marked on the finding charts. Next to the finding charts we show *all* spectroscopic observations available for the object. On the horizontal axis both the observed (bottom) and rest frame (top – if available) wavelength is shown in Å units. The vertical axis is the measured flux, f_λ in 10^{-18} erg cm^{-2} s^{-1} Å^{-1} units. Important emission (above the spectra) and absorption (below the spectra) features used for identification are also marked.

Fig. 6.— For this figure, see http://www.mpe.mpg.de/CDFS/. Extended object 138. The image covers 60×60 arcsec.

Fig. 7.— For this figure, see http://www.mpe.mpg.de/CDFS/. Extended object 249. The image covers 60×60 arcsec.

Fig. 8.— For this figure, see http://www.mpe.mpg.de/CDFS/. Extended object 560. The image covers 60×60 arcsec.

Fig. 9.— For this figure, see http://www.mpe.mpg.de/CDFS/. Extended object 566. The image covers 60×60 arcsec.

Fig. 10.— For this figure, see http://www.mpe.mpg.de/CDFS/. Extended object 594. The image covers 60×60 arcsec.

Fig. 11.— For this figure, see http://www.mpe.mpg.de/CDFS/. Extended object 645. The image covers 60×60 arcsec.

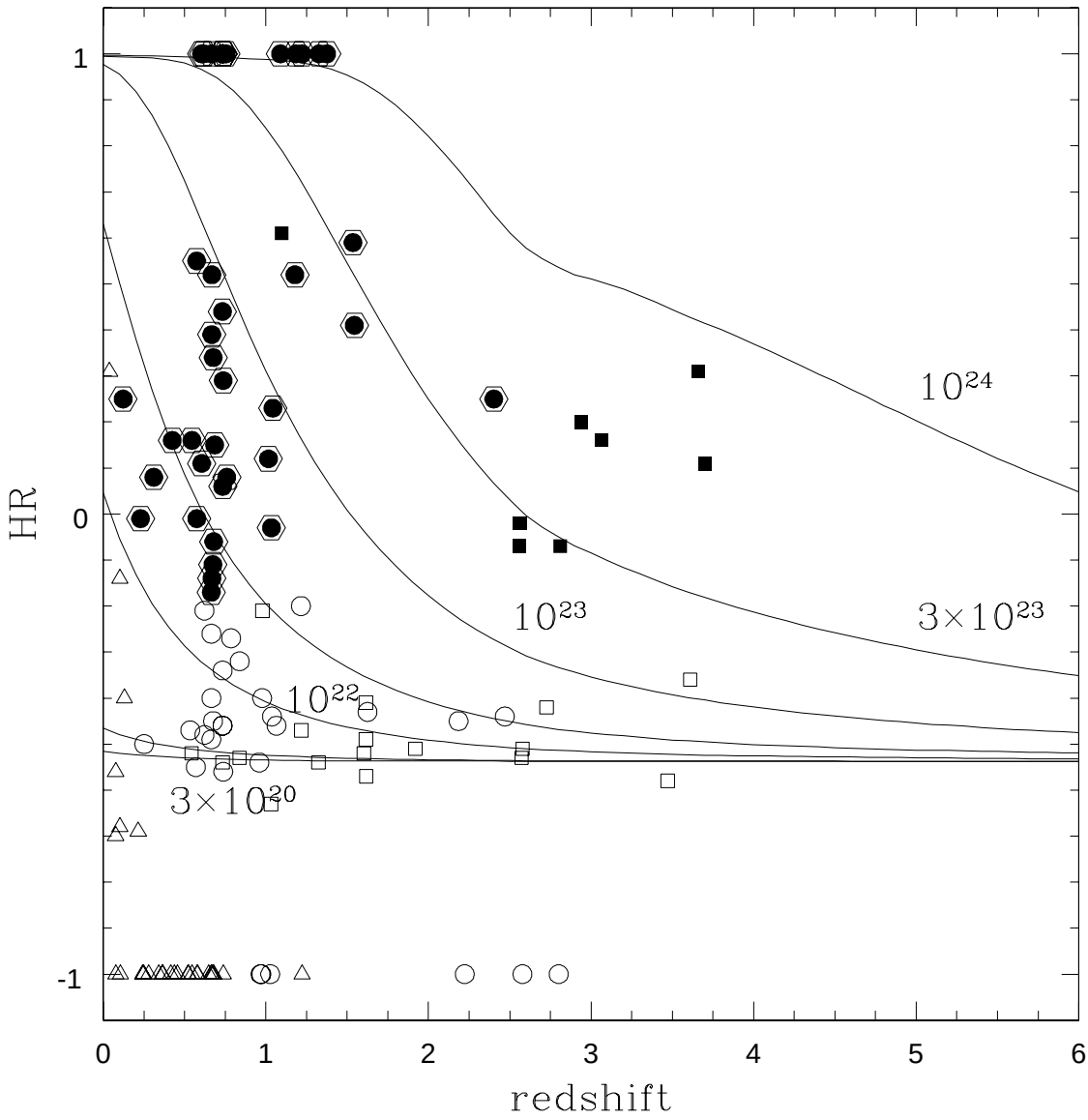

Fig. 12.— Hardness ratio versus redhsift, assuming a typical absorbed AGN spectrum with $\Gamma = 2$ and different absorptions, expressed as $\log(N_H)$. Identified CDFS objects are also plotted (see Figure 1 for symbols). HEX objects (likely optical type-2 AGNs) are additionaly marked with a hexagon.

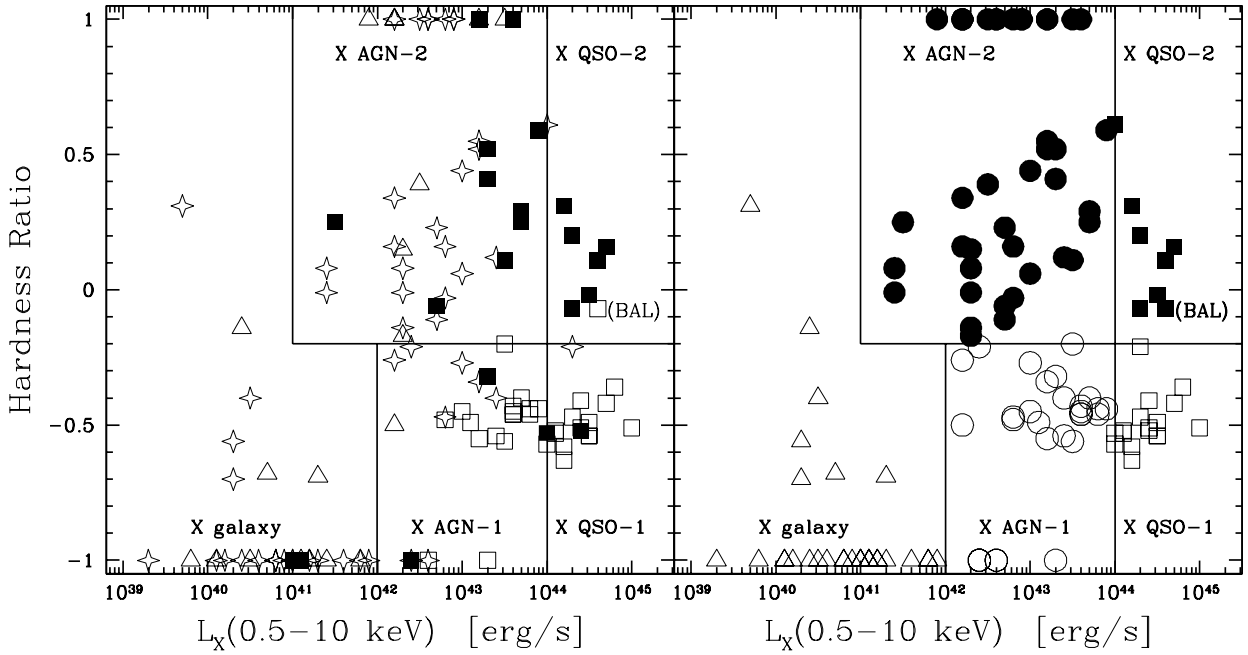

Fig. 13.— Hardness ratio versus observed X-ray luminosity in the 0.5-10 keV band. Symbols in the left panel show the classical optical classification (empty squares: BLAGN, filled squares: HEX, diamonds: LEX, triangles: ABS). Symbols in the right panel are as in see Figure 1 and follow the X-ray classification presented in Section 7. The BAL QSO (XID 62) is also marked.

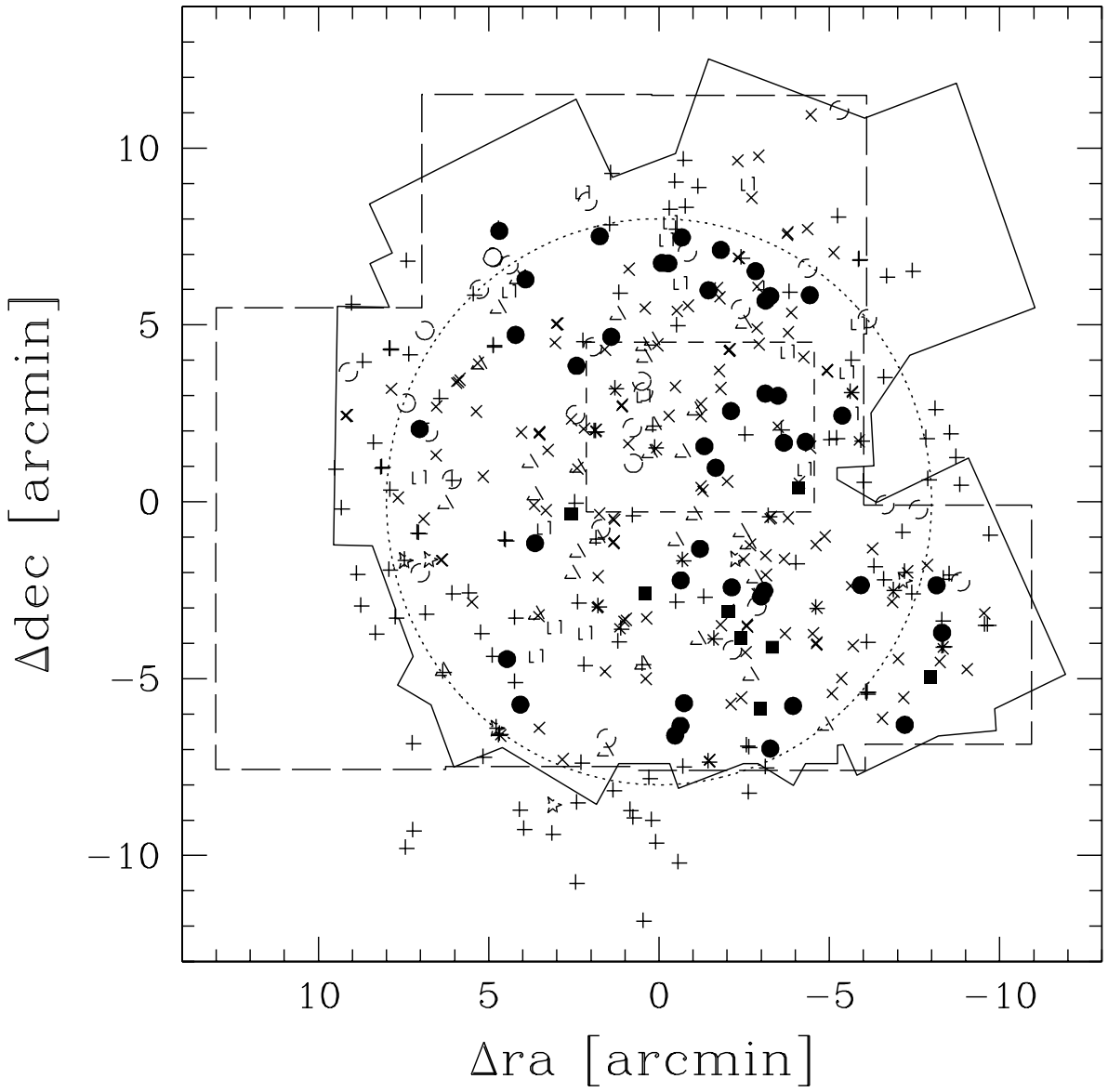

Fig. 14.— Spatial distribution of the X-ray sources with and without pectroscopic observations. Object classes are marked as in Figure 1. The area covered by our spectroscopic masks (solid line), the imaging survey (long dashed line), the K20 survey area (short dashed line) and an 8 arcmin radius circle, centered on the nominal CDFS pointing (3:32:28.0 -27:48:30 J2000; dotted line) is also shown.

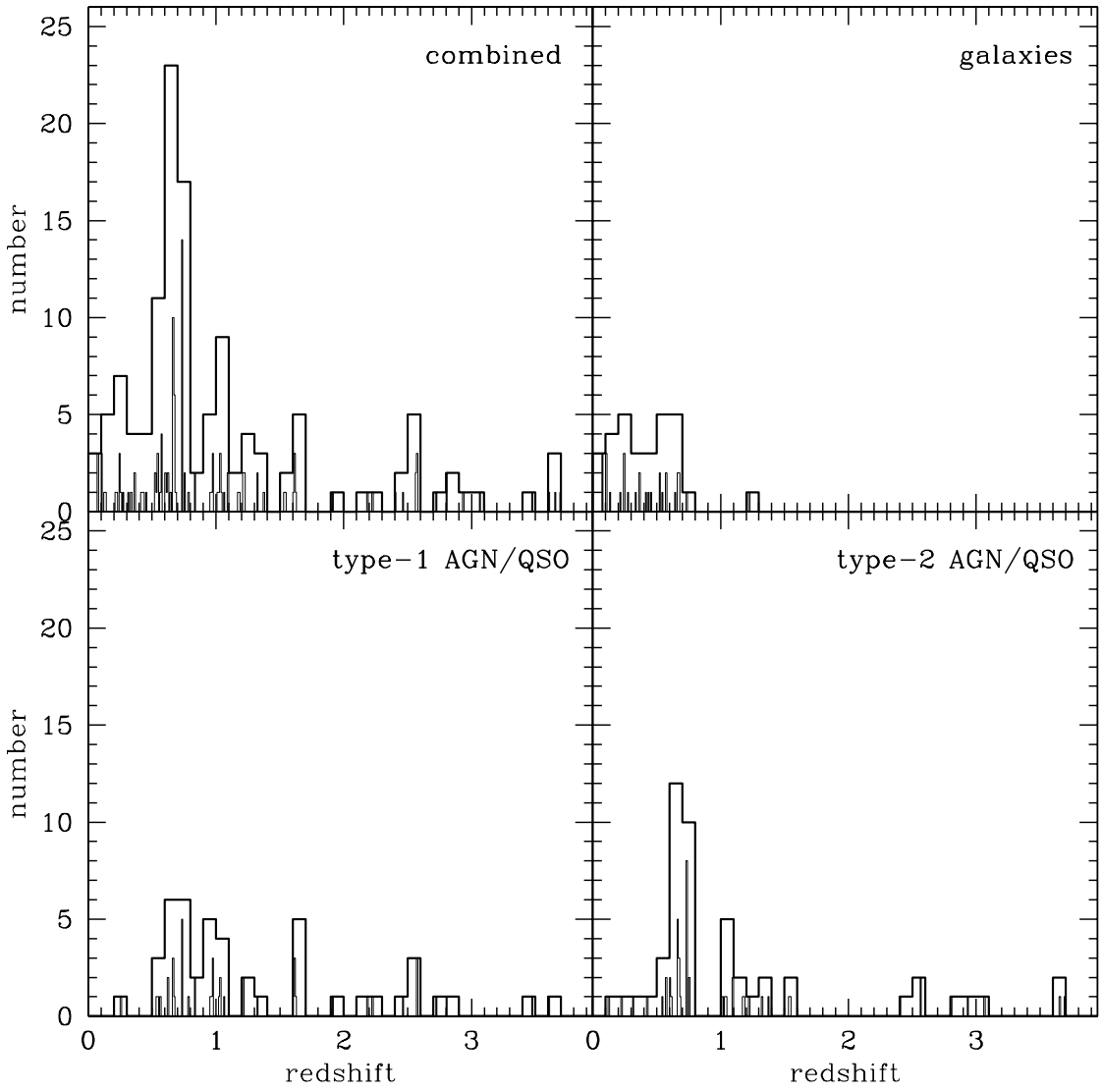

Fig. 15.— Redshift distribution of the various classes of X-ray sources as well as their cumulative distribution. Object XID 138a and 138b are counted as two separate objects. The 4 extended objects (249, 566, 594 and 645) are not included. Two bin sizes ($\Delta z = 0.01$ and 0.1) are selected to show the excess of objects around $z = 0.674$ and 0.734.

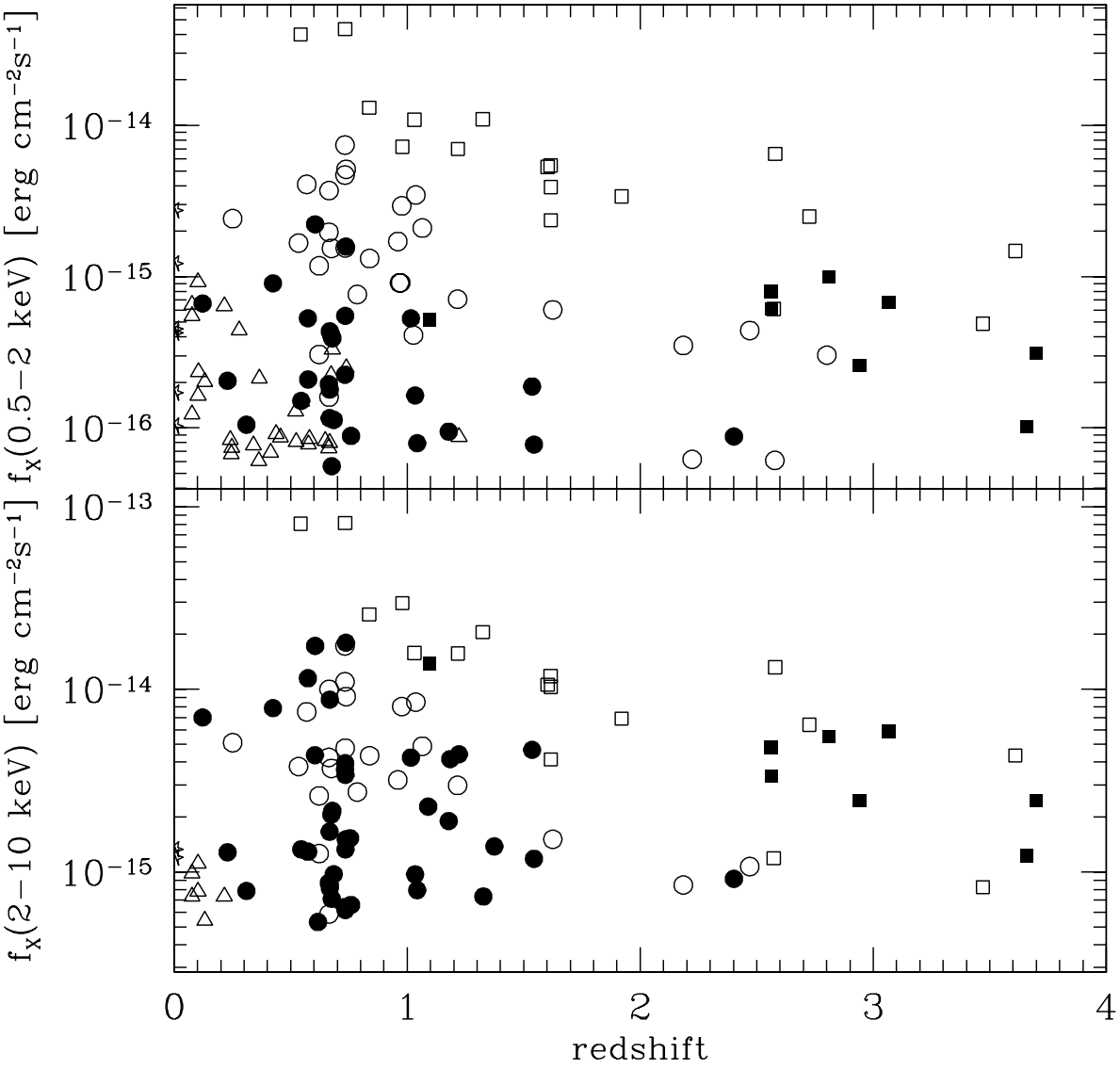

Fig. 16.— X-ray flux of the CDFS sources as a function of redshift for the 0.5-2 keV band (top) and 2-10 keV band (bottom). Symbols are as in Figure 1.

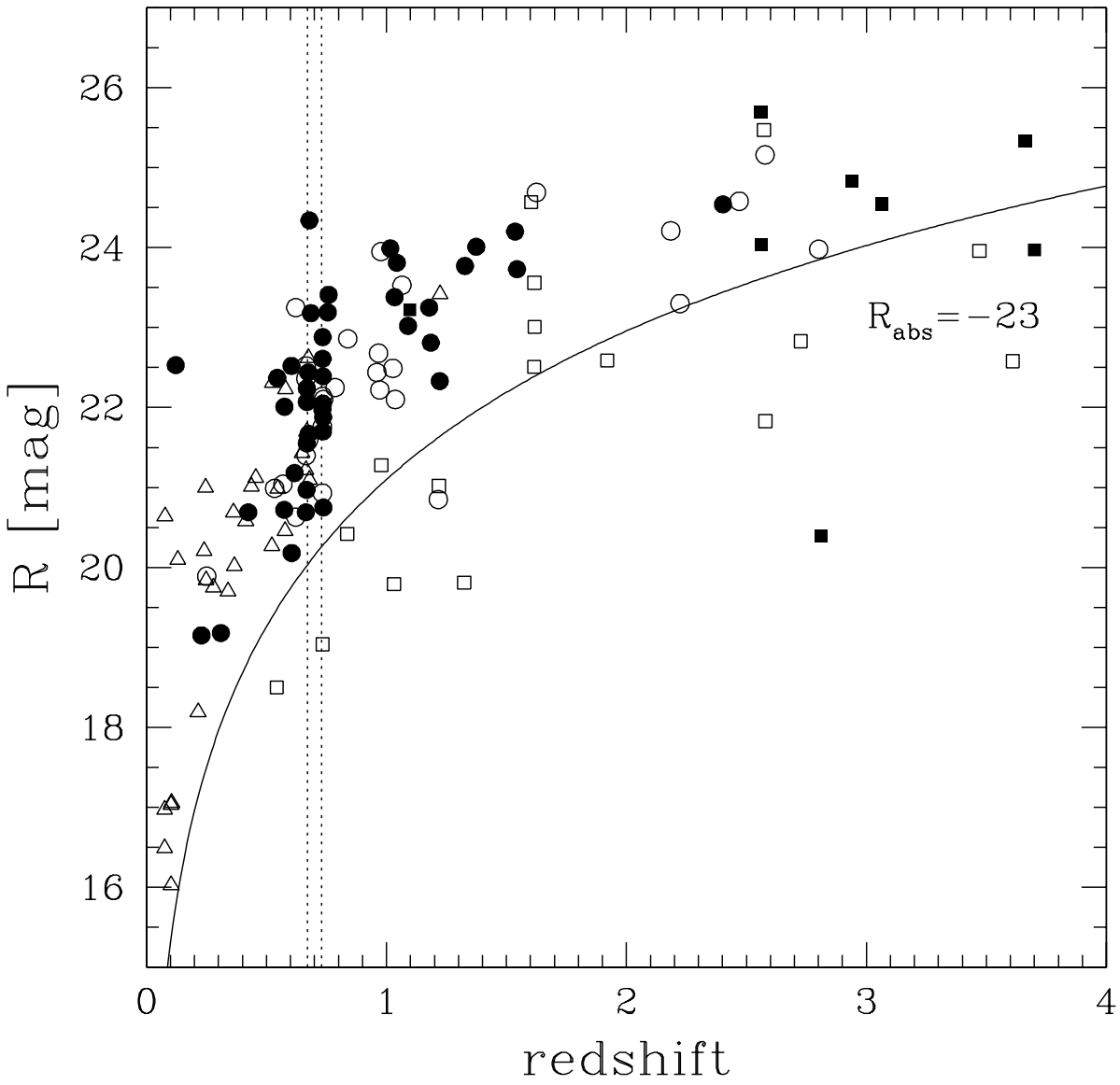

Fig. 17.— R magnitude as a function of redshift for the CDFS X-ray sources. Symbols are as in Figure 1. The dotted lines indicate the two structures around $z = 0.67$ and 0.73. The solid line corresponds to an absolute magnitude of $M_{\rm R} = -23$.

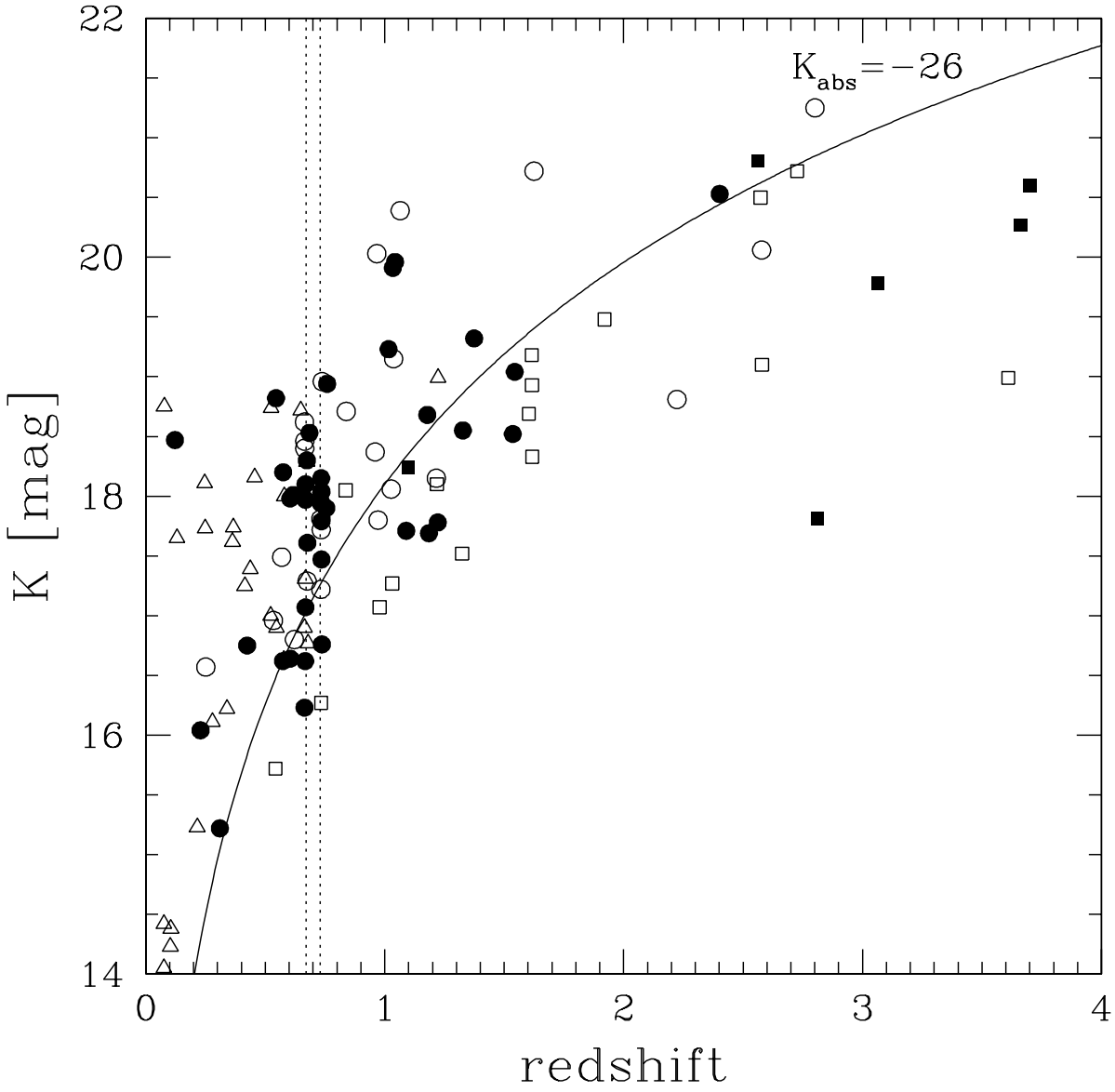

Fig. 18.— K magnitude as a function of redshift. Symbols are as in Figure 1. The solid line corresponds to an absolute magnitude of $M_{\rm K} = -26$. The brigthest source (in both the K- and R-bands) at $z > 1.5$ is the BAL QSO at $z = 2.810$ (XID 62).

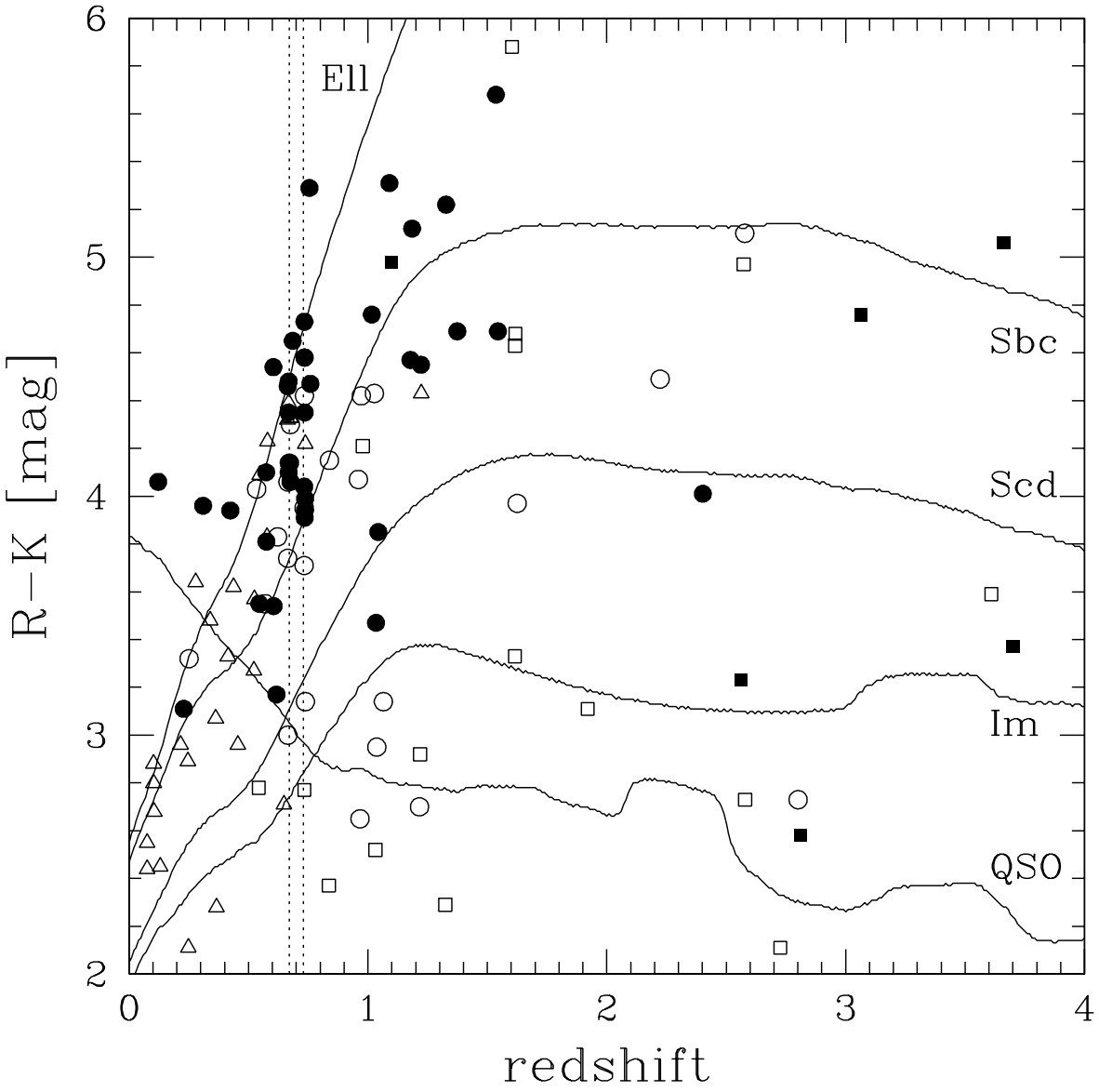

Fig. 19.— R−K colour as a function of redshift. Symbols are as in Figure 1. The five evolutionary tracks correspond to an unreddened QSO, with $L = L^{\star}_{\rm B}$, and unreddened elliptical, Sbc, Scd and irregular $L^{\star}$ galaxies from the Coleman et al. (1980) SED templates.

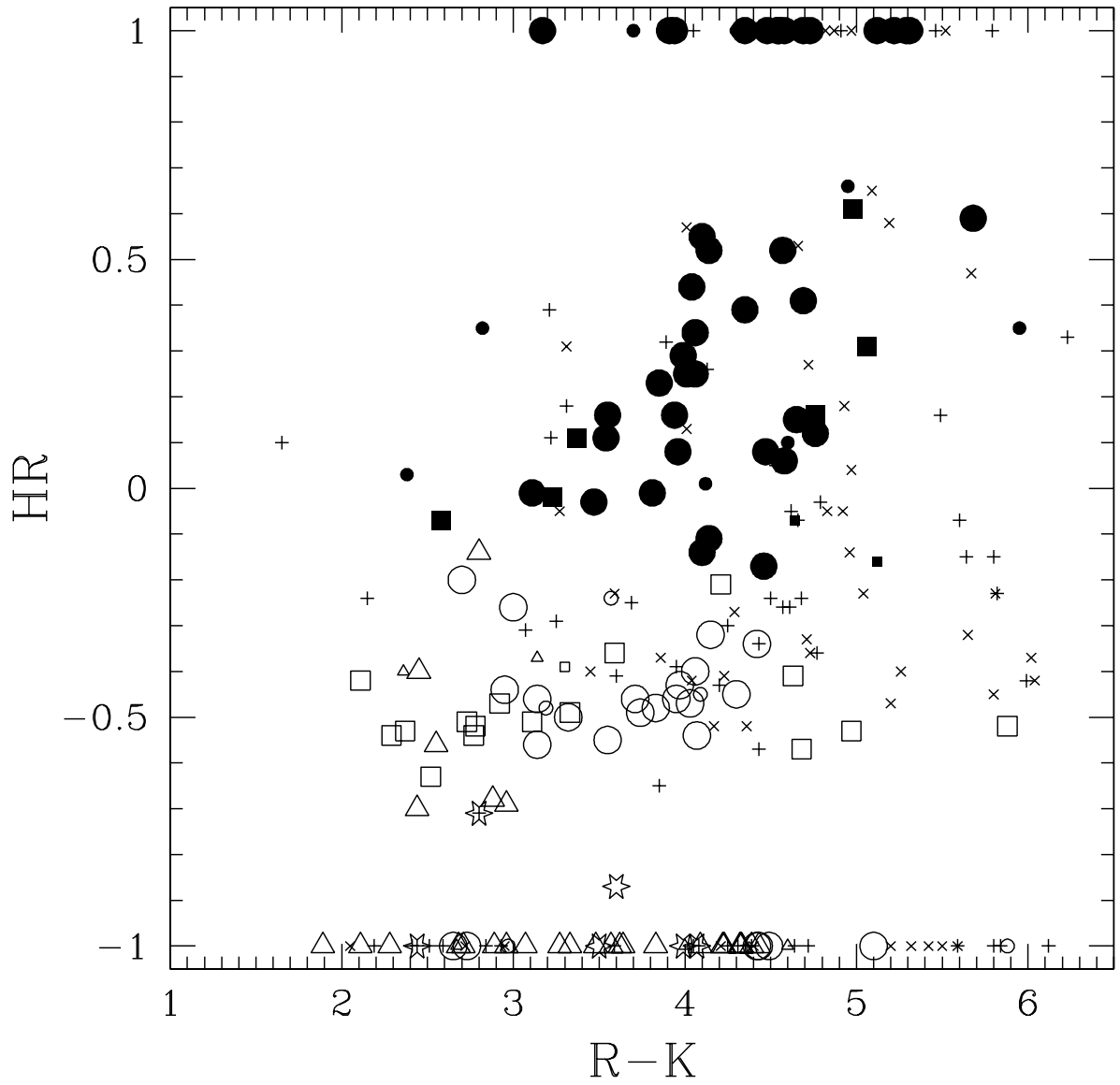

Fig. 20.— The hardness ratio (defined from the net count rates in the 2-10 keV and 0.5-2 keV bands: see Section 7) versus R−K colour. Symbols are as in Figure 1 for the reliable z identifications, similar symbols but of smaller sizes for the tentative z identifications.

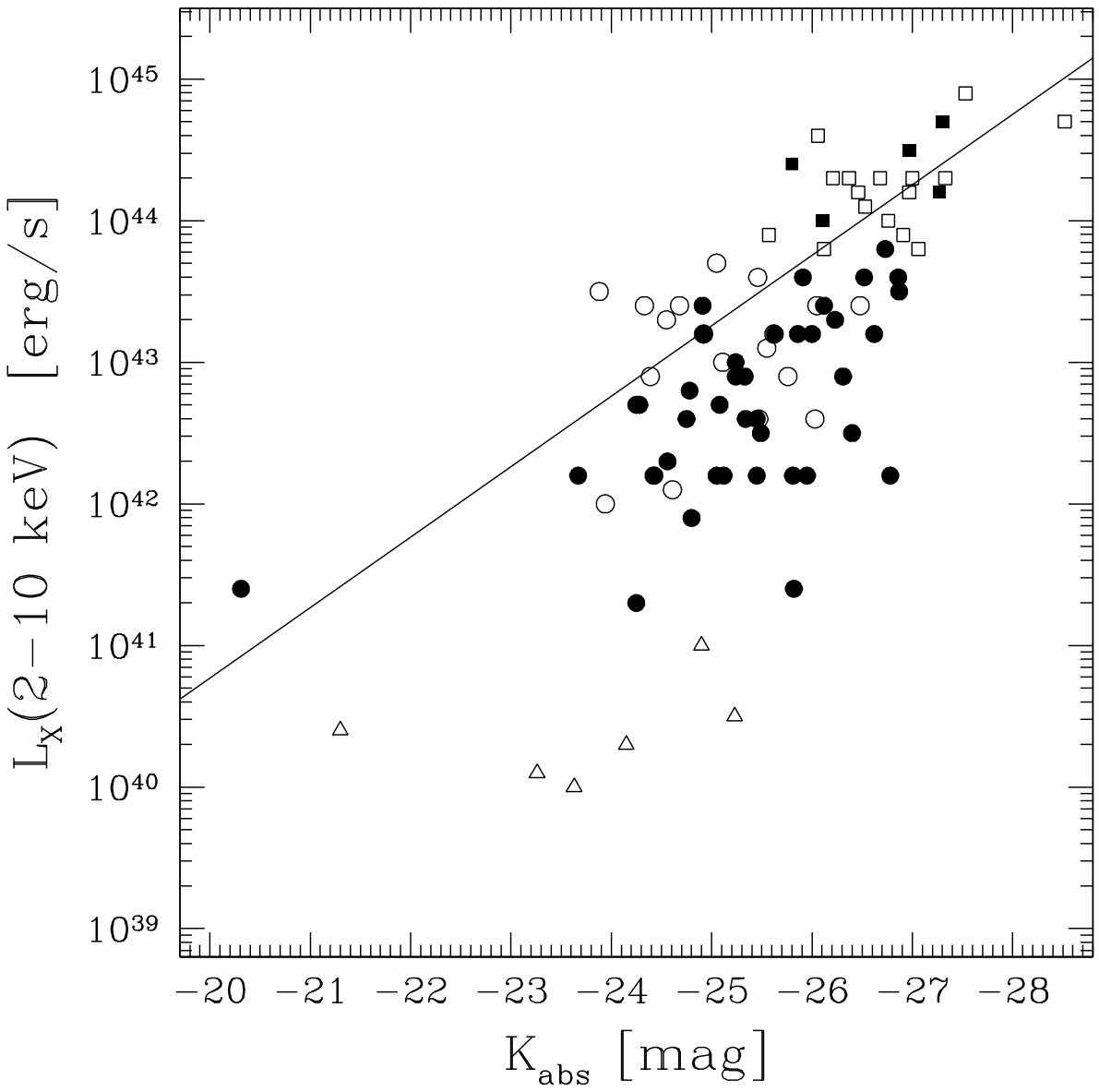

Fig. 21.— The X-ray luminosity in the 2-10 keV band versus the absolute K magnitude. Symbols are as in Figure 1. We also convert the relation found between *bulge* luminosity and black hole *mass* (Marconi & Hunt 2003), by assuming that around 40% of the K-band emission is coming from the bulge and an X-ray luminosity of 0.1% of the Eddington limit (Solid line).

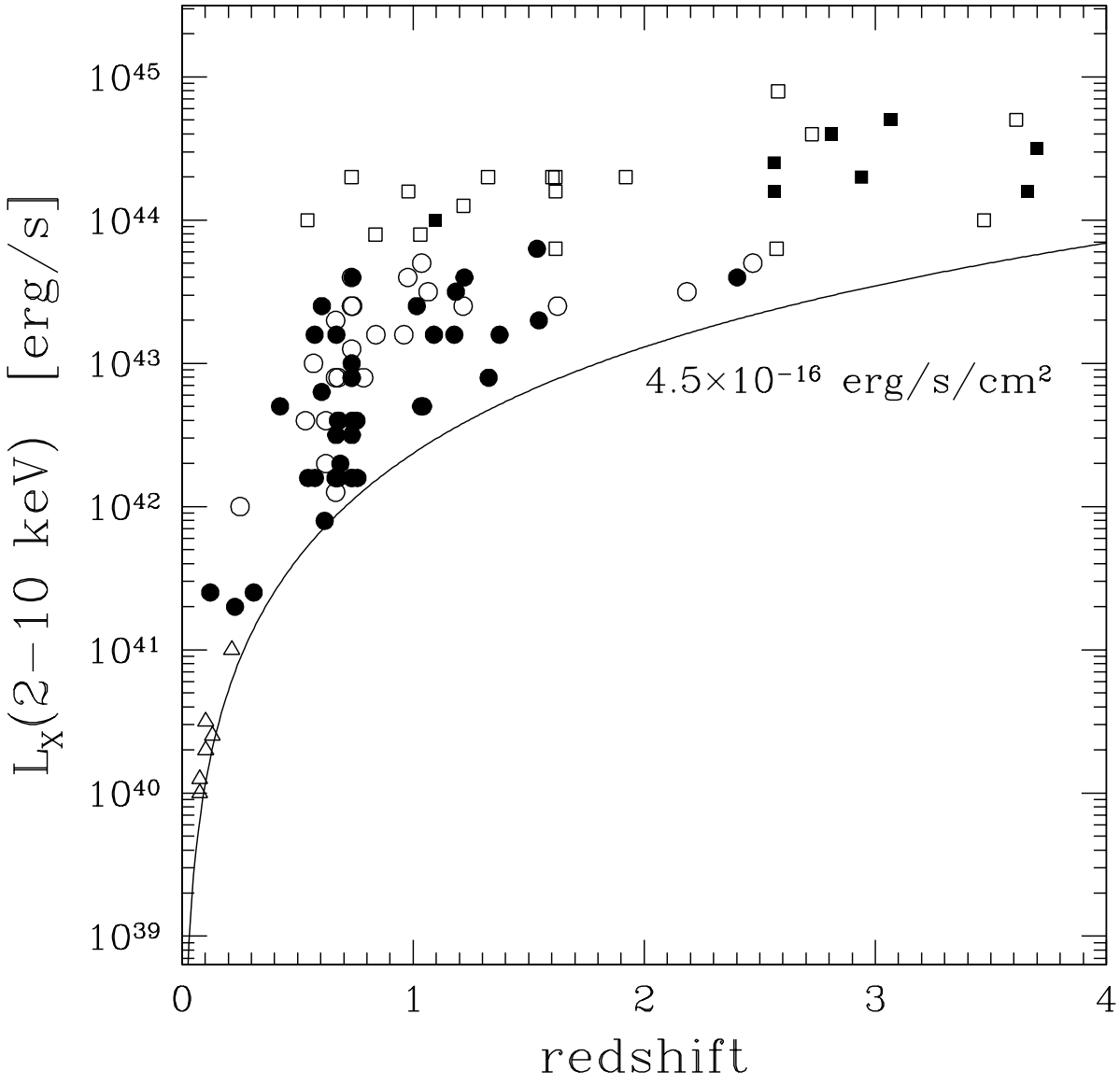

Fig. 22.— The X-ray luminosity in the 2-10 keV band versus redshift. Symbols are as in Figure 1.

Fig. 23.— For these figures, see http://www.mpe.mpg.de/CDFS/. Finding charts and VLT spectra of the field sources. Images are based on our FORS R-band imaging. The images are $20'' \times 20''$ in size. Next to the finding charts we show *all* spectroscopic observations available for the object. On the horizontal axis both the observed (bottom) and rest frame (top – if available) wavelength is shown in Å units. The vertical axis is the measured flux, f_λ in 10^{-18} erg cm^{-2} s^{-1} Å^{-1} units. Important emission (above the spectra) and absorption (below the spectra) features used for identification are also marked.

Table 1. X-ray sources not yet published in Giacconi et al. (2002).

XID[a]	CXO CDFS[b]	RA (J2000)[c]	Dec (J2000)[d]	Soft Cts.[e]	Hard Cts.[f]	Exp Time[g]	Soft Flux[h]	Error[i]	Hard Flux[j]	Error[k]	HR[l]
901	J033235.8-274917	03 32 35.78	-27 49 16.82	11.0±5.0	<9.0	828.4(857.7)	6.1e-17	2.9e-17	<3.1e-16		-1
902	J033222.1-275113	03 32 22.08	-27 51 13.05	<7.0	12.1±6.2	792.3(804.1)	<3.9e-17	–	4.5e-16	2.0E-16	+1
903	J033226.0-274049	03 32 25.97	-27 40 49.21	22.5±10.4	<3	824.3(820.2)	1.3e-16	0.6e-16	< 1e-16		-1

[a]Unique Detection ID

[b]IAU Registered Name, based on X–ray coordinates

[c]Right Ascension

[d]Declination

[e]Net Counts in soft (0.5 - 2 keV) band

[f]Net Counts in hard (2 - 10 keV) band

[g]Effective exposure time in the soft(hard) band, in kiloseconds

[h]Flux in soft (0.5 - 2 keV) band, c.g.s. units

[i]Error on soft flux

[j]Flux in hard (2 - 10 keV) band, c.g.s. units

[k]Error on hard flux

[l]Hardness Ratio, defined as (H - S)/(H + S) where H and S are the net counts in the hard and soft bands respectively

Table 2. X-ray-to-optical flux ratio ranges for different classes of objects

Object class	$\log(f_{0.3...3.5}/f_V)$	f_X-shift	V-R	$\log(f_{0.5...2.0}/f_R)$
AGN	$-1.0...+1.2$	$0.25...0.33$	$0.0...1.0$	$-1.4...+1.1$
BL Lac	$+0.3...+1.7$	$0.25...0.33$	$0.0...1.0$	$-0.1...+1.6$
Clusters	$-0.5...+1.5$	$0.18...0.25$	$0.1...0.4$	$-0.6...+1.6$
Galaxies	$-1.8...-0.2$	$0.10...0.30$	$0.1...1.0$	$-2.2...+0.0$
M stars	$-3.1...-0.5$	$0.05...0.20$	$0.6...1.0$	$-3.4...-0.4$
K stars	$-4.0...-1.5$	$0.05...0.20$	$0.4...0.6$	$-4.1...-1.3$
G stars	$-4.3...-2.4$	$0.05...0.20$	$0.3...0.5$	$-4.4...-2.2$
B-F stars	$-4.6...-3.0$	$0.05...0.20$	$-0.5...0.3$	$-4.6...-2.5$

Note. — The typical X-ray-to-optical flux ratios in our new bands ($0.5...2$ keV in X-ray, R-band in optical) as derived from the previously determined values (Stocke et al. 1991). The f_X-shift is the typical shift of X-ray flux (in $\log_{10}$ units) due to the narrower energy range, assuming typical X-ray spectra for the class of objects. V-R is the typical optical color range in the class. The last column includes our new normalization of the X-ray-to-optical flux ratio, as discussed in the text (Section 3). In the case of clusters, the magnitude refers to the brigtest cluster galaxy (BCG).

Table 3. The location of lines in second order diffraction

Line (Å)	Position[1] (Å)	Flux[1] (ADU)	FWHM[1] (Å)	Position[2] (Å)	Flux[2] (ADU)	FWHM[2] (Å)	Filter (Bessel)
3888.6	3887	13847	26	7462	3632	30	U
3650.1	3648	90265	30	6954	36364	35	U
3650.1	3649	17119	27	6957	8380	34	B
3888.6	3888	79904	27	7465	19142	30	B
4046.6	4047	346283	30	7801	44653	30	B
4358.3	4359	795630	28	8457	51040	30	B
4471.5	4472	97692	27	8694	5151	30	B
5015.7	5014	172340	28	9878	1946	33	V

Note. — The location, apparent width and apparent strength of selected arc lines in first and second order diffraction in FORS, using the 150I grism. Flux values are in instrumental counts (ADU). The *Filter* column indicates which (Bessel) filters we used for the particular line. The observed location of the first order diffraction was used to test that the filters do not introduce significant shifts in our wavelength solution.

Table 4. Summary of spectroscopic observations.

Mask	Exposure (s)	Slit (arcsec)	seeing (arcsec)	Slitloss %	Night
6+7	3×1800, 3×1800	1.2	0.8/0.6	40	2000 Oct 27-28
15	4×1800+1300	1.2	0.7/0.8	45	2000 Oct 27-28
22+23+24	3×1800, 1800, 2×1800	1.2	1.0/0.9	50	2000 Oct 28-29
28+29	2×1800, 3×1800	1.2	0.6/0.9	40	2000 Oct 28-29
36+39+40	1800, 1800, 4×1800	1.2	1.3/0.6	65	2000 Oct 29-30
46+47	4×1800, 1800+900	1.2	0.5/0.7	35	2000 Oct 29-30
78	6×1800+945	1.2	0.5/0.6	N/A	2000 Nov 24-25
82	5×1800	1.2	0.6/0.6	35	2000 Nov 23-24
84	6×1800	1.2	0.9/0.8	45	2000 Nov 23-24
86	3×1800+1535	1.2	1.1/1.0	40	2000 Nov 24-25
88	1200	1.2	0.8/0.6	80	2000 Nov 23-24
89	1200	1.2	0.8/0.6	75	2000 Nov 23-24
90	1200	1.2	1.3/1.1	90	2000 Nov 23-24
99	1800	1.2	0.9/1.3	50	2000 Nov 24-25
119+120+121	2700, 2×2700, 2×2700+3600	1.0	0.5/0.7	70	2001 Sep 20-21
122	4×2700	1.0	0.6/0.8	70	2001 Sep 18-19
134	2500+2700	1.4	0.9/0.8	70	2001 Sep 17-18, 19-20
137	1800+2700	1.4	1.0/1.0	60	2001 Sep 18-19, 19-20
138+139	3×1800, 2×2700	1.0	0.5/0.6	55	2001 Sep 17-18
146	3×2700	1.4	0.7/0.9	60	2001 Sep 19-20
MXU2.1	9×1800+2400	1.0	0.7/0.9	N/A	2001 Nov 13-14, 14-15
MXU4.1	12×1800+1134	1.0	0.9/0.8	N/A	2001 Nov 12-13
MXU5.1	4×1800	1.0	0.5/0.7	70	2001 Nov 14-15
MXU11.1	9×1800+2400	1.0	0.6/0.8	sl	2001 Nov 13-14
MOS11.1	4×1800	?.?	1.2/1.0	75?	2001 Nov 11-12
MXU1.1	2×2100	?.?	0.5/0.7	sl	2001 Dec 18-19

Note. — Seeing values refer to seeing directly measured on the acquisition image (first value) and the seeing measured by the DIMM seeing monitor during the observations (second number). The slitloss is estimated from relatively bright point sources (if observed) by comparing synthetic magnitudes calculated from the flux calibrated spectra and broad-band magnitudes. This value is only to be used to asses the overall quality of each mask as it does not take into account the extend and centering of individual objects (see Section 6.3).

Table 5. Optical spectroscopy results.

No	mask	α (J2000)	δ (J2000)	R (mag)	R−K (mag)	L_X $(\log \frac{erg}{s})$	HR	z	Class (opt)	Class (X-ray)	Qual	Comments
1a	36	03:33:09.49	−27:46:03.6	20.12	NA	42.5	−0.18	0.347	LEX	AGN-2	0.5	6650Å-
1b	39	03:33:09.65	−27:46:04.0	21.74	NA	43.6	−0.18	1.015	LEX	AGN-2	1.0	6700Å-
4a	36+39+40	03:33:03.63	−27:45:18.9	22.80	3.19	43.9	−0.48	1.260	BLAGN	AGN-1	1.0	4650Å-, Mg II
6a	36+39+40	03:33:02.69	−27:48:23.5	23.67	4.17		−0.52	-			0.0	4500Å-
10	36	03:32:59.77	−27:46:26.4	20.69	3.94	42.8	0.16	0.424	LEX	AGN-2	2.0+	
11	36+39+40	03:32:59.83	−27:47:48.2	21.83	2.73	45.0	−0.51	2.579	BLAGN	QSO-1	2.0+	C IV
12	137	03:32:59.69	−27:50:30.4	19.89	3.32	42.2	−0.50	0.251	ABS	AGN-1	2.0+	-9400Å
13	36	03:32:59.09	−27:43:39.5	20.93	3.71	43.6	−0.46	0.733	BLAGN	AGN-1	2.0+	Mg II, [O II]
15	15	03:32:52.88	−27:51:20.0	22.62	4.09		−0.45	-			0.0	6700Å-
15	137	03:32:52.88	−27:51:20.0	22.62	4.09	43.9	−0.45	1.227	BLAGN	AGN-1	1.0	Mg II
17c	15	03:32:49.11	−27:55:06.5	24.62	4.23		−0.41	-			0.0	
18	146	03:32:47.90	−27:42:32.8	21.28	4.21	44.3	−0.21	0.979	LEX	QSO-1	2.0+	
19	47	03:32:47.92	−27:41:48.0	21.76	3.95	43.8	−0.46	0.740	BLAGN	AGN-1	2.0+	[NeV]?, Mg II
19	84	03:32:47.92	−27:41:48.0	21.76	3.95	43.8	−0.46	0.733	BLAGN	AGN-1	2.0+	[NeV]?, [O II], Mg II
20a	86	03:32:44.46	−27:49:40.3	23.99	4.76	43.4	0.12	1.016	LEX	AGN-2	2.0+	3600Å-
20a	137	03:32:44.46	−27:49:40.3	23.99	4.76	43.4	0.12	1.016	LEX	AGN-2	2.0+	5400Å-
21	15	03:32:44.32	−27:52:51.3	23.96	<3.66	44.2	−0.58	3.476	BLAGN	QSO-1	2.0+	C IV
21	137	03:32:44.32	−27:52:51.3	23.96	<3.66	44.2	−0.58	3.471	BLAGN	QSO-1	2.0+	3950Å-,C IV
22	15	03:32:43.24	−27:49:14.2	22.59	3.11	44.4	−0.51	1.92	BLAGN	QSO-1	2.0+	5000Å-, Mg II
23	84	03:32:41.87	−27:44:00.2	24.93	<4.63		−0.46	-			0.0	
24	15	03:32:41.86	−27:52:02.6	22.58	3.59	44.8	−0.36	3.592	BLAGN	QSO-1	2.0+	C IV, [N IV], associated absorption system
24	137	03:32:41.86	−27:52:02.6	22.58	3.59	44.8	−0.36	3.610	BLAGN	QSO-1	2.0+	C IV, [N IV], associated absorption system
25	15	03:32:40.85	−27:55:47.0	24.64	5.95	43.1	0.35	0.625	ABS	AGN-2	0.5	
26	134	03:32:39.71	−27:46:11.1	24.55	5.04		−0.23	-			0.0	
26	146	03:32:39.71	−27:46:11.1	24.55	5.04		−0.23	-			0.0	
27	MXU2.1	03:32:39.67	−27:48:50.5	24.54	4.76	44.7	0.16	3.064	HEX	QSO-2	2.0+	CIV
28	86	03:32:39.09	−27:46:02.0	20.85	2.70	43.5	−0.20	1.216	BLAGN	AGN-1	2.0+	-8950Å, Mg II
30a	28+29	03:32:38.13	−27:39:45.0	20.42	2.37	44.1	−0.53	0.837	BLAGN	QSO-1	2.0+	Mg II, H_β, H_γ, [O II], [Ne V]
31	15	03:32:37.78	−27:52:12.4	24.57	5.88	44.4	−0.52	1.603	HEX	QSO-1	2.0+	HeII, C IV, absorbed below 2 keV
32	28+29	03:32:37.47	−27:40:00.3	22.36	3.74	43.1	−0.49	0.664	BLAGN	AGN-1	2.0+	broad H_β, [NeV]
33		03:32:36.79	−27:44:07.2	22.52	4.06	43.4	−0.40	0.665	LEX	AGN-1	2.0+	[O II] ref 1
34a	15	03:32:34.96	−27:55:11.2	22.86	4.15	43.3	−0.32	0.839	HEX	AGN-1	2.0+	-8400Å, [NeV]
36a	138+139	03:32:33.02	−27:45:47.6	23.38	6.02		−0.37	-			0.0	or arms

Table 5—Continued

No	mask	α (J2000)	δ (J2000)	R (mag)	R−K (mag)	L_X $(\log \frac{erg}{s})$	HR	z	Class (opt)	Class (X-ray)	Qual	Comments
36b	138+139	03:32:32.97	−27:45:45.8	20.82	3.86		−0.37	-			0.0	6550Å-
37*	46+47	03:32:32.09	−27:41:55.3	23.39	3.59		−0.23	-			0.0	4400Å-
37*	84	03:32:32.09	−27:41:55.3	23.39	3.59		−0.23	-			0.0	
37*	146	03:32:32.09	−27:41:55.3	23.39	3.59		−0.23	-			0.0	
38		03:32:30.30	−27:45:05.4	22.10	3.14	43.5	−0.56	0.738	BLAGN	AGN-1	2.0+	Mg II, H_β, [O III], ref 1
39		03:32:30.06	−27:45:30.7	21.02	2.92	44.3	−0.47	1.218	BLAGN	QSO-1	2.0+	Mg II, [Ne V], ref 2
41	22	03:32:27.62	−27:41:45.0	22.24	4.14	43.2	0.52	0.667	HEX	AGN-2	2.0+	H_β, [NeV]?
41	84	03:32:27.62	−27:41:45.0	22.24	4.14	43.3	0.52	0.668	HEX	AGN-2	2.0+	H_β, [NeV], line ratios
42a	28	03:32:27.00	−27:41:05.1	19.04	2.77	44.5	−0.54	0.734	BLAGN	QSO-1	2.0+	Mg II, [O III]
43	23+24	03:32:26.76	−27:41:45.6	22.61	4.58	43.0	0.06	0.737	LEX	AGN-2	2.0+	5500Å-
43	84	03:32:26.76	−27:41:45.6	22.61	4.58	43.0	0.06	0.734	LEX	AGN-2	2.0+	
44a	28	03:32:26.49	−27:40:35.7	19.79	2.52	44.2	−0.63	1.031	BLAGN	QSO-1	2.0+	Mg II, H_γ, [Ne V]
45	82	03:32:25.69	−27:43:05.8	25.35	5.12		−0.16	-			0.0	5000Å-
45	84	03:32:25.68	−27:43:05.7	25.35	5.12	44.4	−0.16	2.291	LEX	QSO-2	1.0	
46	82	03:32:25.16	−27:42:18.9	23.01	4.68	44.0	−0.57	1.617	BLAGN	QSO-1	2.0+	4000Å-, C IV, Mg II
47	139	03:32:24.97	−27:41:01.6	21.98	4.04	43.0	0.44	0.733	LEX	AGN-2	2.0+	6100Å-
49	22+23+24	03:32:24.25	−27:41:26.5	20.99	4.03	42.8	−0.47	0.534	LEX	AGN-1	2.0+	4600Å-
50	119+120+121	03:32:19.00	−27:47:55.4	24.14	2.38	42.7	0.03	0.670	ABS	AGN-2	1.0	
50	138+139	03:32:19.00	−27:47:55.4	24.14	2.38		0.03	-			0.0	
50	MXU1.1	03:32:19.05	−27:47:55.4	24.14	2.38		0.03	-			0.0	
51a	6+7	03:32:17.18	−27:52:20.8	23.22	4.98	44.0	0.61	1.097	LEX	QSO-2	2.0+	
52	82	03:32:17.15	−27:43:03.4	21.04	3.55	43.2	−0.55	0.569	BLAGN	AGN-1	2.0+	Mg II, [O III]
53	78	03:32:14.99	−27:51:27.2	21.59	4.30	43.0	−0.45	0.668	LEX	AGN-1	2.0+	
53	119+120+121	03:32:14.99	−27:51:27.2	21.59	4.30	43.0	−0.45	0.675	BLAGN	AGN-1	2.0+	-9500Å, Mg II
54	122	03:32:14.61	−27:54:20.7	25.69	<5.39	44.3	−0.07	2.561	HEX	QSO-2	2.0+	C IV
55	6	03:32:14.02	−27:51:00.9	22.53	4.06	41.5	0.25	0.122	HEX	AGN-2	2.0+	H_α, [FeVII], low LX AGN-2
56a	23	03:32:13.24	−27:42:41.1	20.18	3.54	43.5	0.11	0.605	HEX	AGN-2	2.0+	H_β, [NeV]
57	122	03:32:12.96	−27:52:36.9	24.04	3.23	44.5	−0.02	2.562	HEX	QSO-2	2.0+	C IV, He II
59	78	03:32:11.33	−27:52:13.7	26.47	<6.17		−0.21	-			0.0	
59	MXU4.1	03:32:11.34	−27:52:13.7	26.47	<6.17		−0.21	-			0.0	
60	22+23+24	03:32:10.92	−27:44:15.2	22.51	3.33	44.5	−0.49	1.60	BLAGN	QSO-1	2.0+	C IV, Mg II
60	82	03:32:10.92	−27:44:15.2	22.51	3.33	44.5	−0.49	1.615	BLAGN	QSO-1	2.0+	3600Å-, C IV, Mg II
61	22+23+24	03:32:10.47	−27:43:09.1	23.98	5.80		−0.45	-			0.0	nearby bright star
62	6+7	03:32:09.46	−27:48:06.8	20.39	2.58	44.6	−0.07	2.810	BLAGN	QSO-2	2.0+	BAL QSO, C IV, [O III]

Table 5—Continued

No	mask	α (J2000)	δ (J2000)	R (mag)	R−K (mag)	L_X $(\log \frac{erg}{s})$	HR	z	Class (opt)	Class (X-ray)	Qual	Comments
63	22+23+24	03:32:08.68	−27:47:34.4	18.50	2.78	44.2	−0.52	0.544	BLAGN	QSO-1	2.0+	Mg II, H_β, [Ne V]
63	88	03:32:08.68	−27:47:34.4	18.50	2.78	44.1	−0.52	0.543	BLAGN	QSO-1	2.0+	-8850Å, Mg II, H_β, [NeV]
64	139	03:32:08.01	−27:46:57.3	24.77	<4.47		−0.34	-			0.0	
65	MOS11.1	03:32:03.86	−27:53:29.8	-	K20.34		−0.48	-			0.0	
66	22	03:32:03.67	−27:46:03.8	20.72	4.10	43.2	0.55	0.574	LEX	AGN-2	2.0+	-8700Å
67	82	03:32:02.47	−27:46:00.4	23.56	4.63	44.4	−0.41	1.616	BLAGN	QSO-1	2.0+	4200Å-, Mg II
68	22+23+24	03:32:01.58	−27:43:27.0	22.83	2.11	44.7	−0.42	2.726	BLAGN	QSO-1	2.0+	-7700Å, C IV
70a	22+23+24	03:32:01.53	−27:46:46.8	23.62	5.67		0.47	-			0.0	-8000Å
71	82	03:32:00.35	−27:43:19.6	22.10	2.95	43.8	−0.44	1.037	BLAGN	AGN-1	2.0+	Mg II, [Ne V]
73	MXU11.1	03:31:58.12	−27:48:34.0	22.14	4.42	43.2	−0.34	0.734	LEX	AGN-1	2.0+	
73	MOS11.1	03:31:58.02	−27:48:34.7	22.14	4.42	43.2	−0.34	0.734	LEX	AGN-1	2.0+	
75	MXU11.1	03:31:55.38	−27:54:48.4	20.75	3.99	43.7	0.29	0.737	HEX	AGN-2	2.0+	[NeV], 4200A-
75	MOS11.1	03:31:55.38	−27:54:48.4	20.75	3.99	43.7	0.29	0.737	HEX	AGN-2	2.0+	[NeV], line ratios
76	MOS11.1	03:31:52.49	−27:50:17.6	24.50	4.64	44.6	−0.07	2.394	LEX	QSO-2	1.0	
77	36+39+40	03:33:01.54	−27:45:42.6	20.63	3.83	42.8	−0.48	0.622	BLAGN	AGN-1	2.0+	3950Å-, Mg II, [O II]
78	22+23+24	03:32:30.06	−27:45:23.6	22.44	4.07	43.4	−0.54	0.960	LEX	AGN-1	1.0	7000Å-
78	84	03:32:30.06	−27:45:23.6	22.44	4.07	43.4	−0.54	0.960	BLAGN	AGN-1	2.0+	4200Å-, Mg II, [O II]
79	84	03:32:37.99	−27:46:26.3	26.55	6.04		−0.42	-			0.0	6000Å-
79	MXU2.1	03:32:38.02	−27:46:26.4	26.55	6.04		−0.42	-			0.0	
80	78	03:32:10.92	−27:48:57.0	24.63	4.36		−0.52	-			0.0	
80	119+120+121	03:32:10.93	−27:48:57.3	24.63	4.36		−0.52	-			0.0	
81	138+139	03:32:25.95	−27:45:14.4	26.04	<5.74		−0.44	-			0.0	
82a	122	03:32:14.86	−27:51:04.0	-	K19.00		−0.01	-			0.0	
82b	78	03:32:15.08	−27:51:04.6	25.94	<5.64		−0.01	-			0.0	
83	22+23+24	03:32:14.98	−27:42:24.9	23.08	5.81		−0.23	-			0.0	
83	139	03:32:14.98	−27:42:24.9	23.08	5.81		−0.23	-			0.0	
83	MXU5.1	03:32:14.98	−27:42:24.9	23.08	5.81		−0.23	-			0.0	
84		03:32:46.77	−27:42:12.2	16.03	2.88	40.7	−0.68	0.103	ABS	gal	2.0+	2dF TGS243Z005
85	15	03:32:44.60	−27:48:35.9	24.78	3.30		−0.39	-			0.0	5850Å-
85	MXU2.1	03:32:44.60	−27:48:35.9	24.78	3.30	44.0	−0.39	2.593	LEX	QSO-1	1.0	
86a	84	03:32:33.85	−27:45:20.7	24.65	3.27		−0.05	-			0.0	4200Å-
86a	134	03:32:33.84	−27:45:20.6	24.65	3.27		−0.05	-			0.0	
87	6+7	03:32:18.25	−27:52:41.4	23.98	2.73	43.3	−1.00	2.801	BLAGN	AGN-1	2.0+	C IV
89	22+23+24	03:32:08.28	−27:41:53.6	24.58	<4.28	43.9	−0.44	2.47	BLAGN	AGN-1	2.0+	C IV

Table 5—Continued

No	mask	α (J2000)	δ (J2000)	R (mag)	R−K (mag)	L_X ($\log \frac{erg}{s}$)	HR	z	Class (opt)	Class (X-ray)	Qual	Comments
90		03:32:42.12	−27:57:04.1	13.82X	3.60		−0.87	0	M-star	M-star	2.0+	ref 3
91	86	03:32:42.84	−27:47:02.6	24.10	<3.80	44.4	−0.31	3.193	BLAGN	QSO-1	1.0	C IV
92		03:32:49.65	−27:54:53.9	16.91	2.80		−0.71	0	star	star	2.0+	ref 3
93	78	03:32:02.34	−27:52:34.0	23.67	4.04		−0.42	-			0.0	contamination, 4000Å-
94a	39+40	03:32:44.00	−27:46:33.5	24.72	<4.42		−1.00	-			0.0	-8600Å
94a	86	03:32:44.00	−27:46:34.0	24.72	<4.42		−1.00	-			0.0	contamination
94b	84	03:32:43.98	−27:46:32.7	24.50	<4.20		−1.00	-			0.0	6000Å-
94c	39+40	03:32:44.00	−27:46:35.1	24.83	<4.53	43.5	−1.00	2.688	LEX	AGN-1	0.5	-8600Å
94c	146	03:32:44.01	−27:46:35.1	24.83	<4.53		−1.00	-			0.0	4600Å-
95		03:32:29.92	−27:44:25.2	16.49	2.44	40.3	−0.70	0.076	LEX	gal	2.0+	ref 2
96a	78	03:32:20.92	−27:52:22.6	24.85	<4.55		−0.39	-			0.0	
97a	22+23+24	03:32:10.99	−27:40:53.7	23.56	3.45		−0.40	-			0.0	
97b	22+23+24	03:32:11.09	−27:40:56.1	19.56	2.36	41.7	−0.40	0.181	LEX	gal	2.0	not centered
98a	137	03:32:44.28	−27:51:41.2	19.75	3.64	41.0	−1.00	0.279	HEX	gal	2.0+	H_α, H_β, [NeV], interacting, possible low L_X AGN-1
98b	137	03:32:44.06	−27:51:43.3	19.19	4.00	41.0	−1.00	0.279	ABS	gal	1.0	interacting
99	MOS11.1	03:32:05.11	−27:53:55.1	25.22	5.65		−0.32	-			0.0	
100	86	03:32:35.98	−27:48:50.4	22.00	2.97	42.3	−1.00	1.309	LEX	AGN-1	1.0	
101a	86	03:32:55.60	−27:47:51.9	24.69	3.97		−0.43	-			0.0	4300Å-
101a	MXU2.1	03:32:55.50	−27:47:51.9	24.69	3.97	43.6	−0.43	1.625	BLAGN	AGN-1	2.0+	C IV, Mg II
103		03:32:28.90	−27:43:56.2	18.19X	2.96	41.3	−0.69	0.215	ABS	gal	2.0+	ref 2
108a	82	03:32:05.78	−27:44:47.2	25.94	<5.64		−0.36	-			0.0	
108b	82	03:32:05.72	−27:44:48.2	26.36	<6.06		−0.36	-			0.0	
110	86	03:32:58.61	−27:46:32.0	23.25	<2.95	42.4	−0.21	0.622	LEX	AGN-1	1.0	
110	MXU2.1	03:32:58.61	−27:46:32.0	23.25	<2.95	42.4	−0.21	0.622	LEX	AGN-1	2.0+	
112a	MXU11.1	03:31:51.94	−27:53:27.4	24.83	<4.53	44.3	0.20	2.940	HEX	QSO-2	2.0+	HeII, NV, OVI
114	78	03:32:07.63	−27:52:13.7	24.52	4.92		−0.05	-			0.0	
114	122	03:32:07.63	−27:52:13.7	24.52	4.92		−0.05	-			0.0	-8550Å
114	MXU4.1	03:32:07.63	−27:52:13.7	24.52	4.92		−0.05	-			0.0	
116*		03:32:30.07	−27:44:05.4	16.97	2.55	40.3	−0.56	0.076	LEX	gal	2.0+	ref 2
117	82	03:32:03.05	−27:44:50.2	25.47	4.97	44.0	−0.53	2.573	HEX	QSO-1	2.0+	CIV
121	MXU11.1	03:31:51.16	−27:50:51.6	22.44	4.14	42.7	−0.11	0.674	LEX	AGN-2	2.0+	
122	86	03:32:57.60	−27:45:48.6	23.14	<2.84		−0.21	-			0.0	
124a	82	03:32:02.47	−27:45:24.2	25.29	<4.99		−1.00	-			0.0	
124b	22+23+24	03:32:02.44	−27:45:25.9	24.94	<4.64		−1.00	-			0.0	

Table 5—Continued

No	mask	α (J2000)	δ (J2000)	R (mag)	R−K (mag)	L_X $\left(\log \frac{erg}{s}\right)$	HR	z	Class (opt)	Class (X-ray)	Qual	Comments
124b	82	03:32:02.43	−27:45:25.8	24.94	<4.64		−1.00	-			0.0	
132*	15	03:32:44.01	−27:54:54.1	24.89	<4.59	42.8	−0.05	0.908	LEX	AGN-2	1.0	
138a*	46	03:32:50.11	−27:41:34.8	22.22	4.42	42.6	−1.00	0.972	BLAGN	AGN-1	2.0+	Mg II, [O II], interacting
138b*	47	03:32:50.01	−27:41:35.8	22.68	2.65	42.6	−1.00	0.967	LEX	AGN-1	2.0+	
145	6+7	03:32:22.54	−27:46:03.9	24.78	4.72		0.27	-			0.0	6950Å-
145	84	03:32:22.54	−27:46:03.9	24.78	4.72		0.27	-			0.0	
145	119+120+121	03:32:22.54	−27:46:03.9	24.78	4.72		0.27	-			0.0	6400Å-
147*	84	03:32:46.34	−27:46:32.1	25.14	5.09		0.65	-			0.0	6200Å-
147*	86	03:32:46.34	−27:46:32.1	25.14	5.09		0.65	-			0.0	
147*	MXU2.1	03:32:46.34	−27:46:32.1	25.14	5.09		0.65	-			0.0	
148	15	03:32:35.22	−27:53:17.9	-	-		0.00	-			0.0	
149		03:32:12.30	−27:46:21.8	23.05	4.60	42.8	0.10	1.033	LEX	AGN-2	1.0	ref 1: [O II]
150	78	03:32:25.16	−27:54:50.1	23.02	5.31	43.2	1.00	1.090	ABS	AGN-2	2.0+	4200Å-
151	6+7	03:32:20.48	−27:47:32.3	22.52	4.54	42.8	1.00	0.604	LEX	AGN-2	2.0+	
151	22+23+24	03:32:20.48	−27:47:32.3	22.52	4.54	42.8	1.00	0.604	LEX	AGN-2	1.0	3900Å-
152	36+39+40	03:32:59.31	−27:48:58.9	23.04	4.66		0.53	-			0.0	Not centered
152	MXU2.1	03:32:59.33	−27:48:59.0	23.04	4.66		0.53	-			0.0	
153	6+7	03:32:18.35	−27:50:55.3	24.20	5.68	43.9	0.59	1.536	HEX	AGN-2	2.0+	HeII?, CIV
155	24	03:32:07.98	−27:42:39.4	22.37	3.55	42.2	0.16	0.545	LEX	AGN-2	2.0+	line ratios
156	MXU4.1	03:32:13.23	−27:55:28.7	22.81	5.12	43.5	1.00	1.185	ABS	AGN-2	2.0+	[NEV]?
170	15	03:32:46.41	−27:54:14.0	20.69	4.46	42.3	−0.17	0.664	ABS	AGN-2	2.0+	[OII]?
171	84	03:32:35.10	−27:44:10.9	23.55	4.12		0.01	-			0.0	
171		03:32:35.19	−27:44:11.6	23.55	4.12	42.5	0.01	0.839	LEX	AGN-2	1.0	ref 1: [O II]
173	MXU5.1	03:32:16.74	−27:43:27.7	22.31	3.57	40.9	−1.00	0.524	LEX	gal	2.0+	[OII]?
173	MXU1.1	03:32:16.76	−27:43:27.5	22.31	3.57	40.9	−1.00	0.524	LEX	gal	2.0+	
175a	36	03:32:52.06	−27:44:35.1	20.10	2.67	40.5	−1.00	0.277	LEX	gal	2.0	line ratios
175b	39+40	03:32:51.86	−27:44:36.7	20.27	3.27	41.1	−1.00	0.522	HEX	gal	2.0+	possible low LX AGN-2, [NeV]
176	36+39+40	03:33:09.25	−27:44:50.0	22.25	NA	43.0	−0.27	0.786	LEX	AGN-1	2.0+	6600Å-
177a	137	03:32:56.98	−27:50:08.8	23.78	5.42		−1.00	-			0.0	
177b	137	03:32:56.86	−27:50:08.5	25.69	<5.39		−1.00	-			0.0	
178	6+7	03:32:13.87	−27:50:34.0	26.02	<5.72		−1.00	-			0.0	
184	15	03:32:48.18	−27:52:56.8	20.97	4.35	42.5	0.39	0.667	ABS	AGN-2	2.0+	
185	22+23+24	03:32:10.92	−27:43:43.3	21.80	4.01		0.13	-			0.0	
185	MXU1.1	03:32:10.94	−27:43:43.1	21.80	4.01		0.13	-			0.0	

Table 5—Continued

No	mask	α (J2000)	δ (J2000)	R (mag)	R−K (mag)	L_X $(\log \frac{erg}{s})$	HR	z	Class (opt)	Class (X-ray)	Qual	Comments
185	134	03:32:10.92	−27:43:43.3	21.80	4.01		0.13	-			0.0	5000Å-
185	MXU5.1	03:32:10.92	−27:43:43.3	21.80	4.01		0.13	-			0.0	
186	40	03:32:52.34	−27:45:56.4	23.09	2.72		−1.00	-			0.0	
186	86	03:32:52.34	−27:45:56.7	23.09	2.72		−1.00	-			0.0	
186	146	03:32:52.34	−27:45:56.7	23.09	2.72		−1.00	-			0.0	
186	MXU2.1	03:32:52.34	−27:45:56.7	23.09	2.72		−1.00	-			0.0	
188	122	03:32:22.56	−27:49:49.8	22.88	4.73	42.2	1.00	0.734	LEX	AGN-2	2.0+	
189d	146	03:32:45.73	−27:42:12.9	23.19	5.29	42.6	1.00	0.755	LEX	AGN-2	2.0+	
190	28+29	03:32:35.86	−27:40:59.6	22.39	4.35	42.9	1.00	0.733	LEX	AGN-2	2.0+	line ratios
190	46+47	03:32:35.86	−27:40:59.6	22.39	4.35	42.9	1.00	0.735	LEX	AGN-2	2.0+	
200a	46+47	03:32:54.97	−27:45:07.1	23.53	4.96		−0.14	-			0.0	5400Å-
200b	46+47	03:32:54.72	−27:45:05.9	24.54	<4.24		−0.14	-			0.0	
201b	84	03:32:38.94	−27:44:39.4	24.34	<4.04	42.7	−0.06	0.679	HEX	AGN-2	2.0+	H_β, [NeV], line ratios
202	78	03:32:29.86	−27:51:05.8	23.97	3.37	44.6	0.11	3.700	HEX	QSO-2	2.0+	C IV, HeII, NV, OVI
204	22+23+24	03:32:23.15	−27:45:54.9	23.42	4.43		−1.00	-			0.0	4600Å-
204	MXU1.1	03:32:23.20	−27:45:54.7	23.42	4.43		−1.00	-			0.0	
204		03:32:23.23	−27:45:55.3	23.42	4.43	41.9	−1.00	1.223	LEX	gal	2.0+	ref 1, [O II]
205b	82	03:32:17.48	−27:41:36.1	24.23	<3.93		0.16	-			0.0	
205c	82	03:32:17.55	−27:41:35.4	24.90	<4.60	42.3	0.16	0.53	LEX	AGN-2	0.5	
206	MXU5.1	03:32:16.20	−27:39:30.6	19.81	2.29	44.5	−0.54	1.324	BLAGN	QSO-1	2.0+	Mg II
207a	MXU5.1	03:32:07.90	−27:37:33.7	24.03	NA		0.36	-			0.0	
209	MXU11.1	03:31:47.22	−27:53:14.3	24.63	4.71		−0.33	-			0.0	
211	122	03:32:05.91	−27:54:49.7	21.10	4.33	41.8	−1.00	0.679	ABS	gal	2.0+	-7900Å
217b	15	03:32:33.30	−27:52:03.6	25.77	<5.47		−1.00	-			0.0	
218a	6+7	03:32:16.38	−27:52:01.3	23.38	3.14	41.9	−0.37	0.497	LEX	gal	0.5	
218b	78	03:32:16.41	−27:51:59.2	25.78	<5.48		−0.37	-			0.0	
218b	119+120+121	03:32:16.42	−27:51:59.2	25.78	<5.48		−0.37	-			0.0	
220a	119+120+121	03:32:32.75	−27:51:51.3	23.30	5.20		−1.00	-			0.0	contamination
220b	6+7	03:32:32.48	−27:51:49.5	22.91	<2.61		−1.00	-			0.0	5600Å-
221	82	03:32:08.86	−27:44:24.7	-	-		−1.00	-			0.0	
221	MXU1.1	03:32:08.86	−27:44:24.7	-	-		−1.00	-			0.0	
222	46+47	03:32:54.52	−27:45:02.0	23.81	5.26		−0.40	-			0.0	5350Å-
222	146	03:32:54.52	−27:45:02.0	23.81	5.26		−0.40	-			0.0	6500Å-
224	23+24	03:32:28.73	−27:46:20.4	22.03	4.22	41.8	−1.00	0.738	ABS	gal	2.0+	6600Å-

Table 5—Continued

No	mask	α (J2000)	δ (J2000)	R (mag)	R−K (mag)	L_X $\left(\log \frac{erg}{s}\right)$	HR	z	Class (opt)	Class (X-ray)	Qual	Comments
224	84	03:32:28.73	−27:46:20.4	22.03	4.22	41.8	−1.00	0.738	LEX	gal	2.0+	5600Å-
229	36	03:32:56.31	−27:48:33.8	17.06	2.68	39.8	−1.00	0.103	ABS	gal	2.0+	contamination
229	MXU2.1	03:32:56.33	−27:48:34.0	17.06	2.68	39.8	−1.00	0.105	ABS	gal	2.0+	
230	MXU11.1	03:31:53.55	−27:48:43.1	24.21	<3.91	43.6	−0.45	2.174	BLAGN	AGN-1	2.0+	C IV
230	MOS11.1	03:31:53.55	−27:48:43.1	24.21	<3.91	43.6	−0.45	2.185	BLAGN	AGN-1	2.0+	C IV
233	7	03:32:25.76	−27:49:36.3	20.46	3.83	41.0	−1.00	0.577	LEX	gal	2.0+	5150Å-, contamination
236	6+7	03:32:11.47	−27:50:06.9	23.85	5.20		−0.47	-			0.0	
236	MXU4.1	03:32:11.46	−27:50:06.8	23.85	5.20		−0.47	-			0.0	
237	137	03:32:58.53	−27:50:07.8	17.80	4.07		−1.00	0	M-star	M-star	2.0+	-8950Å. M-5 or 6
238	MXU11.1	03:31:47.97	−27:50:45.5	23.53	3.14	43.6	−0.46	1.065	BLAGN	AGN-1	2.0+	Mg II, [NeV]
239a	15	03:32:36.18	−27:51:26.6	24.57	4.29		−0.27	-			0.0	
239a	119+120+121	03:32:36.18	−27:51:26.6	24.57	4.29		−0.27	-			0.0	4500Å-
239b	119+120+121	03:32:36.31	−27:51:28.5	25.53	<5.23		−0.27	-			0.0	4500Å-
241	82	03:32:24.21	−27:42:57.7	24.76	4.73		−0.36	-			0.0	4550Å-
241	84	03:32:24.21	−27:42:57.7	24.76	4.73		−0.36	-			0.0	
242	46+47	03:32:51.84	−27:42:29.6	22.49	4.43	42.4	−1.00	1.027	LEX	AGN-1	2.0+	
243	MXU5.1	03:32:08.40	−27:40:46.9	-	-		0.04	-			0.0	
247		03:32:35.10	−27:55:33.2	16.27	3.31	39.7	0.31	0.038	LEX	gal	2.0+	ULX, 2dF TGS243Z011
248	MXU4.1	03:32:10.20	−27:54:16.2	23.18	4.65	42.3	0.15	0.685	ABS	AGN-2	2.0+	
251a	6+7	03:32:07.26	−27:52:31.3	23.85	<3.55		0.04	-			0.0	-8100Å
251a	MOS11.1	03:32:07.18	−27:52:31.7	23.85	<3.55		0.04	-			0.0	4500Å-
251b	MXU4.1	03:32:07.27	−27:52:29.1	24.49	4.97		0.04	-			0.0	
251b	MOS11.1	03:32:07.17	−27:52:29.5	24.49	4.97		0.04	-			0.0	4500Å-
252	39+40	03:32:47.05	−27:43:46.4	23.25	4.57	43.2	0.52	1.172	LEX	AGN-2	2.0+	
252	46+47	03:32:47.03	−27:43:46.8	23.25	4.57	43.2	0.52	1.180	LEX	AGN-2	2.0+	4750Å-
252	146	03:32:47.03	−27:43:46.8	23.25	4.57	43.2	0.52	1.178	LEX	AGN-2	2.0+	
253	22+23+24	03:32:20.05	−27:44:47.4	24.94	4.95	42.4	0.66	0.484	LEX	AGN-2	1.0	3500Å-
253	MXU1.1	03:32:20.08	−27:44:47.2	24.94	4.95	42.4	0.66	0.481	LEX	AGN-2	1.0	
254	138+139	03:32:19.89	−27:45:18.0	23.87	<3.57		1.00	-			0.0	
254	MXU1.1	03:32:19.92	−27:45:17.8	23.87	<3.57		1.00	-			0.0	
256	39+40	03:32:43.03	−27:48:44.2	24.36	4.01		0.57	-			0.0	-8200Å
256	86	03:32:43.05	−27:48:44.7	24.36	4.01		0.57	-			0.0	
256	MXU2.1	03:32:43.05	−27:48:44.7	24.36	4.01		0.57	-			0.0	
257a	6+7	03:32:13.38	−27:48:57.7	24.17	<3.87		0.35	-			0.0	

Table 5—Continued

No	mask	α (J2000)	δ (J2000)	R (mag)	R−K (mag)	$L_{\rm X}$ $\left(\log \frac{erg}{s}\right)$	HR	z	Class (opt)	Class (X-ray)	Qual	Comments
257b	6+7	03:32:13.19	−27:48:56.0	22.57	2.82	42.2	0.35	0.549	LEX	AGN-2	1.0	
259	78	03:32:06.12	−27:49:27.8	24.44	5.19		0.58	-			0.0	
259	122	03:32:06.12	−27:49:27.8	24.44	5.19		0.58	-			0.0	-8000Å
259	MXU4.1	03:32:06.12	−27:49:27.8	24.44	5.19		0.58	-			0.0	
259	MOS11.1	03:32:06.04	−27:49:28.3	24.44	5.19		0.58	-			0.0	
260	15	03:32:25.11	−27:50:43.3	23.81	3.85	42.7	0.23	1.043	LEX	AGN-2	2.0+	
261	MXU11.1	03:31:57.11	−27:51:19.4	-	-		0.50	-			0.0	
263a	78	03:32:18.87	−27:51:34.3	24.68	<4.38	42.5	0.31	0.70	LEX	AGN-2	0.5	
263b	MXU4.1	03:32:18.83	−27:51:35.6	25.33	5.06	44.2	0.31	3.660	HEX	QSO-2	2.0+	CIV
264	6+7	03:32:29.76	−27:51:47.1	23.44	<3.14	43.2	0.60	1.318	LEX	AGN-2	1.0	5000Å-
264	15	03:32:29.76	−27:51:47.1	23.44	<3.14	43.2	0.60	1.315	LEX	AGN-2	1.0	
264	122	03:32:29.76	−27:51:47.1	23.44	<3.14	43.2	0.60	1.316	LEX	AGN-2	1.0	5350-
266	82	03:32:13.86	−27:42:49.0	21.70	3.91	42.5	1.00	0.735	LEX	AGN-2	2.0+	
267	82	03:32:04.84	−27:41:27.7	23.72	3.70		1.00	-			0.0	
267	MXU5.1	03:32:04.87	−27:41:27.6	23.72	3.70	43.0	1.00	0.720	LEX	AGN-2	1.0	MgII
268a	46	03:32:49.20	−27:40:50.6	22.33	4.55	43.6	1.00	1.222	HEX	AGN-2	2.0+	He II, [NeIV]
511a*	146	03:32:36.50	−27:46:29.2	22.29	3.57	42.2	−0.24	0.767	LEX	AGN-1/grp	2.0	6450Å-
511a*	MXU2.1	03:32:36.50	−27:46:29.2	22.29	3.57	42.2	−0.24	0.764	LEX	AGN-1	2.0	
511b*	146	03:32:36.47	−27:46:28.3	23.26	<2.96		−0.24	-			0.0	6450Å-
512	134	03:32:34.50	−27:43:50.3	22.07	4.10	42.3	−0.14	0.665	LEX	AGN-2	2.0+	
512	146	03:32:34.35	−27:43:50.3	22.07	4.10	42.3	−0.14	0.668	LEX	AGN-2	2.0+	
513a	119+120+121	03:32:34.02	−27:49:00.9	26.06	<5.76		0.23	-			0.0	
513b	MXU2.1	03:32:34.10	−27:48:58.3	26.25	<5.95		0.23	-			0.0	
514*		03:32:33.47	−27:43:13.1	17.03	2.80	40.4	−0.14	0.103	ABS	gal	2.0+	ULX, 2dF TGS243Z010
515	MXU2.1	03:32:32.16	−27:46:51.6	-	-		0.41	-			0.0	
516	134	03:32:31.36	−27:47:24.9	21.40	3.00	42.2	−0.26	0.667	LEX	AGN-1	2.0+	5050A-
516	MXU1.1	03:32:31.40	−27:47:24.7	21.40	3.00	42.2	−0.26	0.665	LEX	AGN-1	2.0+	
518	MXU1.1	03:32:26.76	−27:46:04.1	-	-		0.01	-			0.0	
519	122	03:32:25.87	−27:55:06.4	23.38	3.47	42.8	−0.03	1.034	LEX	AGN-2	2.0+	4100Å-
521	119+120+121	03:32:22.76	−27:52:24.0	20.10	2.45	40.5	−0.40	0.131	LEX	gal	2.0+	line ratios
522a*	122	03:32:21.41	−27:55:49.8	24.13	<3.83		−0.34	-			0.0	
522b*	122	03:32:21.40	−27:55:48.7	24.81	<4.51		−0.34	-			0.0	
523	MXU5.1	03:32:20.35	−27:42:28.1	-	-		−0.08	-			0.0	
524	138+139	03:32:19.96	−27:42:43.3	-	-		0.04	-			0.0	

Table 5—Continued

No	mask	α (J2000)	δ (J2000)	R (mag)	R−K (mag)	$L_{\rm X}$ $\left(\log \frac{erg}{s}\right)$	HR	z	Class (opt)	Class (X-ray)	Qual	Comments
524	MXU5.1	03:32:20.02	−27:42:43.8	-	-		0.04	-			0.0	
525	138	03:32:19.80	−27:41:22.8	19.15	3.11	41.4	−0.01	0.229	LEX	AGN-2	2.0+	line ratios: low $L_{\rm X}$ AGN-2
526a	134	03:32:18.70	−27:44:13.0	23.55	4.93		0.18	-			0.0	
526a	138+139	03:32:18.70	−27:44:13.0	23.55	4.93		0.18	-			0.0	
526a	MXU1.1	03:32:18.73	−27:44:12.7	23.55	4.93		0.18	-			0.0	
526b	138+139	03:32:18.63	−27:44:11.7	24.71	<4.41		0.18	-			0.0	
526b	MXU1.1	03:32:18.66	−27:44:11.6	24.71	<4.41		0.18	-			0.0	
526c		03:32:18.82	−27:44:13.0	22.99	NA	42.5	0.18	0.958	LEX	AGN-2	2.0	ref 1, [O II]
527*	MXU4.1	03:32:18.54	−27:54:13.1	-	-		−0.29	-			0.0	
528	MXU4.1	03:32:17.15	−27:54:02.4	23.41	<3.11		0.10	-			0.0	
530	MXU5.1	03:32:14.90	−27:38:43.9	23.23	NA		0.33	-			0.0	
531	119+120+121	03:32:14.44	−27:51:10.9	23.73	4.69	43.3	0.41	1.544	HEX	AGN-2	2.0+	HeII, CIV
531	MXU4.1	03:32:14.44	−27:51:10.9	23.73	4.69	43.3	0.41	1.544	HEX	AGN-2	2.0+	He II, C IV
534	134	03:32:12.21	−27:45:30.2	21.67	4.06	42.2	0.34	0.676	LEX	AGN-2	2.0+	[NeV]?
535	138+139	03:32:11.42	−27:46:50.0	22.01	3.81	42.3	−0.01	0.575	LEX	AGN-2	2.0+	
538	138	03:32:08.55	−27:46:48.4	19.18	3.96	41.4	0.08	0.310	LEX	AGN-2	2.0+	-8750Å, line ratios, low $L_{\rm X}$ AGN-2
539	MXU5.1	03:32:04.05	−27:37:25.5	23.95	NA	43.7	−0.40	0.977	BLAGN	AGN-1	2.0+	Mg II, [O II]
540	MXU4.1	03:32:02.57	−27:50:52.6	25.37	4.83		−0.05	-			0.0	
541	MXU11.1	03:31:59.75	−27:49:49.5	-	K20.33		0.08	-			0.0	
542	MOS11.1	03:31:58.44	−27:54:37.2	-	-		−0.16	-			0.0	
543a	MOS11.1	03:31:56.90	−27:51:02.0	26.06	<5.76		0.17	-			0.0	
547a	MXU11.1	03:31:50.40	−27:52:38.0	24.45	<4.15	43.8	0.24	2.316	LEX	AGN-2	1.0	
549		03:32:22.61	−27:58:04.1	11.44W	2.05TM		−1.00	0	star	star	2.0+	TYC 6453-888-1
552	121	03:32:15.80	−27:53:24.7	22.62	4.33	41.6	−1.00	0.673	LEX	gal	2.0+	-7800Å
552	122	03:32:15.80	−27:53:24.7	22.62	4.33	41.6	−1.00	0.674	LEX	gal	2.0+	
553a	137	03:32:56.66	−27:53:16.6	20.02	2.28	41.0	−1.00	0.366	LEX	gal	2.0+	5900Å-, line ratios
554	MXU11.1	03:31:50.77	−27:53:01.1	24.32	<4.02		−1.00	-			0.0	
560*	138+139	03:32:06.29	−27:45:36.8	21.93	4.21	41.4	−1.00	0.669	ABS	gal/grp	2.0+	-8550Å, [OII]?
561a	MXU1.1	03:32:22.45	−27:45:44.3	-	-		−1.00	-			0.0	
563	134	03:32:31.47	−27:46:23.2	23.30	4.49		−1.00	-			0.0	3800Å-
563	MXU2.1	03:32:31.47	−27:46:23.2	23.30	4.49		−1.00	-			0.0	
563		03:32:31.54	−27:46:24.6	23.30	4.49	42.4	−1.00	2.223	HEX	AGN-1	2.0+	ref 4: narrow HeII, CIII]
565	119+120+121	03:32:24.85	−27:47:06.4	20.69	3.07	40.4	−1.00	0.368	LEX	gal	2.0+	5950Å-, line ratios
565	134	03:32:24.85	−27:47:06.4	20.69	3.07	40.4	−1.00	0.363	LEX	gal	2.0+	

Table 5—Continued

No	mask	α (J2000)	δ (J2000)	R (mag)	R−K (mag)	L_X ($\log \frac{erg}{s}$)	HR	z	Class (opt)	Class (X-ray)	Qual	Comments
567a	134	03:32:38.78	−27:47:32.2	21.12	2.96	40.8	−1.00	0.460	LEX	gal	2.0+	6000Å-, line ratios
567a	137	03:32:38.78	−27:47:32.2	21.12	2.96	40.8	−1.00	0.456	LEX	gal	2.0+	
567b	137	03:32:38.88	−27:47:33.3	23.19	<2.89		−1.00	-			0.0	
570	138+139	03:32:22.54	−27:48:04.3	24.58	<4.28		−1.00	-			0.0	
572	MXU1.1	03:32:22.25	−27:48:11.0	26.95	<6.65		−1.00	-			0.0	
573	137	03:32:44.44	−27:48:19.0	20.58	3.33	40.6	−1.00	0.414	LEX	gal	2.0+	-8000Å
575	119+120+121	03:32:17.08	−27:49:21.7	19.70	3.48	40.5	−1.00	0.340	ABS	gal	2.0+	[OII]?
577a	89	03:32:36.18	−27:49:31.8	20.99	4.09		−1.00	-			0.0	
577a	119+120	03:32:36.18	−27:49:31.8	20.99	4.09	41.3	−1.00	0.547	LEX	gal	2.0+	6350A-
579a	119+120+121	03:32:34.16	−27:49:39.5	25.29	<4.99		−1.00	-			0.0	
579a	137	03:32:34.15	−27:49:39.5	25.29	<4.99		−1.00	-			0.0	
579b	119+120+121	03:32:34.05	−27:49:37.8	24.93	5.50		−1.00	-			0.0	5700Å-
579b	137	03:32:34.05	−27:49:37.8	24.93	5.50		−1.00	-			0.0	
580a	119+120	03:32:16.17	−27:49:41.9	21.22	4.32	41.1	−1.00	0.664	HEX	gal	2.0+	interacting, [NeV], possible low L_X| AGN-1
580b	121	03:32:15.98	−27:49:43.3	21.69	4.60	41.1	−1.00	0.666	ABS	gal	2.0	interacting
581*	MXU4.1	03:32:07.36	−27:49:41.9	24.38	<4.08		−1.00	-			0.0	
581*	MOS11.1	03:32:07.27	−27:49:42.6	24.38	<4.08		−1.00	-			0.0	4100Å-
582b	89	03:32:38.83	−27:49:56.3	20.21	NA	40.2	−1.00	0.242	LEX	gal	2.0+	line ratios
582b	137	03:32:38.83	−27:49:56.3	20.21	NA	40.2	−1.00	0.241	LEX	gal	2.0+	
583	MXU4.1	03:32:13.92	−27:50:01.2	-	K19.81		−1.00	-			0.0	
584	119	03:32:17.86	−27:50:07.1	20.32	3.50		−1.00	0	M-star	M-star	2.0+	around M-5
585a	MXU11.1	03:31:55.12	−27:50:28.6	23.77	5.88	42.0	−1.00	1.212	LEX	AGN-1	1.0	
586	137	03:32:39.47	−27:50:31.9	22.23	4.23	41.1	−1.00	0.580	ABS	gal	2.0+	
587	121	03:32:15.28	−27:50:39.4	21.00	2.89	40.1	−1.00	0.245	ABS	gal	2.0+	
587	122	03:32:15.28	−27:50:39.4	21.00	2.89	40.1	−1.00	0.246	ABS	gal	2.0+	
588	MXU11.1	03:31:55.61	−27:50:43.9	19.80	3.99		−1.00	0	M-star	M-star	2.0+	
590a	122	03:32:07.12	−27:51:29.1	25.07	<4.77		−1.00	-	BLLAC?		0.0	BLLAC?, -8400Å
591	MOS11.1	03:31:44.88	−27:51:38.9	-	-		−1.00	-			0.0	-7500Å
593	138+139	03:32:14.70	−27:44:02.9	25.87	<5.57		−1.00	-			0.0	
593	MXU1.1	03:32:14.81	−27:44:02.6	25.87	<5.57		−1.00	-			0.0	
595	MXU5.1	03:32:15.77	−27:39:54.2	25.71	<5.41		−1.00	-			0.0	4000Å-
598	MXU4.1	03:32:24.68	−27:54:11.6	21.18	3.17	41.9	1.00	0.617	ABS	AGN-2	2.0+	
599	122	03:32:29.81	−27:53:30.1	25.16	<4.86		1.00	-			0.0	
600	MXU1.1	03:32:13.86	−27:45:25.7	23.77	5.22		1.00	-			0.0	

Table 5—Continued

No	mask	α (J2000)	δ (J2000)	R (mag)	R−K (mag)	L_X $\left(\log \frac{erg}{s}\right)$	HR	z	Class (opt)	Class (X-ray)	Qual	Comments
600		03:32:13.88	−27:45:26.5	23.77	5.22	42.9	1.00	1.327	LEX	AGN-2	2.0+	ref 1
601	134	03:32:18.45	−27:45:56.0	22.05	4.58	42.2	1.00	0.735	ABS	AGN-2	2.0+	
602	134	03:32:21.98	−27:46:55.8	21.55	4.48	42.2	1.00	0.668	ABS	AGN-2	2.0+	
603	MXU2.1	03:32:57.68	−27:47:10.8	25.52	4.82		1.00	-			0.0	
606a	122	03:32:24.97	−27:50:08.0	25.26	4.30	42.9	1.00	1.037	LEX	AGN-2	1.0	3800Å-
609	119+120+121	03:32:36.20	−27:50:37.1	24.98	5.52		1.00	-			0.0	5300Å-
609	137	03:32:36.20	−27:50:37.1	24.98	5.52		1.00	-			0.0	
610	MXU4.1	03:32:19.85	−27:51:58.6	-	-		1.00	-			0.0	
611a	146	03:32:41.72	−27:43:28.5	23.29	4.65	42.7	1.00	0.979	LEX	AGN-2	1.0	
611b	146	03:32:41.55	−27:43:27.9	23.67	4.97		1.00	-			0.0	
612a	138+139	03:32:21.34	−27:42:28.8	22.57	3.18	41.9	1.00	0.387	LEX	AGN-2	2.0	4200Å-
612b	138+139	03:32:21.43	−27:42:31.2	21.88	3.94	42.6	1.00	0.736	LEX	AGN-2	2.0+	4200Å-
615	MXU4.1	03:32:01.29	−27:50:50.8	23.41	4.47	42.3	0.08	0.759	LEX	AGN-2	2.0+	
615	MOS11.1	03:32:01.21	−27:50:51.4	23.41	4.47	42.3	0.08	0.759	LEX	AGN-2	2.0+	
619	MOS11.1	03:31:55.62	−27:54:02.4	22.73	2.95		−1.00	-			0.0	
620a	119+120+121	03:32:30.15	−27:53:05.9	21.43	2.71	41.2	−1.00	0.648	LEX	gal	2.0+	
621	122	03:32:16.57	−27:52:45.5	24.70	<4.40		−1.00	-			0.0	
621	MXU4.1	03:32:16.57	−27:52:45.5	24.70	<4.40		−1.00	-			0.0	
623a	MXU1.1	03:32:28.46	−27:47:00.0	24.86	4.40		−1.00	-			0.0	
624	134	03:32:29.21	−27:47:07.6	21.70	4.39	41.2	−1.00	0.669	ABS	gal	2.0+	4400Å-
624	138+139	03:32:29.21	−27:47:07.6	21.70	4.39	41.2	−1.00	0.668	ABS	gal	2.0+	4600Å-
626	138+139	03:32:09.48	−27:47:57.1	25.35	<5.05		−1.00	-			0.0	-8600Å
627	120	03:32:23.35	−27:48:52.5	19.84	2.11	40.1	−1.00	0.248	LEX	gal	2.0+	3750Å-, line ratios
630	146	03:32:28.28	−27:44:03.7	23.05	5.32		−1.00	-			0.0	6000Å-
631	138+139	03:32:15.08	−27:43:35.5	24.35	5.59!		−1.00	-			0.0	
633	MXU11.1	03:31:50.43	−27:52:12.2	24.01	4.69	43.2	1.00	1.374	HEX	AGN-2	2.0+	HeII, Mg II, [NeV]
634	MXU2.1	03:32:51.42	−27:47:46.9	24.86	4.87		1.00	-			0.0	
635a	MXU4.1	03:32:16.78	−27:50:07.9	23.01	4.51	42.1	1.00	0.729	ABS	AGN-2	2.0	more counterparts?
638	146	03:32:29.95	−27:43:01.3	23.67	4.37		1.00	-			0.0	
640	MXU5.1	03:32:17.66	−27:38:51.4	-	NA		1.00	-			0.0	
642	138+139	03:32:15.19	−27:41:58.9	24.54	4.01	43.7	0.25	2.402	HEX	AGN-2	2.0+	CIV
643	MOS11.1	03:31:56.32	−27:52:56.5	24.96	<4.66		−0.08	-			0.0	
646	134	03:32:45.10	−27:47:24.1	21.01	3.62	40.8	−1.00	0.438	LEX	gal	2.0+	6500Å-
647		03:33:01.82	−27:50:09.4	17.50	2.44		−1.00	0	star	star	2.0+	ref 3

Table 5—Continued

No	mask	α (J2000)	δ (J2000)	R (mag)	R−K (mag)	L_X $(\log \frac{erg}{s})$	HR	z	Class (opt)	Class (X-ray)	Qual	Comments
652	146	03:32:49.33	−27:43:02.3	20.64	1.89	39.3	−1.00	0.077	LEX	gal	2.0+	5800Å-, line ratios
901	MXU2.1	03:32:35.72	−27:49:16.0	25.16	5.10	42.5	−1.00	2.578	HEX	AGN-1	2.0+	CIV, NV
Cluster members for extended source 249 (with associated point source)												
249a	122	03:32:19.29	−27:54:06.0	21.72	5.25	42.6	−0.12	0.964	ABS	AGN-2	2.0+	interacting, within X-ray error circle
249b	122	03:32:19.29	−27:54:03.3	23.15	4.96	42.6	−0.12	0.964	LEX	gal	2.0	interacting
249c	MXU4.1	03:32:17.25	−27:54:04.9	23.50	<3.20	42.6	−0.12	0.962	LEX	gal	1.0	
Cluster members for extended source 566 (with associated point source)												
566a	6+7	03:32:18.02	−27:47:18.5	20.62	4.88	41.8	−1.00	0.734	LEX	gal	2.0+	
566a	134	03:32:18.02	−27:47:18.5	20.62	4.88	41.8	−1.00	0.734	LEX	gal	2.0+	
566b	22+23+24	03:32:20.65	−27:47:17.1	21.78	3.52	41.8	−1.00	0.733	LEX		1.0	not centered, contaminated, 3900Å-
Cluster members for extended source 594 (with associated point source)												
594a	22	03:32:09.71	−27:42:48.2	21.52	4.53	41.9	−1.00	0.733	LEX	gal	2.0+	
594a	138	03:32:09.71	−27:42:48.2	21.52	4.53	41.9	−1.00	0.733	LEX	gal	2.0+	
594c	82	03:32:09.20	−27:42:25.7	22.92	4.60	41.9	−1.00	0.734	ABS	gal	2.0+	
594c	MXU5.1	03:32:09.20	−27:42:25.7	22.92	4.60	41.9	−1.00	0.734	ABS	gal	2.0+	
594d	MXU5.1	03:32:08.54	−27:42:17.8	22.09	4.61	41.9	−1.00	0.732	ABS	gal	2.0+	
594e	99	03:32:09.40	−27:42:36.4	23.10	4.52	41.9	−1.00	-		gal	0.0	
594e	138	03:32:09.40	−27:42:36.2	23.10	4.52	41.9	−1.00	0.731	ABS	gal	2.0	G-band
Cluster members for extended source 645 (no associated point source)												
645a	MXU11.1	03:31:49.79	−27:49:40.0	21.61	4.87	42.0	−1.00	0.679	ABS	gal	2.0+	
645b	MXU11.1	03:31:51.66	−27:49:30.7	21.51	4.51	42.0	−1.00	0.683	ABS	gal	2.0	

Note. — ref 1: A. Cimatti & R. Gilli, private communication, ref 2: paper I: Giacconi et al. 2001, ApJ 551,624, ref 3: C. Wolf, private communication, ref 4: Daddi et al. (2003)
See Section 7 for explanation of columns.

*: extended X-ray source.
See Table 6 for diagnostics on line ratios.

Table 6. Line ratios.

No	$\log \frac{[OIII]}{H\beta}$ [5007Å/4861Å]	$\log \frac{[SII]}{H\alpha}$ [6716+6731Å/6563Å]	$\log \frac{[NII]}{H\alpha}$ [6583Å/6563Å]	$\log \frac{[OI]}{H\alpha}$ [6300Å/6563Å]	Class
41	0.98	-	-	-	Seyfert II
75	0.56	-	-	-	-
155	0.94	-	-	-	Seyfert II
175a	0.25	−0.58	−0.60	-	NELG
190	1.00	-	-	-	Seyfert II
201b	0.88	-	-	-	Seyfert II
521	0.26	-	^{x}	−0.98	LINER
525	>1.0	-	0.04^x	-	Seyfert II
538	0.73	-	−0.03	-	Seyfert II
553a	0.56	−0.94	-	-	HII region
565	0.07	−0.51	−0.46	-	NELG
567a	−0.11	-	-	-	-
582b	<0.0	-	−0.39	-	-
627	0.28	−0.61	-	-	NELG
652	-	−0.48	-	-	-

Note. — Traditional line ratios used for classification of emission-line galaxies. We only measured line strengths for objects with suffitiently high signal-to-noise spectra.
The classification as Seyfert II, LINER, NELG or HII region is derived from the line ratio diagnostics given by Ho et al. (1993).
^{x} possible broad Hα component.

Table 7. Optical spectroscopy results for field galaxies.

No	mask	α (J2000)	δ (J2000)	R (mag)	z	Class	Qual	Comments
00012	MXU11.1	03:31:59.60	−27:50:10.7	20.17	0	star	2	
00338	82	03:32:01.00	−27:46:15.5	22.52	0.334	NELG	2	4200Å-
02008	99	03:32:05.80	−27:41:45.2	20.71	0	M-star	2	
02045	78	03:32:05.97	−27:48:45.8	21.69	0.196	NELG	2	
02124	138+139	03:32:06.26	−27:45:42.7	17.37	0.000	star	2	
02215	MXU4.1	03:32:06.59	−27:50:38.2	20.55	0.339	NELG	2	
02215	MXU11.1	03:32:06.49	−27:50:38.7	20.55	0.337	NELG	2	4900Å-, contaminated
02311	99	03:32:06.88	−27:42:07.7	21.08	0.286	gal	2	
02311	MXU5.1	03:32:06.89	−27:42:07.7	21.08	0.283	NELG	2	
02569	88	03:32:07.58	−27:48:40.6	18.58	0	star?		-8450Å, star?
02593	6+7	03:32:07.67	−27:47:31.5	19.29	0	M-star	2	M5+ star
02869	MXU5.1	03:32:08.44	−27:42:43.5	21.83	0.420	NELG	2	
02910	88	03:32:08.55	−27:46:48.4	19.18	0.310	NELG	2	-8800Å
02969	78	03:32:08.69	−27:52:11.5	24.67	0.561	NELG	1	
03204	138	03:32:09.40	−27:42:36.2	23.10	0.731	gal	2	
03268	138+139	03:32:09.58	−27:42:41.9	23.77	0.681	NELG	2	
03470	88	03:32:10.08	−27:49:07.3	18.86	0	Star	2	
04024	138+139	03:32:11.60	−27:46:59.2	22.72	0.816	NELG	2	
04356	MXU5.1	03:32:12.47	−27:39:32.8	20.60	0.214	NELG	2	
04500	122	03:32:12.90	−27:52:27.9	24.22	0.741	NELG	1	
04766	6+7	03:32:13.69	−27:49:15.2	22.98	0.538	NELG	2	
04888	22+23+24	03:32:14.03	−27:46:34.3	23.76	0.836	NELG	1	
05395	121	03:32:15.38	−27:50:45.1	19.00	0.23	gal	1	Halo only
05614	MXU4.1	03:32:15.99	−27:53:50.1	17.92	0	star	2	
05619	MXU4.1	03:32:16.00	−27:52:11.9	19.39	0	M-star	2	Early
05857	MXU5.1	03:32:16.70	−27:43:24.4	21.66	0	M-star	2	
06215	6+7	03:32:17.58	−27:49:41.1	22.01	0.337	NELG	2	
06312	88	03:32:17.84	−27:46:28.0	18.10	0	Star	2	
06629	138+139	03:32:18.73	−27:44:16.1	21.62	0.603	gal	1	
06683	88	03:32:18.84	−27:45:29.4	19.16	0.450	gal	1	Sky residuals
06780	138+139	03:32:19.14	−27:47:59.5	21.31	0.228	NELG	2	
06861	MXU4.1	03:32:19.36	−27:53:31.0	18.71	0	star	2	Late-K or early M
06894	MXU5.1	03:32:19.48	−27:42:16.8	20.81	0.382	gal	2	
06913	78	03:32:19.52	−27:54:43.2	23.69	0.247	NELG	1	5100Å-
07159	78	03:32:20.27	−27:52:22.1	20.36	0.343	NELG	2	
07210	122	03:32:20.44	−27:49:14.2	22.63	0.115	NELG	2	
07511	78	03:32:21.23	−27:52:23.6	25.52	0.863	NELG	1	
07694	MXU4.1	03:32:21.77	−27:54:09.8	19.93	0	star	2	
07894	119+120+121	03:32:22.33	−27:45:59.9	22.76	0.727	NELG	1	6400Å-, edge
07993	134	03:32:22.59	−27:44:26.0	21.07	0.738	NELG	2	
07993	138+139	03:32:22.59	−27:44:26.0	21.07	0.737	NELG	2	3800Å-, partly on slit
08145	122	03:32:22.97	−27:55:29.4	24.05	0.780	NELG	1	
08198	134	03:32:23.16	−27:44:23.0	22.69	0.739	NELG	1	
08302	84	03:32:23.47	−27:42:57.9	24.89	1.020	NELG	1	
08351	MXU1.1	03:32:23.67	−27:46:56.6	18.05	0	Star	2	

Table 7—Continued

No	mask	α (J2000)	δ (J2000)	R (mag)	z	Class	Qual	Comments
08619	78	03:32:24.53	−27:54:43.0	19.24	0.126	NELG	1	4200Å-
09290	46+47	03:32:26.53	−27:43:03.8	21.04	0.216	NELG	1	6900Å-
09479	78	03:32:27.06	−27:54:16.3	24.14	1.405	BLAGN	1	3600Å-
09511	84	03:32:27.15	−27:41:45.9	20.66	0	Star	2	
09949	146	03:32:28.15	−27:43:08.1	23.33	0.339	NELG	2	5100Å-
10024	MXU1.1	03:32:28.37	−27:48:07.3	19.93	0	M-star	2	
10444	138+139	03:32:28.96	−27:46:55.9	22.00	0.301	gal	2	4600Å-
11210	122	03:32:29.83	−27:53:41.0	23.77	0.987	NELG	1	5400Å-
11338	MXU2.1	03:32:29.99	−27:48:39.6	21.26	0	M-star	2	Early type
12519	46+47	03:32:31.51	−27:40:59.9	20.14	0	M-star	2	
12596	28+29	03:32:31.65	−27:39:48.6	19.21	0	Star	2	
12982	46+47	03:32:32.53	−27:41:58.3	23.33	0.682	NELG	1	4400Å-
13046	86	03:32:32.72	−27:48:59.5	22.35	0.669	NELG	1	
13094	134	03:32:32.81	−27:46:08.0	20.47	0.368	NELG	1	
13106	84	03:32:32.86	−27:41:55.8	24.27	0.948	NELG	1	
14502	15	03:32:35.98	−27:51:18.4	20.42	0.358	NELG	2	Not centered
14768	86	03:32:36.45	−27:46:55.2	24.00	0.894	NELG	1	-9300Å
15210	46+47	03:32:37.37	−27:41:26.2	20.66	0.670	gal	2	blended
15471	90	03:32:37.93	−27:46:09.2	20.11	0.086	gal	2	reduction problem
15505	89	03:32:38.00	−27:47:41.7	19.04	0	Star	2	Not centered
15773	86	03:32:38.59	−27:46:31.6	21.96	0.625	gal	1	
16089	89	03:32:39.16	−27:48:44.6	19.68	0.457	gal	2	
16647	15	03:32:40.37	−27:55:38.2	23.55	0.350	NELG	1	Not centered
17281	15	03:32:41.64	−27:51:57.6	21.30	0.783	gal	2	
17312	46+47	03:32:41.72	−27:40:07.7	23.76	0.761	NELG	1	
17624	15	03:32:42.33	−27:49:50.8	21.07	0.459	NELG	2	4100Å-
17660	MXU2.1	03:32:42.41	−27:47:58.8	19.85	0	M-star	2	
17958	84	03:32:43.03	−27:43:59.9	21.73	0	M-star	2	
18065	46+47	03:32:43.23	−27:40:22.0	23.13	0.425	NELG	2	
18365	90	03:32:43.82	−27:46:05.5	17.71	0	Star	2	
18468	89	03:32:44.03	−27:48:24.3	19.01	0	Star	2	
18473	89	03:32:44.06	−27:51:43.3	19.19	0.305	NELG	1	Sky residuals
18474	46+47	03:32:44.06	−27:40:48.2	23.43	0.730	gal	1	
18545	134	03:32:44.20	−27:47:33.5	21.96	0.738	NELG	2	6650Å-
18745	15	03:32:44.60	−27:52:58.3	23.26	0.662	NELG	1	Not centered
18814	36+39+40	03:32:44.68	−27:49:22.4	21.69	0.521	NELG	1	-8750Å
18894	36+39+40	03:32:44.86	−27:47:27.2	18.82	0.215	NELG	2	Not centered, -8950Å
18894	89	03:32:44.87	−27:47:27.6	18.82	0.213	NELG	2	Partly on slit
18981	137	03:32:45.02	−27:54:39.6	19.55	0.459	NELG	2	6450Å-
18995	47	03:32:45.05	−27:41:09.5	21.89	0.735	NELG	2	
19026	36+39+40	03:32:45.05	−27:47:38.3	20.36	0.346	NELG	2	-8900Å
19260	46	03:32:45.51	−27:40:53.2	21.57	0.740	NELG	2	
19633	46	03:32:46.24	−27:41:23.9	23.14	0.638	NELG	2	
19887	47	03:32:46.78	−27:41:14.1	21.88	0.730	gal	2	
19977	39+40	03:32:47.00	−27:43:42.2	22.29	0.417	NELG	2	

Table 7—Continued

No	mask	α (J2000)	δ (J2000)	R (mag)	z	Class	Qual	Comments
20803	46+47	03:32:48.65	−27:44:33.3	22.92	0.215	NELG	2	5550Å-
20811	89	03:32:48.63	−27:46:26.4	18.89	0.145	gal	2	
20811	MXU2.1	03:32:48.63	−27:46:26.4	18.89	0.147	gal	2	
21088	90	03:32:49.20	−27:44:36.3	19.81	0.217	NELG	2	3700Å-
21303	90	03:32:49.65	−27:41:34.8	18.88	0	Star	2	
21714	90	03:32:50.52	−27:41:25.4	19.05	0.146	gal	2	
21757	84	03:32:50.60	−27:42:30.1	20.94	0.125	NELG	2	
22083	46+47	03:32:51.28	−27:44:29.4	20.77	0.534	gal	2	5100Å-
22439	146	03:32:52.05	−27:44:29.8	21.80	0.821	NELG	1	
22450	86	03:32:52.07	−27:45:59.2	23.78	0.538	NELG	1	
22471	89	03:32:52.12	−27:51:08.9	20.40	0.128	NELG	2	3500Å-
22892	89	03:32:53.06	−27:45:19.0	18.78	0.279	gal	2	3800Å-
22892	90	03:32:53.06	−27:45:19.0	18.78	0.278	gal	2	5300Å-
23076	MXU2.1	03:32:53.45	−27:48:29.6	18.40	0	Star	2	
23256	90	03:32:53.92	−27:41:09.9	18.93	0.146	NELG	2	
23290	15	03:32:54.01	−27:54:42.2	19.91	0.147	NELG	2	
23307	86	03:32:54.02	−27:47:04.5	22.05	0	M-star	2	
23483	90	03:32:54.41	−27:40:53.5	18.02	0.146	gal	2	
23540	MXU2.1	03:32:54.51	−27:46:16.2	18.36	0	Star	1	Bad sky subtraction
24034	46+47	03:32:55.58	−27:43:22.5	19.27	0.146	NELG	2	
24251	90	03:32:55.97	−27:44:18.2	20.11	0	M-star	2	5500Å-
26135	86	03:32:58.89	−27:45:30.3	23.19	1.035	NELG	1	Not centered
26822	36+39+40	03:33:01.24	−27:49:42.4	21.35	0.512	gal	2	3800Å-
27022	36+39+40	03:33:02.76	−27:43:16.1	16.75	0.129	gal	2	4400Å-, sky residuals
27511	36+39+40	03:33:07.10	−27:46:39.7	18.29	0.220	gal	2	5800Å-, good signal, HELP!
27747	36+39+40	03:33:09.51	−27:44:07.0	19.10	0.104	NELG	2	6700Å-, CHECK!
60014	99	03:31:59.33	−27:43:02.4	20.50	0	M-star	2	4700Å-
60017	99	03:31:57.85	−27:42:45.3	21.10	0.670	gal	2	
60019	99	03:31:57.37	−27:42:39.4	20.66	0.667	NELG	2	4350-
60021	99	03:31:56.42	−27:40:45.9	18.75	0	M-star	2	
60024	99	03:31:50.96	−27:41:16.1	22.00	0.253	NELG	1	
60028	99	03:31:49.02	−27:39:45.7	N/A	0.813	NELG	1	
60029	99	03:31:45.03	−27:40:56.5	N/A	0.421	NELG	1	Sky residuals
60033	MXU11.1	03:31:45.91	−27:51:30.7	21.88	0.681	NELG	2	
60035	MXU11.1	03:31:44.63	−27:50:52.3	20.76	0.523	NELG	2	
60036	MXU11.1	03:31:57.25	−27:52:22.7	21.27	0	M-star	2	
60037	MXU11.1	03:31:54.08	−27:55:01.9	20.82	0	Star	2	
60038	MXU11.1	03:31:47.10	−27:53:26.4	20.92	0	Star	2	
60039	MOS11.1	03:32:04.53	−27:50:07.4	19.90	0.229	NELG	2	
60041	MXU11.1	03:31:49.82	−27:48:36.6	19.07	0.182	NELG	2	

Note. — See Section 9 for explanation of columns.

Table 8. Comparision of the optical and X-ray classification.

	BLAGN	HEX	LEX	ABS
X-ray AGN-1 and QSO-1	31	5	10	1
X-ray AGN-2 and QSO-2	1	16	24	8
X-ray galaxy	0	3	20	12

Note. — Only the reliable identifications are shown.

Table 9. Optical counterparts not observed in our program.

No	α (J2000)	δ (J2000)	R (mag)	R-K (mag)	HR
Additional counterpart candidates					
17a	03:32:49.17	−27:55:04.6	24.59	-	-0.41
17b	03:32:49.31	−27:55:06.7	25.00	-	-0.41
70c	03:32:01.21	−27:46:47.4	24.31	-	0.47
86b	03:32:33.85	−27:45:18.4	24.62	4.62	-0.05
96b	03:32:20.71	−27:52:22.9	25.00	-	-0.39
101b	03:32:55.48	−27:47:53.4	24.61	4.20	-0.43
124c	03:32:02.61	−27:45:24.9	25.49	-	-1.00
189a	03:32:45.90	−27:42:13.4	25.09	-	1.00
189b	03:32:45.80	−27:42:11.3	25.40	-	1.00
189c	03:32:45.78	−27:42:12.2	24.21	-	1.00
201a	03:32:39.05	−27:44:39.7	26.11	-	-0.06
205a	03:32:17.11	−27:41:36.9	25.99	5.49	0.16
217a	03:32:33.10	−27:52:05.9	-	-	-1.00
224b	03:32:28.82	−27:46:21.6	25.04	-	-1.00
239c	03:32:36.09	−27:51:28.3	25.00	-	-0.27
257c	03:32:13.49	−27:48:55.1	25.64	-	0.35
268b	03:32:49.31	−27:40:48.4	24.58	-	1.00
511c*	03:32:36.65	−27:46:31.2	23.83	4.68	-0.24
511d*	03:32:36.42	−27:46:31.6	23.61	4.50	-0.24
522c*	03:32:21.49	−27:55:51.6	24.15	-	-0.34
543b	03:31:56.92	−27:51:00.6	24.52	-	0.17
547b	03:31:50.43	−27:52:36.8	25.90	-	0.24
547c	03:31:50.27	−27:52:35.9	24.81	-	0.24
553b	03:32:56.71	−27:53:19.2	21.52	2.59	-1.00
577b	03:32:36.35	−27:49:33.1	26.31	6.12	-1.00
585b	03:31:55.44	−27:50:30.1	23.74	2.84	-1.00
590b	03:32:07.18	−27:51:31.0	26.05	-	-1.00
606b	03:32:24.91	−27:50:10.0	26.13	-	1.00
620b	03:32:30.26	−27:53:06.4	23.04	-	-1.00
623b	03:32:28.55	−27:46:58.8	25.23	4.72	-1.00
Inside the 8 arc min circle					
48	03:32:24.85	−27:56:00.1	24.55	4.79	-0.03
58	03:32:11.80	−27:46:28.3	26.00	4.77	-0.36
72a	03:31:58.27	−27:50:42.1	26.07	5.82	-0.23
133	03:32:02.49	−27:44:29.6	-	-	0.00
146	03:32:47.20	−27:53:36.5	24.40	-	-0.01
159	03:32:50.15	−27:52:52.0	23.30	4.25	-0.30
210	03:32:38.35	−27:55:53.6	-	K=19.75	-0.45
226	03:32:04.46	−27:46:43.3	-	-	-0.43

Table 9—Continued

No	α (J2000)	δ (J2000)	R (mag)	R-K (mag)	HR
227	03:32:05.37	−27:46:44.5	26.67	6.94	0.55
232	03:31:55.83	−27:49:21.5	24.14	5.84	-1.00
240*	03:32:59.04	−27:51:40.4	25.00W	5.80	-0.15
265	03:32:33.31	−27:42:36.4	-	K=20.32	0.47
507a*	03:33:00.14	−27:49:23.2	22.86	1.65	0.10
507b*	03:32:59.92	−27:49:24.1	24.51	-	0.10
508	03:32:51.69	−27:52:13.5	-	-	0.33
510	03:32:38.79	−27:51:21.7	25.42	99.00	0.28
529a*	03:32:16.41	−27:55:24.3	23.79	-	0.11
529b*	03:32:16.10	−27:55:27.4	23.17	3.22	0.11
532	03:32:14.07	−27:42:30.3	24.59	-	-0.06
536	03:32:10.76	−27:42:34.7	19.39	3.69	-0.25
537	03:32:09.85	−27:50:15.3	-	-	0.02
544*	03:31:54.48	−27:51:05.5	24.18	4.53	0.05
546	03:31:52.33	−27:47:53.0	25.12W	5.64	-0.15
555	03:32:37.96	−27:53:07.9	25.41	-	-1.00
556	03:32:00.43	−27:52:28.8	22.09	4.25	-1.00
557	03:32:38.13	−27:43:58.5	25.44	-	-1.00
558	03:31:58.16	−27:44:59.7	21.18W	4.05	-1.00
559	03:32:57.14	−27:45:34.7	17.94	2.41	-1.00
564	03:32:16.63	−27:46:36.7	26.04	-	-1.00
571	03:33:03.75	−27:48:10.4	26.14	5.80	-1.00
574	03:32:31.56	−27:48:53.9	24.33	4.36	-1.00
578a	03:32:48.56	−27:49:34.5	24.43	5.59	-1.00
578b	03:32:48.41	−27:49:36.2	25.75	-	-1.00
589	03:32:25.80	−27:51:20.4	-	-	-1.00
592	03:32:47.18	−27:51:47.6	23.54	4.64	-1.00
605	03:32:39.18	−27:48:32.4	25.30	4.05	1.00
607	03:31:59.54	−27:50:20.0	23.77	4.54	1.00
614	03:32:34.58	−27:40:40.5	-	K=19.97	0.02
618	03:32:29.35	−27:56:19.4	25.57W	-	-1.00
622a	03:32:50.01	−27:44:07.2	24.20	-	-1.00
622b	03:32:50.01	−27:44:05.4	25.38	-	-1.00
625	03:32:00.92	−27:47:57.0	21.68	4.31	-1.00
628	03:32:55.50	−27:51:06.5	16.79	3.59	-1.00
629	03:32:53.33	−27:51:04.6	25.26	-	-1.00
632	03:32:33.45	−27:52:27.8	-	-	1.00
637	03:32:25.65	−27:43:31.6	-	-	1.00
639	03:32:52.63	−27:42:39.24	23.36	4.91	1.00
902	03:32:22.07	−27:51:12.2	26.15	-	+1.00
903	03:32:25.84	−27:40:47.8	23.07	3.90	-1.00

Outside the 8 arc min circle

Table 9—Continued

No	α (J2000)	δ (J2000)	R (mag)	R-K (mag)	HR
3	03:33:05.90	−27:46:50.6	-	-	-0.14
9	03:33:00.76	−27:55:20.6	23.53	4.43	-0.57
35	03:32:34.43	−27:39:13.2	24.32	5.60	-0.07
69a	03:32:01.46	−27:41:39.2	24.02	4.61	-0.26
69b	03:32:01.52	−27:41:40.5	23.90	-	-0.26
174	03:33:01.21	−27:44:20.9	25.37	7.21	0.05
179	03:31:49.50	−27:50:34.0	-	-	-0.34
203	03:32:26.67	−27:40:13.6	23.53	3.25	-0.29
213a	03:32:00.58	−27:53:53.5	25.65	-	-0.08
213b	03:32:00.37	−27:53:53.3	25.06	-	-0.08
213c	03:32:00.43	−27:53:56.2	24.20	-	-0.08
219	03:31:50.43	−27:51:52.1	-	K=19.94	-0.32
244	03:32:04.33	−27:40:27.0	25.29	-	-1.00
246	03:32:22.86	−27:39:36.8	20.73	2.15	-0.24
501	03:33:10.19	−27:48:42.1	22.99	NA	-0.38
502	03:33:08.17	−27:50:33.3	21.21	4.13	0.26
503	03:33:07.62	−27:51:27.1	23.26	3.60	-0.41
504	03:33:05.67	−27:52:14.5	18.96	3.31	0.18
505a	03:33:04.81	−27:47:31.9	25.48	6.23	0.33
505b	03:33:04.96	−27:47:33.3	24.64	-	0.33
506	03:33:02.99	−27:51:47.0	-	-	-0.49
520	03:32:25.93	−27:39:27.6	23.18	-	-0.17
548a	03:31:44.85	−27:51:59.3	24.85	-	-0.42
548b	03:31:44.49	−27:51:59.4	25.06	5.99	-0.42
568	03:33:11.07	−27:47:34.4	-	NA	-1.00
576	03:31:44.19	−27:49:26.4	-	NA	-1.00
597	03:32:51.36	−27:55:43.7	24.69	5.46	1.00
608	03:33:03.87	−27:50:26.2	20.74	3.17	1.00
613	03:32:24.55	−27:40:10.4	23.13	4.59	1.00
636	03:31:50.40	−27:50:42.0	-	K=19.83	1.00
649	03:32:24.76	−27:38:50.7	-	NA	-1.00
650	03:33:07.31	−27:44:32.7	17.40	2.93	-1.00
653a	03:33:03.72	−27:44:12.2	25.04	5.31	1.00
653b	03:33:03.82	−27:44:11.7	26.20	-	1.00
653c	03:33:03.74	−27:44:11.0	-	K=19.63	1.00
Objects not covered by our imaging survey					
2	03:33:08.81	−27:42:54.8	22.84W	3.85	-0.65
7	03:33:01.68	−27:58:17.8	20.26W	NA	-0.34
8	03:33:01.51	−27:41:42.3	23.43W	4.66	-0.07
29	03:32:38.95	−27:57:01.1	18.74W	3.21	0.39
40	03:32:29.02	−27:57:30.6	20.82W	4.43	-0.34
74	03:31:57.82	−27:42:09.0	22.06W	4.57	-0.26

Table 9—Continued

No	α (J2000)	δ (J2000)	R (mag)	R-K (mag)	HR
183	03:32:34.12	−27:56:40.5	-	-	1.00
208	03:31:52.57	−27:46:42.7	21.39W	3.95	-0.39
225	03:31:49.43	−27:46:34.4	22.31W	3.07	-0.31
509	03:32:42.20	−27:57:54.0	-	NA	-0.07
517	03:32:30.15	−28:00:21.6	21.88W	NA	-0.21
533	03:32:13.87	−27:56:01.2	-	-	0.17
545	03:31:54.40	−27:41:59.3	24.39W	3.89	0.32
550	03:33:00.71	−27:57:48.2	24.28W	NA	-1.00
551	03:32:16.16	−27:56:44.4	22.46W	2.19	-1.00
562	03:31:51.39	−27:45:53.7	26.03W	-	-1.00
569	03:31:48.06	−27:48:02.2	24.49W	4.39	-1.00
596	03:32:31.88	−27:57:14.0	25.22W	5.79	1.00
604	03:31:48.62	−27:47:15.0	26.56W	6.56	1.00
616	03:32:25.49	−27:58:42.4	-	NA	-1.00
617	03:32:31.44	−27:57:26.5	21.37W	4.08	-1.00
641	03:32:39.06	−27:59:17.0	-	NA	0.14
644	03:32:45.98	−27:57:45.9	16.74W	2.51	-1.00
648	03:32:46.56	−27:57:13.5	-	K=16.91	-1.00
651	03:32:28.47	−27:58:09.1	18.97W	NA	-1.00

Note. — For objects not covered by our FORS imaging survey, the WFI magnitudes are given (Giacconi et al. 2002), indicated by 'W'. If the object is only detected in the K-band, the K magnitude (Vega) is given instead of the R-K color. No detection in the K-band images are indicated by a dash in the R-K column, no coverage is indicated by 'NA'.

Table 10. Success rate of our spectroscopic survey.

Sample	All sources			R<24 sample		
	Total	Observed	Secure	Total	Observed	Secure
All X-ray sources	345/416	247/277	133/141	195/214	157/170	118/126
Sources covered by our imaging survey	322/393	246/276	132/140	180/199	156/169	117/125
Sources covered by our spectroscopic survey	314/385	245/275	131/139	177/196	155/168	116/124
Inner 8 arc min circle	229/274	182/201	107/112	132/147	119/128	95/100

Note. — Both the number of X-ray objects (first number) and the number of optical counterpart candidates (second number) are given. X-ray objects with at least one R<24 optical counterpart candidate were considered part of the R<24 sample. Secure identifications include external identifications. The four clusters (XID 249, 566, 594 and 645) are not included.

Table 11. The number of objects in different object classes

Object class	$z \leq 2$	$z > 2$
AGN-1	26/5	5/0
AGN-2	41/41	1/1
QSO-1	12/0	5/2
QSO-2	1/0	7/2
Galaxy	28/5	0
Cluster	5/1	0
Star	7	NA

Note. — For the AGN/QSO object classes, both secure (first number) and unsecure (second number) identifications are counted.